The Astrophysical Journal, 878:52 (61pp), 2019 June 10 https://doi.org/10.3847/1538-4357/ab1d4e

A Decade of Gamma-Ray Bursts Observed by *Fermi*-LAT: The Second GRB Catalog

M. Ajello[1], M. Arimoto[2], M. Axelsson[3,4], L. Baldini[5], G. Barbiellini[6,7], D. Bastieri[8,9], R. Bellazzini[10], P. N. Bhat[11], E. Bissaldi[12,13], R. D. Blandford[14], R. Bonino[15,16], J. Bonnell[17,18], E. Bottacini[14,19], J. Bregeon[20], P. Bruel[21], R. Buehler[22], R. A. Cameron[14], R. Caputo[23], P. A. Caraveo[24], E. Cavazzuti[25], S. Chen[8,19], C. C. Cheung[26], G. Chiaro[24], S. Ciprini[27,28], D. Costantin[29], M. Crnogorcevic[18], S. Cutini[30], M. Dainotti[14], F. D'Ammando[31,32], P. de la Torre Luque[12], F. de Palma[15], A. Desai[1], R. Desiante[15], N. Di Lalla[5], L. Di Venere[12,13], F. Fana Dirirsa[33], S. J. Fegan[21], A. Franckowiak[22], Y. Fukazawa[34], S. Funk[35], P. Fusco[12,13], F. Gargano[13], D. Gasparrini[28,30], N. Giglietto[12,13], F. Giordano[12,13], M. Giroletti[31], D. Green[36], I. A. Grenier[37], J. E. Grove[26], S. Guiriec[17,38], E. Hays[17], J. W. Hewitt[39], D. Horan[21], G. Jóhannesson[40,41], D. Kocevski[17], M. Kuss[10], L. Latronico[15], J. Li[22], F. Longo[6,7], F. Loparco[12,13], M. N. Lovellette[26], P. Lubrano[30], S. Maldera[15], A. Manfreda[5], G. Martí-Devesa[42], M. N. Mazziotta[13], I. Mereu[43], M. Meyer[14], P. F. Michelson[14], N. Mirabal[17,44], W. Mitthumsiri[45], T. Mizuno[46], M. E. Monzani[14], E. Moretti[47], A. Morselli[27], I. V. Moskalenko[14], M. Negro[15,16], E. Nuss[20], M. Ohno[34], N. Omodei[14], M. Orienti[31], E. Orlando[14], M. Palatiello[6,7], V. S. Paliya[22], D. Paneque[36], M. Persic[6,48], M. Pesce-Rollins[10], V. Petrosian[14], F. Piron[20], S. Poolakkil[11], H. Poon[34], T. A. Porter[14], G. Principe[35], J. L. Racusin[17], S. Rainò[12,13], R. Rando[8,9], M. Razzano[10,61], S. Razzaque[33], A. Reimer[14,42], O. Reimer[14,42], T. Reposeur[49], F. Ryde[4,50], D. Serini[12], C. Sgrò[10], E. J. Siskind[51], E. Sonbas[52], G. Spandre[10], P. Spinelli[12,13], D. J. Suson[53], H. Tajima[14,54], M. Takahashi[36], D. Tak[17,18], J. B. Thayer[14], D. F. Torres[55,56], E. Troja[17,18], J. Valverde[21], P. Veres[11], G. Vianello[14], A. von Kienlin[57], K. Wood[58], M. Yassine[6,7], S. Zhu[59], and S. Zimmer[42,60]

[1] Department of Physics and Astronomy, Clemson University, Kinard Lab of Physics, Clemson, SC 29634-0978, USA
[2] Faculty of Mathematics and Physics, Institute of Science and Engineering, Kanazawa University, Kakuma, Kanazawa, Ishikawa 920-1192, Japan
[3] Department of Physics and Oskar Klein Center for Cosmoparticle Physics, Stockholm University, SE-106 91 Stockholm, Sweden; magnusa@astro.su.se
[4] Department of Physics, KTH Royal Institute of Technology, AlbaNova, SE-106 91 Stockholm, Sweden
[5] Università di Pisa and Istituto Nazionale di Fisica Nucleare, Sezione di Pisa I-56127 Pisa, Italy
[6] Istituto Nazionale di Fisica Nucleare, Sezione di Trieste, I-34127 Trieste, Italy
[7] Dipartimento di Fisica, Università di Trieste, I-34127 Trieste, Italy
[8] Istituto Nazionale di Fisica Nucleare, Sezione di Padova, I-35131 Padova, Italy
[9] Dipartimento di Fisica e Astronomia "G. Galilei," Università di Padova, I-35131 Padova, Italy
[10] Istituto Nazionale di Fisica Nucleare, Sezione di Pisa, I-56127 Pisa, Italy
[11] Center for Space Plasma and Aeronomic Research (CSPAR), University of Alabama in Huntsville, Huntsville, AL 35899, USA
[12] Dipartimento di Fisica "M. Merlin" dell'Università e del Politecnico di Bari, I-70126 Bari, Italy; elisabetta.bissaldi@ba.infn.it
[13] Istituto Nazionale di Fisica Nucleare, Sezione di Bari, I-70126 Bari, Italy
[14] W.W. Hansen Experimental Physics Laboratory, Kavli Institute for Particle Astrophysics and Cosmology, Department of Physics and SLAC National Accelerator Laboratory, Stanford University, Stanford, CA 94305, USA; nicola.omodei@stanford.edu, giacomov@slac.stanford.edu
[15] Istituto Nazionale di Fisica Nucleare, Sezione di Torino, I-10125 Torino, Italy
[16] Dipartimento di Fisica, Università degli Studi di Torino, I-10125 Torino, Italy
[17] NASA Goddard Space Flight Center, Greenbelt, MD 20771, USA
[18] Department of Astronomy, University of Maryland, College Park, MD 20742, USA
[19] Department of Physics and Astronomy, University of Padova, Vicolo Osservatorio 3, I-35122 Padova, Italy
[20] Laboratoire Univers et Particules de Montpellier, Université Montpellier, CNRS/IN2P3, F-34095 Montpellier, France
[21] Laboratoire Leprince-Ringuet, École polytechnique, CNRS/IN2P3, F-91128 Palaiseau, France
[22] Deutsches Elektronen Synchrotron DESY, D-15738 Zeuthen, Germany
[23] Center for Research and Exploration in Space Science and Technology (CRESST) and NASA Goddard Space Flight Center, Greenbelt, MD 20771, USA
[24] INAF-Istituto di Astrofisica Spaziale e Fisica Cosmica Milano, via E. Bassini 15, I-20133 Milano, Italy
[25] Italian Space Agency, Via del Politecnico snc, I-00133 Roma, Italy
[26] Space Science Division, Naval Research Laboratory, Washington, DC 20375-5352, USA
[27] Istituto Nazionale di Fisica Nucleare, Sezione di Roma "Tor Vergata," I-00133 Roma, Italy
[28] Space Science Data Center—Agenzia Spaziale Italiana, Via del Politecnico, snc, I-00133, Roma, Italy
[29] University of Padua, Department of Statistical Science, Via 8 Febbraio, 2, I-35122 Padova, Italy
[30] Istituto Nazionale di Fisica Nucleare, Sezione di Perugia, I-06123 Perugia, Italy
[31] INAF Istituto di Radioastronomia, I-40129 Bologna, Italy
[32] Dipartimento di Astronomia, Università di Bologna, I-40127 Bologna, Italy
[33] Department of Physics, University of Johannesburg, P.O. Box 524, Auckland Park 2006, South Africa
[34] Department of Physical Sciences, Hiroshima University, Higashi-Hiroshima, Hiroshima 739-8526, Japan
[35] Friedrich-Alexander-Universität Erlangen-Nürnberg, Erlangen Centre for Astroparticle Physics, Erwin-Rommel-Str. 1, D-91058 Erlangen, Germany
[36] Max-Planck-Institut für Physik, D-80805 München, Germany
[37] AIM, CEA, CNRS, Université Paris-Saclay, Université Paris Diderot, Sorbonne Paris Cité, F-91191 Gif-sur-Yvette, France
[38] The George Washington University, Department of Physics, 725 21st St., NW, Washington, DC 20052, USA
[39] University of North Florida, Department of Physics, 1 UNF Drive, Jacksonville, FL 32224, USA
[40] Science Institute, University of Iceland, IS-107 Reykjavik, Iceland
[41] Nordita, Royal Institute of Technology and Stockholm University, Roslagstullsbacken 23, SE-106 91 Stockholm, Sweden
[42] Institut für Astro- und Teilchenphysik and Institut für Theoretische Physik, Leopold-Franzens-Universität Innsbruck, A-6020 Innsbruck, Austria
[43] Dipartimento di Fisica, Università degli Studi di Perugia, I-06123 Perugia, Italy
[44] Department of Physics and Center for Space Sciences and Technology, University of Maryland Baltimore County, Baltimore, MD 21250, USA
[45] Department of Physics, Faculty of Science, Mahidol University, Bangkok 10400, Thailand
[46] Hiroshima Astrophysical Science Center, Hiroshima University, Higashi-Hiroshima, Hiroshima 739-8526, Japan
[47] Institut de Física d'Altes Energies (IFAE), Edifici Cn, Universitat Autònoma de Barcelona (UAB), E-08193 Bellaterra (Barcelona), Spain
[48] Osservatorio Astronomico di Trieste, Istituto Nazionale di Astrofisica, I-34143 Trieste, Italy
[49] Centre d'Études Nucléaires de Bordeaux Gradignan, IN2P3/CNRS, Université Bordeaux 1, BP120, F-33175 Gradignan Cedex, France
[50] The Oskar Klein Centre for Cosmoparticle Physics, AlbaNova, SE-106 91 Stockholm, Sweden

[51] NYCB Real-Time Computing Inc., Lattingtown, NY 11560-1025, USA
[52] Adıyaman University, 02040 Adıyaman, Turkey
[53] Purdue University Northwest, Hammond, IN 46323, USA
[54] Solar-Terrestrial Environment Laboratory, Nagoya University, Nagoya 464-8601, Japan
[55] Institute of Space Sciences (CSICIEEC), Campus UAB, Carrer de Magrans s/n, E-08193 Barcelona, Spain
[56] Institució Catalana de Recerca i Estudis Avançats (ICREA), E-08010 Barcelona, Spain
[57] Max-Planck Institut für extraterrestrische Physik, D-85748 Garching, Germany
[58] Praxis Inc., Alexandria, VA 22303, resident at Naval Research Laboratory, Washington, DC 20375, USA
[59] Albert-Einstein-Institut, Max-Planck-Institut für Gravitationsphysik, D-30167 Hannover, Germany
[60] University of Geneva, Département de physique nucléaire et corpusculaire (DPNC), 24 quai Ernest-Ansermet, CH-1211 Genève 4, Switzerland
Received 2019 March 28; accepted 2019 April 25; published 2019 June 13

Abstract

The Large Area Telescope (LAT) aboard the *Fermi* spacecraft routinely observes high-energy emission from gamma-ray bursts (GRBs). Here we present the second catalog of LAT-detected GRBs, covering the first 10 yr of operations, from 2008 to 2018 August 4. A total of 186 GRBs are found; of these, 91 show emission in the range 30–100 MeV (17 of which are seen only in this band) and 169 are detected above 100 MeV. Most of these sources were discovered by other instruments (*Fermi*/GBM, *Swift*/BAT, AGILE, *INTEGRAL*) or reported by the Interplanetary Network (IPN); the LAT has independently triggered on four GRBs. This catalog presents the results for all 186 GRBs. We study onset, duration, and temporal properties of each GRB, as well as spectral characteristics in the 100 MeV–100 GeV energy range. Particular attention is given to the photons with the highest energy. Compared with the first LAT GRB catalog, our rate of detection is significantly improved. The results generally confirm the main findings of the first catalog: the LAT primarily detects the brightest GBM bursts, and the high-energy emission shows delayed onset as well as longer duration. However, in this work we find delays exceeding 1 ks and several GRBs with durations over 10 ks. Furthermore, the larger number of LAT detections shows that these GRBs not only cover the high-fluence range of GBM-detected GRBs but also sample lower fluences. In addition, the greater number of detected GRBs with redshift estimates allows us to study their properties in both the observer and rest frames. Comparison of the observational results with theoretical predictions reveals that no model is currently able to explain all results, highlighting the role of LAT observations in driving theoretical models.

Key words: catalogs – gamma-ray burst: general – methods: data analysis

Supporting material: FITS file

1. Introduction

Observations by the *Fermi Gamma-Ray Space Telescope* in the 10 yr since it was placed into orbit on 2008 June 11 have allowed for the opportunity to study the broadband properties of gamma-ray bursts (GRBs) over an unprecedented energy range. Its two scientific instruments, the Large Area Telescope (LAT; Atwood et al. 2009) and the Gamma-Ray Burst Monitor (GBM; Meegan et al. 2009), provide the combined capability of probing emission from GRBs over seven decades in energy. These groundbreaking observations have helped to characterize the highest-energy emission from these events (Abdo et al. 2009a, 2009e, 2010a; Ackermann et al. 2010a, 2010b, 2011), furthered our understanding of the emission processes associated with GRBs (Ryde et al. 2010; Axelsson et al. 2012; Preece et al. 2014; Ahlgren et al. 2015; Arimoto et al. 2016; Burgess et al. 2016; Moretti & Axelsson 2016), helped place constraints on the Lorentz invariance of the speed of light (Abdo et al. 2009b, 2009c; Shao et al. 2010; Nemiroff et al. 2012; Vasileiou et al. 2013) and the gamma-ray opacity of the universe (Abdo et al. 2010b; Desai et al. 2017), and motivated revisions in our basic understanding of collisionless relativistic shock physics (Ackermann et al. 2014).

The first *Fermi*-LAT GRB catalog was published in 2013 (Ackermann et al. 2013b, hereafter 1FLGC). It is a compilation of the 35 GRBs, including 30 long-duration (>2 s) and 5 short-duration (<2 s) GRBs, detected in the period 2008 August through 2011 July (the first GRB included is GRB 080825C, and the last is GRB 110731A). Of these GRBs, 28 were detected with standard analysis techniques at energies above 100 MeV, while 7 GRBs were detected at only <100 MeV using the LAT Low-Energy (LLE) technique. It established three main observational characteristics of the high-energy emission:

1. Additional spectral components: Many of the bright GRBs observed by *Fermi*-LAT were not well fit with a single Band function (Band et al. 1993). In particular, an additional power-law (PL) component was required to account for the high-energy data of four bursts.
2. Delayed onset: The emission above 100 MeV was systematically delayed compared with the emission seen at lower energies, in the keV–MeV energy range. Delays of up to 40 s have been detected, with a few seconds being a typical value.
3. Extended duration: The emission above 100 MeV also systematically lasted longer than the keV–MeV prompt emission. The flux generally followed a PL decay with time, $F \propto t^{-\alpha}$, with α close to -1.

The 1FLGC also left some open questions regarding GRB properties at high energy, which we plan to address in the 2FLGC:

1. Hyperfluent GRBs: Four GRBs of the 1FLGC hinted at the possibility of a different class of high-energy fluence, significantly greater than the average fluence of the other GRBs. Because of the small sample, the hyperfluent class of GRBs was not significant and its confirmation was left for subsequent observations.

[61] Funded by contract FIRB-2012-RBFR12PM1F from the Italian Ministry of Education, University and Research (MIUR).

2. Late-time temporal decay index: The distribution of the late-time temporal decay index in the 1FLGC was clustered around −1, supporting the hypothesis of an adiabatically expanding fireball as a common origin of the extended emission. Although this scenario could explain all observations, only nine GRBs had enough data to allow the decay index to be determined.
3. Breaks in the late-time light curve: Three GRBs in the 1FLGC showed breaks in the temporal decay at late times, similar to the breaks observed in the X-ray light curves. Exploration of this feature was limited by the small sample and the relatively low significance of the breaks.

Since the publication of the 1FLGC, a number of improvements have been made with regard to LAT data processing. The two major changes concern the development of a new event analysis. Since launch, the LAT event classes have undergone a number of versions (or "passes"), and the latest "Pass 8" analysis constitutes a major improvement on the previous versions. In addition, a new detection algorithm has been developed running in parallel over a range of different timescales. Taken together, this has increased the detection efficiency by over 60% (Vianello et al. 2015), and in particular allows the detection of fainter high-energy GRB counterparts.

This paper presents the second catalog of GRBs detected by the *Fermi*-LAT (2FLGC), covering a 10 yr period, from 2008 August to 2018 August. During this time, the GBM triggered on 2357 GRBs, approximately half of which were in the field of view (FOV) of the LAT at the time of trigger. LAT counterparts are searched for in ground processing, following external triggers provided by the GBM, as well as by other instruments. The LAT instrument is also capable of detecting GRBs through an onboard trigger search algorithm. This is a very rare occurrence and has so far only happened 4 times (see Section 4). In addition, continual blind searches are performed as part of the standard ground processing, to look for untriggered events. These efforts are further described in Ackermann et al. (2016) and Ajello et al. (2018).

In the 2FLGC, we have performed an entirely new, standardized analysis to look for LAT counterparts to all GRB triggers reported during the first decade of *Fermi* operations. In Section 2 we describe the data used in this study, giving first a short description of the *Fermi* instruments, followed by the description of data cuts and sample selection. This is followed in Section 3 by a detailed description of the analysis methods used for detection and localization. We also present the methodology that we followed to characterize the temporal and spectral properties of the detected GRBs. The 2FLGC is focused on the LAT-only properties of the bursts in our sample, and we do not perform any joint spectral analysis of LAT and GBM data. In Sections 4 and 5 we present and discuss our results. Finally, we examine the theoretical implications of our results in Section 6.

2. Data Preparation

The 2FLGC presents analysis done with data from the LAT, i.e., covering energies above 30 MeV for GRBs detected through LLE, and from 100 MeV to 300 GeV for GRBs detected with the standard analysis. However, the GBM provides the vast majority of the GRB triggers and is an integral part of the GRB observations made by *Fermi*. We therefore begin with a brief description of both instruments. This is followed by a more thorough description of the LAT data used for the analysis. Finally, we present the selection of GRB triggers that formed the seed of the catalog.

2.1. Instrument Overview

The LAT is a pair production telescope sensitive to γ-rays in the energy range from ∼30 MeV to more than 300 GeV. The instrument and its on-orbit calibrations are described in detail in Atwood et al. (2009) and Abdo et al. (2009d). The telescope consists of a 4×4 array of identical towers, each including a tracker of 18 x–y silicon strip detector planes interleaved with tungsten foils, followed by an 8.6 radiation length imaging calorimeter made with CsI(Tl) scintillation crystals with a hodoscopic layout. This array is surrounded by a segmented anticoincidence detector made of 89 plastic scintillator tiles that identifies and rejects charged particle background events with an efficiency above 99.97% (Ackermann et al. 2012a).

Whether or not an event is observable by the LAT is primarily defined by two angles: the angle ζ with respect to the spacecraft zenith, and the viewing angle θ from the LAT boresight. The LAT performance—including the dependence of the effective area on energy and θ—is presented on the official *Fermi*-LAT performance web page.[62] In the analysis performed in this catalog, we do not make any explicit cuts on the angle θ; however, the exposure will drop very quickly for θ greater than ∼75°. The wide FOV (∼2.4 sr at 1 GeV) of the LAT, its high observing efficiency (obtained by keeping the FOV on the sky with scanning observations), its broad energy range, its large effective area, its low dead time per event (∼27 μs), its efficient background rejection, and its good angular resolution (the 68% containment angle of the point-spread function is 0.°8 at 1 GeV) are vastly improved in comparison with those of previous instruments such as EGRET (Esposito et al. 1999). As a result, the LAT provides more GRB detections, higher statistics per detection, and more accurate localizations.

The GBM is composed of 12 sodium iodide (NaI) and two bismuth germanate (BGO) detectors sensitive in the 8 keV–1 MeV and 250 keV–40 MeV energy ranges, respectively. The NaI detectors are arranged in groups of three at each of the four edges of the spacecraft, and the two BGO detectors are placed symmetrically on opposite sides of the spacecraft, resulting in an FOV of 9.5 sr. Triggering and localization are determined from the NaI detectors, while spectroscopy is performed using both the NaI and BGO detectors. The GBM flight software continually monitors the detector rates and triggers when a statistically significant rate increase occurs in two or more NaI detectors. A combination of 28 timescales and energy ranges are currently tested, with the first combination that exceeds the predefined threshold (generally 4.5σ) being considered the triggering timescale. Localization is performed using the relative event rates of detectors with different orientations with respect to the source and is typically accurate to a few degrees (statistical uncertainty). An additional systematic uncertainty has been characterized as a core-plus-tail model, with 90% of GRBs having a 3.7° uncertainty and a small tail suffering a larger than 10° systematic uncertainty (Connaughton et al. 2015). The GBM covers roughly four decades in energy and provides a bridge from the low energies (below ∼1 MeV),

[62] http://www.slac.stanford.edu/exp/glast/groups/canda/lat_Performance.htm

where most of the GRB emission takes place, to the less studied energy range that is accessible to the LAT.

For GRBs exceeding a preset threshold for peak flux or fluence in the GBM, an autonomous repoint request (ARR) is sent to the spacecraft flight software. If the GBM request is accepted, a special LAT observation mode is initiated. This will keep the GBM flight software location in the LAT FOV for an extended period of time, typically ∼2.5 hr, subject to observational constraints.

On 2018 March 16, one of the solar array drive assemblies on *Fermi* suffered a malfunction. This led to the LAT and GBM being switched off, and normal science operations were only resumed on April 13. However, as of writing one of the solar panels remains in a fixed position, and a modified rocking strategy has been adopted. As a result, the LAT rocks between the northern and southern sky every week, as opposed to every orbit as before. A further impact is that ARRs have been disabled.

2.2. Sample Selection

The 2FLGC presents the results of a search for high-energy counterparts of GRBs that triggered space instruments and have an available public localization. We considered in particular bursts detected by the GBM, the *Swift* Burst Alert Telescope (BAT; Barthelmy et al. 2005) on board the *Neil Gehrels Swift Observatory* (Gehrels et al. 2004), and the *International Gamma-Ray Astrophysics Laboratory* Soft Gamma-Ray Imager (*INTEGRAL*/ISGRI; Lebrun et al. 2003) on board the *INTEGRAL* satellite (Winkler et al. 2003), or reported by the Interplanetary Network (IPN[63]). In the 10 yr period covered by the 2FLGC, there were 2357 GBM GRB triggers, 876 *Swift*/BAT GRB triggers, 65 *INTEGRAL*/ISGRI GRB triggers, and 83 events reported by the IPN (a few through private communication by the PI K. Hurley). We also considered seven bursts contained in the first catalog of GRBs detected by the *Astrorivelatore Gamma a Immagini Leggero* mini-calorimeter (*AGILE*/MCAL; Galli et al. 2013) and not contained in any other list. After accounting for bursts that triggered more than one instrument, we have a total of 3044 independent GRBs. We use the localizations provided by the GBM, unless a better localization is provided by one of the instruments on board *Swift*, namely, the BAT, the X-ray Telescope (XRT; Burrows et al. 2005), or the UV–Optical Telescope (UVOT; Roming et al. 2005), or by the IPN. All these latter positions are distributed via the Gamma-Ray Burst Coordinates Network (GCN),[64] while the GBM-only localizations are reported in the *Fermi*-GBM online GRB Catalog[65] (hereafter FGGC; see Bhat et al. 2016, for more details).

2.3. LAT Data Cuts and Temporal Selection

For the standard analysis, we use Pass 8 LAT data with energies between 100 MeV and 100 GeV, selecting the time interval around each trigger from 600 s before to 100 ks after the GRB trigger time, and defining a standard region of interest (ROI) around the trigger location of 12°. In order to reduce the contamination of the Earth limb, in some dedicated cases (13 GRBs) we define a smaller ROI with a radius of 8°. It is worth noting that as a final check we look for high-energy events over a larger energy range (up to 300 GeV), as discussed in Section 4.8.

We then use `gtmktime` to select only those time intervals when the center of the ROI has a zenith angle $\zeta < 97°$ (i.e., every point of the ROI has $\zeta < 105°$). For bursts with an initial value of $\zeta > 90°$, we increase our selection to include all time intervals when the center of the ROI has a zenith angle $\zeta < 102°$. This allows us to study the prompt emission of those GRBs that started close to the limb of the Earth. The choice of the event class depends on the timescale on which we detect the signal from the GRB and is described in Section 3.2.

2.4. LLE Data

The LLE technique is an analysis method designed to study bright transient phenomena, such as GRBs and solar flares, in the 30 MeV–1 GeV energy range. The LAT Collaboration developed this analysis using a different approach than the one used in the standard photon analysis, which is based on sophisticated classification procedures (a detailed description of the standard analysis can be found in Atwood et al. 2009; Ackermann et al. 2012a). The idea behind LLE is to maximize the effective area below ∼1 GeV by relaxing the standard analysis requirement on background rejection.

The basic LLE selection is based on a few simple requirements on the event topology in the three LAT subdetectors. First of all, an event passing the LLE selection must have at least one reconstructed track in the tracker and therefore an estimate of the direction of the incoming photon. Second, we require that the reconstructed energy of the event be nonzero.

We use the information provided by the flight software in LLE to efficiently select events that are gamma-ray like. With the release of Pass 8 data, we have also improved the LLE selection. For events with an incident angle $\theta < 40°$, we require that no anticoincidence tiles are in "veto" condition (to suppress charged particle contamination), while for angles greater than 40°, we allow a maximum of two tiles in "veto" condition, but no tracker hits can be found in proximity of the anticoincidence hits. This condition helps prevent suppression of large incident angle gamma-rays due to secondary electrons or positrons interacting with the anticoincidence detector downstream. In order to reduce the number of photons originating from the Earth limb in our LLE sample, we only keep reconstructed events with a zenith angle $\zeta < 90°$ or $\zeta < 100°$ (depending on the location of the GRB). Finally, we explicitly include in the selection a cut on the ROI, i.e., the position in the sky of the transient source we are observing. In other words, the localization of the source is embedded in the event selection, and therefore for a given analysis the LLE data are tailored to a particular location in the sky. The response of the detector for the LLE class is encoded in a response matrix, which is generated using a dedicated Monte Carlo simulation for each GRB, and is saved in the standard `HEASARC RMF` file format.[66] LLE data and the relative response are made available for any transient signal (GRB or solar flare) detected with a significance above 4σ through the `HEASARC FERMILLE` website.[67]

[63] http://www.ssl.berkeley.edu/ipn3/
[64] https://gcn.gsfc.nasa.gov/gcn3_archive.html
[65] https://heasarc.gsfc.nasa.gov/W3Browse/fermi/fermigbrst.html
[66] Described at http://heasarc.gsfc.nasa.gov/docs/heasarc/caldb/docs/memos/cal_gen_92_002/cal_gen_92_002.html#Sec:RMF-format.
[67] http://heasarc.gsfc.nasa.gov/W3Browse/fermi/fermille.html

2.5. Low-energy Data Used for Comparisons

While we do not perform any joint spectral fitting with GBM data in this work, comparisons with the sample of GBM-detected GRBs are both highly interesting and inevitable in order to characterize our sample. For this purpose we use the official data from the FGGC.

In order to perform the comparisons, we use the standard GRB properties that characterize the GRB emission, in particular the onset time and duration (both calculated by GBM in the 50–300 keV energy range), values of peak fluxes (F_P, calculated in 1024 ms and 64 ms intervals for long and short GRBs, respectively), fluences (F, calculated over the time interval used in the GBM spectral analysis, which might not always be coincident with the burst duration), and the spectral parameters of the best-fit model derived by the GBM in the 10–1000 keV energy band. The best fit is determined from the four standard spectral models tested in the GBM time-integrated spectral catalog analysis (see Gruber et al. 2014, for more details), namely, the simple PL, the smoothly broken PL (SBPL), the phenomenological Band function (BAND; Band et al. 1993), and the *Comptonized* model (COMP), which is a subset of the Band function. The latter three models are characterized by a low-energy spectral index α, by a high-energy spectral index β, which in the case of the COMP model goes to minus infinity, and by the energy $E_{\rm peak}$, which describes the peak of the νF_ν distribution.

The classification of GRBs into long and short classes is primarily derived from the low-energy duration as measured by GBM and follows the standard rule that long and short bursts are longer and shorter than 2 s, respectively (Kouveliotou et al. 1993). For bursts that did not trigger GBM and are not included in the FGGC, we use the durations calculated by the Konus-*Wind* instrument in the 20 keV–5 MeV energy range, which have been published in GCN Circulars.

3. Analysis Methods and Procedures

As presented in Section 1, significant improvements have been made to the analysis techniques since the 1FLGC. The two developments with highest impact are the "Pass 8" event analysis and a redesigned detection algorithm. "Pass 8" has been rebuilt from the ground up with respect to previous versions ("Pass 6" was used for the first catalog), resulting in increased sensitivity. It is thoroughly described in Atwood et al. (2013a). In this section, we focus on the improvements to the triggered search and detection algorithms for GRBs used to produce the 2FLGC.

3.1. Analysis Sequence

The procedure followed to produce the catalog is summarized in Figure 1. Each individual step of the analysis is described in detail in the following subsections.

Each input trigger was first run through a detection algorithm as described in Section 3.2. All triggers that passed the criteria for detection in any time window were placed in the list of potential candidates for analysis. This list was manually inspected following the procedure in Section 3.5. Only detections retained after this inspection were passed to the analysis pipeline. Here, analyses were performed to determine a number of key properties for each GRB, such as onset, duration, and spectral parameters. The steps of this analysis are described in Section 3.6.

3.2. The LAT Transient Factory

The LAT Transient Factory (LTF) algorithm was introduced after the publication of the 1FLGC and is presented in Vianello et al. (2015). LTF has been running continuously ever since, looking in real time for GRB counterparts in LAT data. When compared to the old algorithm on the same data set as the first catalog, it returned 50% more GRBs. The adoption of "Pass 8" data has led to a further 10% improvement.

LTF is based on the application of an unbinned maximum likelihood technique. This analysis starts by selecting all the photons detected by the LAT above 100 MeV in a circular ROI with radius r and center ($\alpha_{\rm ROI}$, $\delta_{\rm ROI}$) in a time window starting at the trigger time T_0. Then, the presence of a new point source at a position (α_t, δ_t) is tested by using the likelihood-ratio test (LRT). The null hypothesis for the test is represented by a baseline likelihood model including all point sources from the LAT source catalog (Acero et al. 2015) with all parameters fixed, as well as the Galactic and isotropic diffuse emission templates[68] provided by the *Fermi*-LAT Collaboration (Acero et al. 2016), with the normalizations left free to vary. The alternative hypothesis is represented by the baseline model plus the new point source ("test source"), modeled with a PL spectrum with free index and normalization. The LRT uses as the test statistic (TS) twice the logarithm of the maximum of the likelihood function for the alternative hypothesis (L_1) divided by the maximum of the likelihood function for the null hypothesis (L_0):

$$\mathrm{TS} = 2(\log L_1 - \log L_0). \quad (1)$$

Detailed instructions on how to perform an unbinned likelihood analysis using the *Fermi* Science Tools can be found on the *Fermi* website.[69]

For each trigger, a search is performed on five time windows starting at the trigger time T_0 and ending 10, 100, 500, 4000, and 10,000 s after T_0. This selection slightly differs from the standard LTF real-time analysis, which consists of 10 searches running in parallel over time intervals logarithmically spaced from the trigger time to 10 ks after that, as stated in Vianello et al. (2015). For the 10 and 100 s time windows, we use the Pass 8 `P8R2_TRANSIENT020E_V6` event class and the corresponding response functions; for the longer time windows, the event class `P8R2_TRANSIENT010E_V6` is used. In each time window the LTF starts from the input coordinates and trigger time as measured by the triggering instrument (see Section 2.2) and performs the following steps:

1. *Finding map*: we consider an ROI with radius r centered on the input position and a square grid of side δx inscribed in the ROI with a spacing of 0.°8. The size of the grid is fixed according to the triggering instrument and its typical localization accuracy (statistical + systematic), as well as the typical size of the LAT PSF. Specifically, $\delta x = 32^\circ$ for triggers localized by the GBM that are dominated by systematic uncertainties (Connaughton et al. 2015), $\delta x = 1.^\circ 6$ for *Swift* and *INTEGRAL* triggers, and $\delta x = 5^\circ$ for IPN triggers. The radius of the ROI is chosen as $r = \delta x/2 + 12^\circ$ in order to have enough data around each point in the grid for performing an LRT

[68] `gll_iem_v06.fits` and `iso_P8R3_SOURCE_V2.txt`; https://fermi.gsfc.nasa.gov/ssc/data/access/lat/BackgroundModels.html.
[69] https://fermi.gsfc.nasa.gov/ssc/data/analysis/scitools/likelihood_tutorial.html

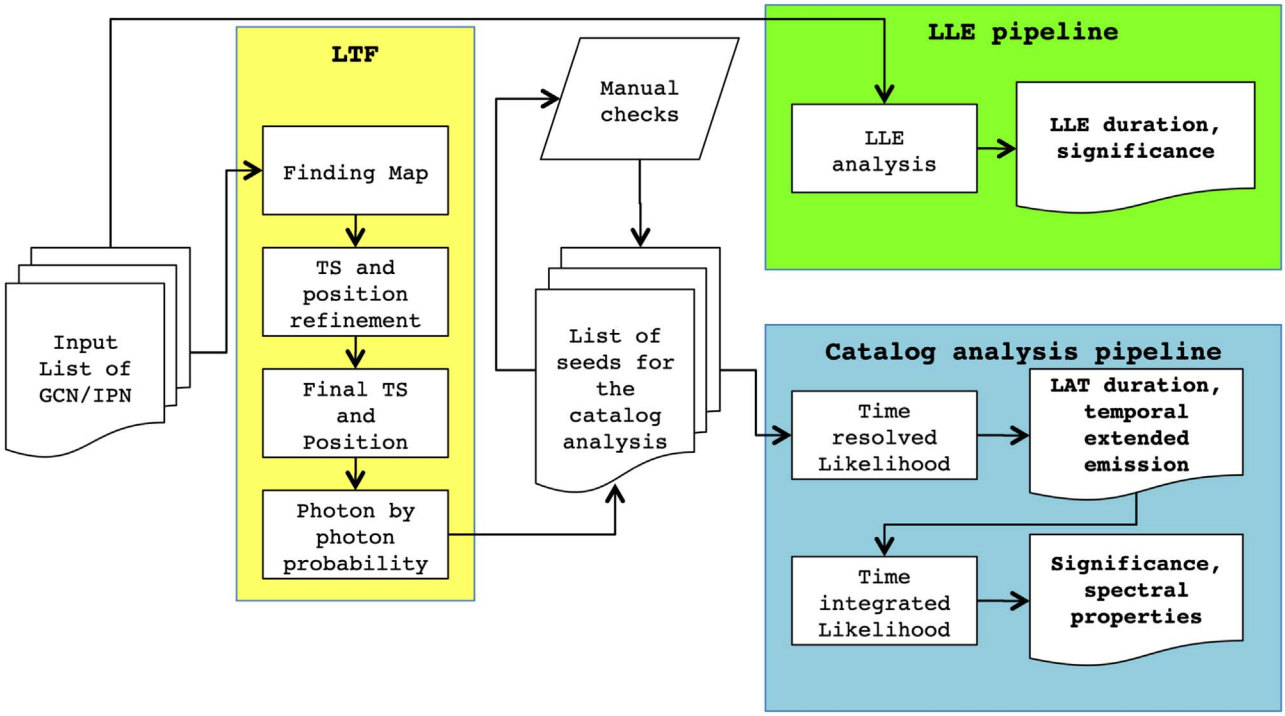

Figure 1. Flow diagram representation of the analysis pipeline. The LTF detection algorithm is highlighted in yellow, and the catalog analysis pipeline, which is executed after manually checking the candidate seeds, is highlighted in blue. The LLE analysis pipeline, which is executed on all input triggers, is highlighted in green. All input candidates are analyzed by the LTF/LLE pipelines; only those passing the detection criteria are retained. Inspection in the manual checks can also lead to rejection of further cases (see text for details).

test (see below). In order to reduce the contamination from the Earth limb—a bright source of γ-rays—all events with $\zeta < 100^\circ$ are filtered out. The effect of this selection is taken into account when computing the exposure by the tool *gtltcube*. We then use the LRT as described above to test for the presence of a source at each position of the grid having at least three photons within 10°. The latter requirement filters out points without any photon cluster around them, in order to reduce the computational cost. The point ($\alpha_{\rm max}$, $\delta_{\rm max}$) in the grid providing the maximum of the TS is considered the best guess for the position of the new transient and marked for further analysis.

2. *TS and position refinement*: we consider an ROI centered on ($\alpha_{\rm max}$, $\delta_{\rm max}$) with a radius of 8°, and we perform an LRT as described above considering only the time intervals within the time window when the border of the ROI is at a zenith angle smaller than 105° ("good time intervals"). This is a different way of reducing the contamination from the Earth limb that is more effective than the one used in the previous step, but it can only be applied on small ROIs. We then use the tool *gtfindsrc* to search for the maximum of the likelihood under the alternative hypothesis (i.e., when the test source is added to the model), varying the position of the test source and profiling the other free parameters. The position (α_1, δ_1) yielding the maximum of the likelihood is considered the new putative position for the candidate counterpart.
3. *Final TS and position*: the previous step is repeated using an ROI centered on (α_1, δ_1) that yields the final TS ($\rm TS_{GRB}$). The tool *gtfindsrc* is run again returning the final estimate of the localization uncertainty.
4. *Photon-by-photon assignment of probability*: we run the tool *gtsrcprob* using the final optimized likelihood model under the alternative hypothesis. This tool assigns to each detected photon the probability of belonging to the test source, i.e., to the candidate counterpart. We then measure the number of photons $N_{p>0.9}$ having a probability larger than 90% of belonging to the candidate counterpart.

The final products of LTF are five sets of results, one for each time window. In order to consider a counterpart detected, we consider in particular $\rm TS_{GRB}$ and $N_{p>0.9}$, as explained in the next section.

3.3. Detection Threshold and False Discovery Rate

A classic result from Chernoff (1954) states that under the null hypothesis the TS of a single LRT as applied in LTF is a random variable that is zero half of the time and is distributed as χ^2 with 1 degree of freedom the other half. This result was confirmed by Monte Carlo simulation in Mattox et al. (1996). Under these circumstances, the significance of the detection (z-score) is $\sqrt{\rm TS}$; thus, a threshold of $\rm TS = 25$ corresponds to a detection $>5\sigma$ for one LRT.

As described in the previous section, LTF consists of multiple LRT procedures and the trial factor needs to be taken into account. The effective number of trials for one time window is, however, difficult to determine because the trials are not independent. Furthermore, we also need to account for the number of time windows and for the number of triggers searched.

To account for the number of triggers searched, we use the procedure proposed by Benjamini & Hochberg (1995). It assumes independent trials and is simple: all the p-values p_i for

all the $n_{\rm tr}$ searches, with $i = 1...n_{\rm tr}$, are sorted in increasing order. We then find k so that p_k is the largest p-value where $p_k \leqslant (k/n_{\rm tr})\alpha$, where α is the error probability for one test. All the triggers with $i = 1...k$ are considered detected. In practice, we first compute through Monte Carlo simulations the effective number of trials for one time window $n_{\rm trw}$. The value of $n_{\rm trw}$ is different depending on the instrument that generated the trigger, and it reflects the size of the finding map (see previous section), so it is larger for larger finding maps. We find $n_{\rm trw} = 110$ for GBM triggers, $n_{\rm trw} = 12.28$ for IPN triggers, and $n_{\rm trw} = 1.25$ for *Swift* and *INTEGRAL* triggers. We then compute the post-trial p-value for one time window by using the binomial distribution as $p_{\rm w} = 1 - (1 - p_{\rm pr})^{n_{\rm trw}}$, where $p_{\rm pr}$ is the p-value coming from the LRT applied to the current time window. There is also another independent trial factor $n_{\rm et}$, which we consider to be equal to the number of time windows where we effectively searched for a counterpart. Note that this is a slightly conservative approach, as the time windows are not independent and thus $n_{\rm et}$ is in reality a little smaller. The number $n_{\rm et}$ can vary from 0 to 5 depending on how many time windows had an exposure larger than zero after our data cuts. For example, if the trigger was never in the FOV or it was always at a zenith angle larger than our cut during a time window, this will not constitute a search, and it will not contribute to $n_{\rm et}$. We can now compute the p-value for a GRB corrected for both the spatial and the time trials as $p = 1 - (1 - p_{\rm w,min})^{n_{\rm et}}$, where $p_{\rm w,min}$ is the minimum $p_{\rm w}$ corresponding to the maximum final $\mathrm{TS_{GRB}}$ found by LTF among the timescales searched. We then apply the Benjamini & Hochberg (1995) procedure using these p-values and correct for the number of triggers searched as explained above.

We further apply the quality cut $n_{\rm p>0.9} \geqslant 3$ to the list of detections, i.e., we require at least three photons with a probability larger than 90% of belonging to the GRB. This neutralizes the effect of isolated high-energy photons ($\gtrsim$10 GeV) within the search region that tend to return high TS values during the unbinned analysis but also very hard spectra, with photon indices close to 0. Moreover, three photons are required in order to have both the normalization and the photon index free during the likelihood maximization under the alternative hypothesis and still have at least 1 degree of freedom.

3.4. The Bayesian Blocks Burst Detection Algorithm for LLE Data

In order to detect GRB counterparts in LLE data, we use a counting analysis based on the well-known Bayesian blocks (BB) algorithm of Scargle et al. (2013). The BB algorithm is capable of dividing a time series into intervals of constant rate, opening a new block only when the rate of events changes in a statistically significant way. In particular, we use the unbinned version of the algorithm, which presents as the only parameter the probability p_0 of opening a new block when the rate is constant (false positive). However, before we can apply the BB algorithm, we need to introduce a preprocessing step to account for the time-varying background in LLE data. Otherwise, the BB algorithm will find many blocks following the variation in the event rate owing to the variations in the background.

We start by fitting a polynomial function to the data in two off-pulse time windows, one before and one after the trigger window, as shown in the left panel of Figure 2 for GRB 131014A. The trigger window is defined on the basis of the duration measured by the GBM in the 50–300 keV energy range. Then, we exploit the fact that a nonuniform Poisson process with expected value $\lambda(t)$ can be converted to a uniform one by transforming the time reference system to

$$t' = \int_0^t \lambda(t)dt. \quad (2)$$

In our case $\lambda(t)$ is the expected number of events of the time-varying background as modeled by the polynomial. We then transpose the time series of LLE events to the t' time reference system and apply the standard BB algorithm. If more than one block is found in the trigger window, it means that there is a rate change on top of what is predicted by the background model. We then deem the transient detected, and we transform back to the original time reference system to yield the time interval of the detection. For all searches we use $p_0 = 10^{-3}$. The analysis is illustrated in the right panel of Figure 2, which shows the final BB representation of the light curve for GRB 131014A.

3.5. Final Manual Checks

The normalization of the Galactic and diffuse templates is allowed to vary in the analysis, but the parameters for the point sources are kept fixed to the values found in the updated *Fermi*-LAT point-source list.[70] This means that the algorithm can potentially pick up non-GRB sources, such as AGN flares. Moreover, GRBs detected far from zenith might also suffer from Earth limb contamination. Therefore, a final manual check of all potential detections was also performed. The list of detections derived by the LTF pipeline previously described was divided into random subsets of bursts that were assigned for analysis to the members of the *Fermi*-LAT GRB team. Each putative event was independently cross-checked by two people, whose task was to either confirm or reject the detection. In case of agreement, the classification was seen as final; otherwise, the case was reviewed by a third person.

The manual checks included a series of tasks to be carried out. First, the LTF results were evaluated in each of the five temporal intervals, taking into account (1) the number of photons with probability >90%, (2) the distance to the nearest known source, (3) the localization error, (4) the spectral index, and (5) the final TS value. We identified many "simple" cases, in which both the number of detected photons was high and the final TS was above 80 in several time intervals, and no other known sources were present in the ROI. These candidates were marked as confirmed with no further inspection.

Intermediate cases that needed deeper investigations included (1) cases where the final TS in all time intervals was close to the threshold, (2) cases where only three to four high-energy photons were detected, (3) cases where a bright source (an AGN, solar flares, etc.) was at an angle $<1^\circ$ from the GRB candidate in the ROI, and (4) cases where a high TS value was obtained only by integrating over the longest timescale (from 0 to 10,000 s; see Section 3.2). In order to check for other active sources in the ROI around the time of the GRB trigger, we looked for flaring blazars using the publicly available FAVA tool[71] (Ciprini et al. 2013; Abdollahi et al. 2017), and for solar activity we checked the Solar Monitor public pages.[72]

[70] https://fermi.gsfc.nasa.gov/ssc/data/access/lat/fl8y/
[71] https://fermi.gsfc.nasa.gov/ssc/data/access/lat/FAVA/
[72] http://www.solarmonitor.org

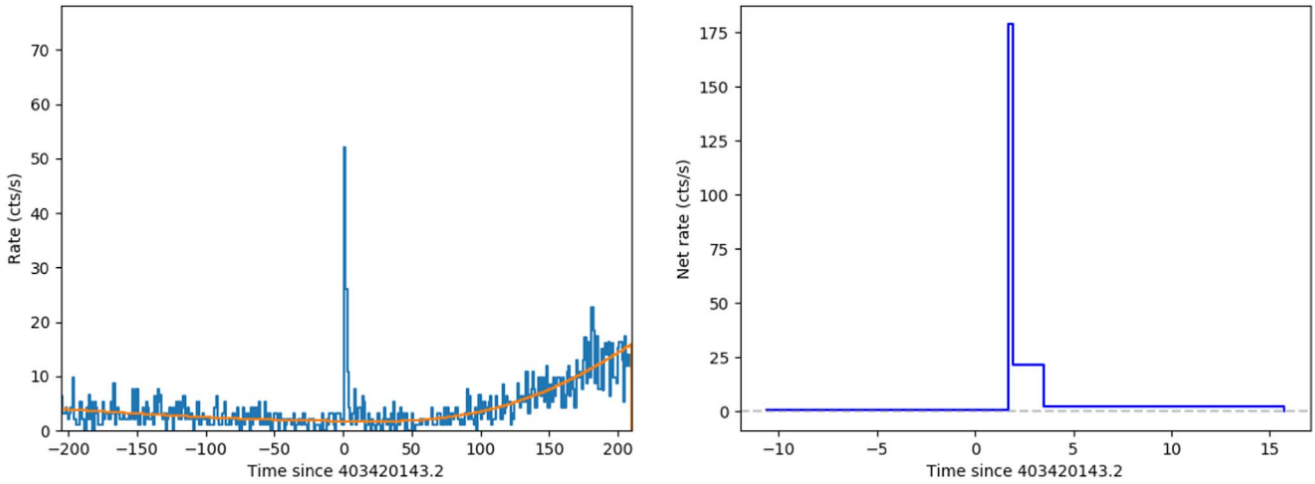

Figure 2. Left panel: LLE light curve of GRB 131014 in the 30 MeV–1 GeV energy range. The polynomial fit to the background is marked by a red line. Right panel: BB representation of the light curve of GRB 131014. All light curves are centered around the GBM trigger time $T_0 = 403420143.2$ (in MET).

Table 1
Definition of the Four Time Intervals (with Start and Stop Times) Used in the Time-integrated Spectral Analysis

Name	Interval	Description
GBM	$[T_{\rm GBM,05}, T_{\rm GBM,95}]$	GRB duration measured by GBM in the 50–300 keV energy range
LTF	$[T_0, T_{\rm max}^{\rm LTF}]$	Time interval showing the highest TS value as calculated by the LAT transient factory, starting from the GRB trigger time
LAT	$[T_{\rm LAT,0}, T_{\rm LAT,1}]$	GRB duration measured by LAT by performing a time-resolved likelihood analysis in the 100 MeV–100 GeV energy range
EXT	$[T_{\rm GBM,95}, T_{\rm LAT,1}]$	Interval from end of GBM to end of LAT duration

In case of particularly uncertain candidates, we performed an ad hoc likelihood analysis, similar to the one performed by the LTF pipeline, but running on dedicated time intervals that might differ from the catalog ones.

Through these manual checks, ∼15%–20% of the examined cases were rejected as not connected to a GRB. The remaining events were processed in the dedicated analysis pipeline.

3.6. Catalog Analysis Description

In this section we describe the analysis steps we performed on each GRB of the final sample. The idea is to perform an automated analysis, which is implemented in a series of `python` scripts that are used to control the various steps. The analysis is based on `ScienceTools v11r05p03`, available for download at the *Fermi* Science Support Center.[73]

3.6.1. Time-integrated Likelihood Analysis

We perform an unbinned likelihood analysis in four different time intervals. The "GBM" time interval represents the GRB duration as given by $T_{\rm GBM,90}$ reported in the FGGC. $T_{\rm GBM,90}$ is the interval during which the instrument measures from 5% to 95% of the total GRB flux in the 50–300 keV energy range (i.e., from $T_{\rm GBM,05}$ to $T_{\rm GBM,95}$). The "LTF" interval corresponds to the time interval in the LAT Transient Factory analysis where the highest TS was found. The "LAT" interval encompasses the signal detected by the LAT, as defined in 3.6.2. The "EXT" interval is defined as the time interval including LAT emission (if any) after the $T_{\rm GBM,95}$. Table 1 summarizes the definition of these intervals.

[73] https://fermi.gsfc.nasa.gov/ssc/data/analysis/

3.6.2. Time-resolved Likelihood Analysis

In order to perform time-resolved likelihood analysis, we have developed an algorithm for adaptively binning the LAT events. Starting from the result of the analysis in the "LTF" time window, we apply `gtsrcprob` to calculate the probability of each LAT event to be associated with the GRB source. Starting with preselected logarithmically spaced time bins (48 bins from 0.01 s to 50 ks after the GBM trigger), we merge them until at least three events with probability >0.9 are present in each final bin. In practice, we have 3 degrees of freedom ($N_{\rm dof}$): 2 associated with the PL describing the GRB, and 1 with the normalization of the isotropic diffuse component. The normalization of the Galactic model has been fixed to its nominal value (1). We require at least $N_{\rm dof}$ events with probability >0.9 in every bin. In this way, we optimize the duration of the time intervals in order to always have enough photons to perform the fit. Once we have identified the time bins, we perform unbinned likelihood analysis in each bin, calculating the value of flux or, in the case of a TS value <10, we calculate the flux upper limit (95%) by profiling the likelihood function.

In the 1FLGC, the duration in the LAT was calculated based on the concept of $T_{\rm GBM,90}$, i.e., the time during which 90% of the flux is collected. As the LAT observes each photon individually, this requires the simulation of light curves. In this analysis, we instead use a technique based on the individual photons intrinsic to the LAT. The total duration of the signal in the LAT, defined as $T_{\rm LAT,100}$, is estimated starting from the results of the time-resolved analysis. The LAT onset time $T_{\rm LAT,0}$ corresponds to the time when the first photon with probability $p > 0.9$ to be associated with the GRB is detected,

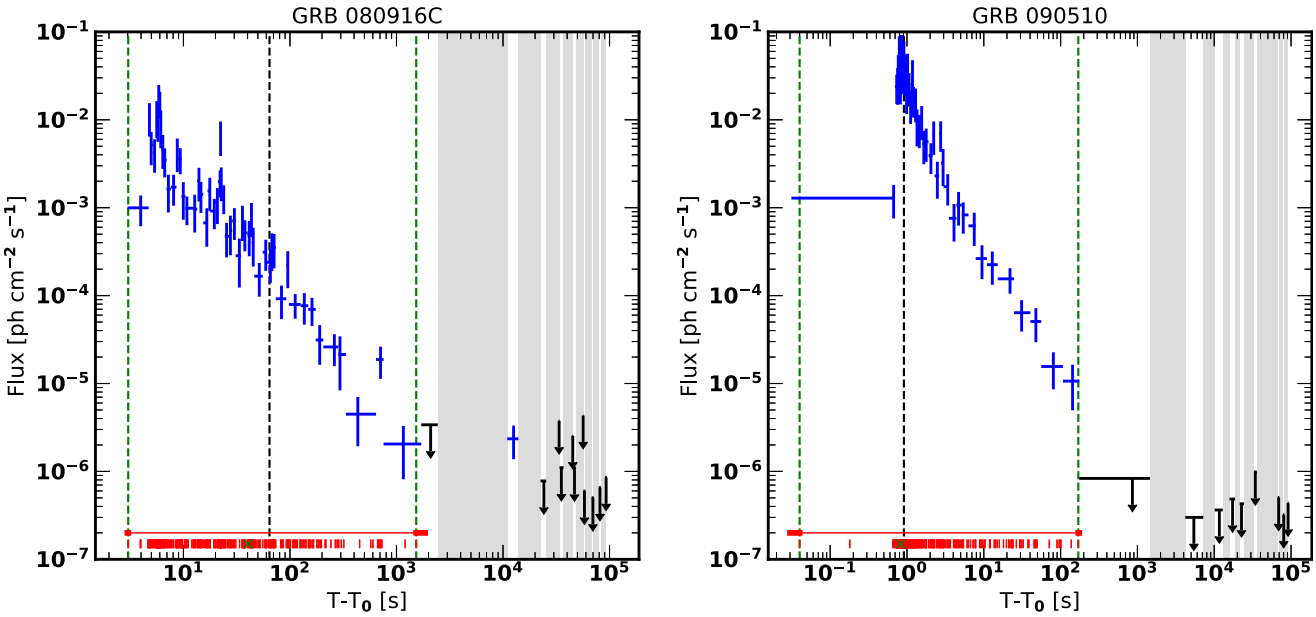

Figure 3. Temporal extended emission for two bright LAT GRBs, the long GRB 080916C (left panel) and the short GRB 090510 (right panel). Blue points show the flux in each time bin, while black arrows mark upper limits. The green vertical dashed lines indicate the first and the last LAT-detected event, while the vertical dashed black line marks the end of the GBM emission ($T_{\rm GBM,95}$). Shaded gray areas mark intervals when the GRB is outside the FOV. The red vertical markers at the bottom of each panel indicate the arrival times of the events with probability >0.9 to be associated with the GRB, with the green cross being the event with maximum energy. The horizontal red line indicates the estimated duration of the GRB ($T_{\rm LAT,100}$).

while $T_{\rm LAT,1}$ corresponds to the last event with $p > 0.9$. $T_{\rm LAT,100}$ of the signal is simply $T_{\rm LAT,1} - T_{\rm LAT,0}$. These are also the quantities that define the "LAT" time interval, as previously discussed (see Table 1).

In order to correctly estimate the uncertainty on $T_{\rm LAT,1}$ ($\delta T_{\rm LAT,1}$) for an event with n detected photons with probability $p > 0.9$, we define $\Delta t_{n-1,n}$ as the time interval between the second-to-last and the last event. Assuming Poisson statistics, the probability to measure an event between t and $t + dt$ is $P(t, t + dt) = \lambda\, dt$, where λ is the rate: in our case $\lambda = 2/\Delta t_{n-1,n}$. Therefore, we conservatively compute the uncertainty as $\delta T_{\rm LAT,1} = 1/\lambda = \Delta t_{n-1,n}/2$. Similarly, considering the first two events with probability $p > 0.9$, we define the uncertainty on $T_{\rm LAT,0}$ as $\delta T_{\rm LAT,0} = \Delta t_{1,2}/2$. The error on $T_{\rm LAT,100}$ follows using standard error propagation.

In order to better illustrate this analysis, Figure 3 shows two light curves of two bright GRBs, the long GRB 080916C (left panel) and the short GRB 090510 (right panel). For the long burst, the arrival time of the last event is substantially smaller than the end of the bin of the last detection. This could indicate that in the last bin the GRB is only marginally detected. For most of the other bursts, the arrival time of the last event is very close to the end of the last bin with positive detection, as in the case of GRB 090510.

3.6.3. Calculation of Energetics

In addition to reporting the flux and fluence of each GRB, for the subset of GRBs with measured redshift z we also calculate their total radiated energy ($E_{\rm iso}$). Starting from the measured spectrum of each burst, this is done by using the best-fit model over a specific energy range and by assuming that the energy emitted by a GRB at the source in the cosmological source frame is isotropically radiated. The isotropic radiated energy is defined by following expression:

$$E_{\rm iso} = \frac{4\pi\, d_L^2}{1+z}\, S(E_1, E_2, z), \tag{3}$$

where d_L is the luminosity distance and $S(E_1, E_2, z)$ is the fluence integrated between the minimum energy E_1 and the maximum energy E_2. It can be expressed as

$$S(E_1, E_2, z) = T_{100} \int_{E_1/(1+z)}^{E_2/(1+z)} E\, N(E) dE. \tag{4}$$

Here $N(E)$ describes the best-fit spectral model, and T_{100} represents the total duration of the burst as defined in the previous section. LAT data are always fit with a simple PL model in the energy range 100 MeV–10 GeV, i.e.,

$$N(E) = AE^{\Gamma}. \tag{5}$$

Finally, assuming a spatially flat universe ΛCDM model with $\Omega_\Lambda = 0.714$, $\Omega_M = 0.286$, and $H_0 = 69.6$ km s^{-1} Mpc^{-1} (Bennett et al. 2014; Planck Collaboration et al. 2016), the luminosity distance is given by (Weinberg 1972)

$$d_L(z, \Omega_\Lambda, \Omega_M) = (1+z)\frac{c}{H_0}\int_0^z \frac{dz'}{\sqrt{\Omega_M(1+z')^3 + \Omega_\Lambda}}. \tag{6}$$

3.6.4. Localization

The LTF algorithm described in Section 3.2 returns the position of the GRB, as well as its detection probability. The steps of the procedure include refining the source location, and the position given in the final step is taken as the definitive one; no further optimization is performed.

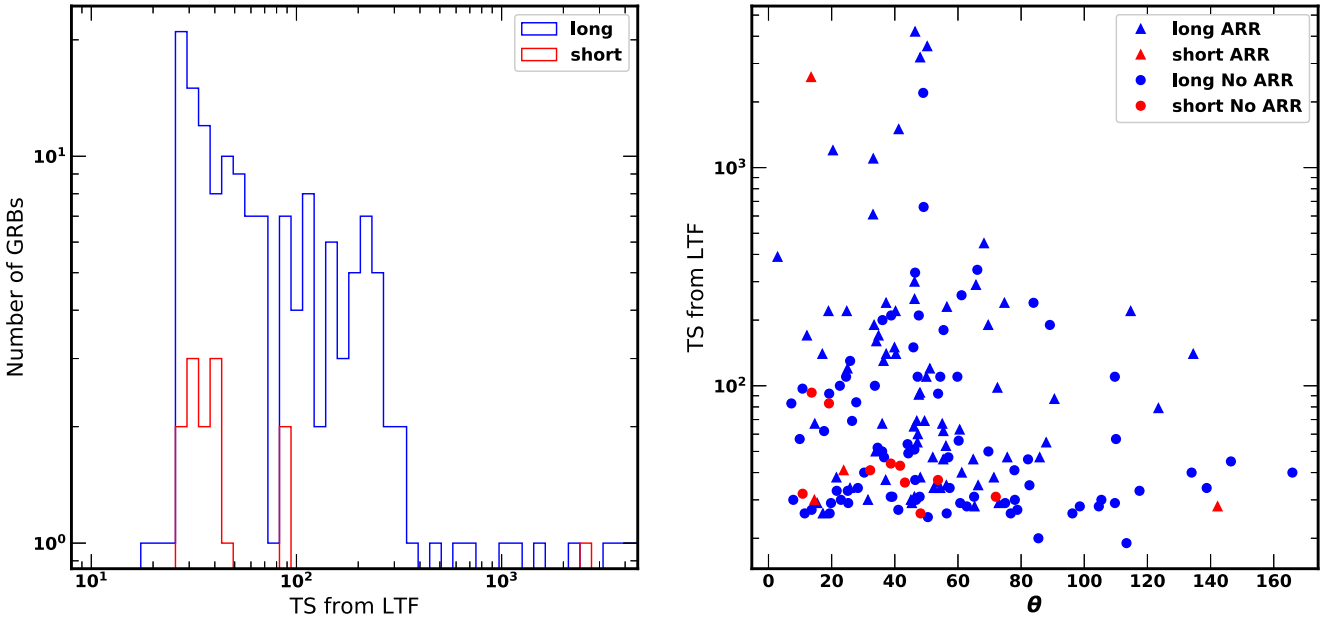

Figure 4. Left panel: distribution of the TS for 14 short (red) and 155 long (blue) GRBs detected by the LTF algorithm. Right panel: TS values for long and short bursts as a function of the angle θ at the trigger time. Bursts that triggered an ARR are marked with a triangle.

3.6.5. LLE Light Curve and Duration

The BB burst detection algorithm described in Section 3.4 provides a way of binning the data taking into account background fluctuations: blocks are defined only when an intrinsic rate variation above the background is detected, as opposed to an absolute variation. In our analysis we therefore define the onset of the LLE signal ($T_{\rm LLE,05}$) as the starting time of the first block above background. Similarly, we define the $T_{\rm LLE,95}$ as the ending time of the last block above background. The LLE duration ($T_{\rm LLE,90}$) is simply defined as $T_{\rm LLE,95}$–$T_{\rm LLE,05}$.

4. Results

In the following subsections, we examine the main results of our analysis. The focus will be on the properties of the overall population, rather than a presentation of individual GRBs.

4.1. LAT Detections

This 10 yr catalog comprises 186 detections, 17 short GRBs (sGRBs), and 169 long GRBs (lGRBs). Adopting the analysis methods described in Section 3, we detect 169 GRBs with our likelihood analysis above 100 MeV. Of these, 155 are lGRBs and 14 are sGRBs. The distribution of the TS obtained by the LTF algorithm is shown in the left panel of Figure 4. The distribution peaks at relatively low values of TS (∼30) and then smoothly falls with increasing TS value. Only a handful of GRBs (∼5%) form a tail at very high TS (above 1000).

Using the LLE technique, 91 GRBs are found below 100 MeV. Out of those, 85 are lGRBs and 6 are sGRBs. Moreover, 17 of these GRBs (of which 2 are sGRBs) are found only with the LLE technique and are not detected at higher energies with the LAT standard analysis chain.

Of all 3044 triggers in our initial list, we thus detect ∼6% at high energies with the LAT. About 18% of the LAT-detected bursts were outside the nominal FOV of the LAT at the time of the trigger. We note that the position in the sky of events that were outside the FOV at trigger time may have entered the FOV at a later time. Moreover, in 10 yr 220 triggers initiated an ARR of the satellite, a small fraction (<10%) of which are caused by other sources, such as solar flares or particle events. Of these ARRs, 83 successfully resulted in LAT detection. The distribution of the LTF TS values as a function of θ at the trigger time is shown in the right panel of Figure 4. The highest TS values are seen for GRBs with $\theta < 50°$.

Furthermore, this catalog includes four GRBs that triggered the LAT directly: one short burst, GRB 090510, and three long ones, GRB 131108A, GRB 160509A, and GRB 160821A. This underscores that onboard LAT GRB detections are relatively rare, implying exceptional brightness in high-energy gamma-rays. It is worth noting that the very bright GRB 130427A did not result in LAT onboard trigger, since the GBM had triggered and issued an ARR on the first emission peak (Preece et al. 2014), which was very bright at low energies but not particularly strong above 100 MeV.

Figure 5 shows the position in equatorial coordinates of 2357 GBM GRB triggers (gray symbols) detected over the 10 yr period of the catalog. A total of 160 lGRBs and 16 sGRBs also detected by LAT are marked by blue and red asterisks, respectively. In fact, out of the 169 likelihood-detected GRBs, 10 did not trigger the GBM instrument. Of these, two GRBs triggered *Swift*-BAT, namely, GRB 081203A and GRB 130907A, while six GRBs were reported by the IPN: GRB 090427A, GRB 110518A, GRB 120911B, GRB 140825A, the short GRB 160702A, and GRB 180526A. While GRB 120911B did not trigger GBM, it was the only burst to be later found in on-ground analysis of GBM data and announced by Gruber et al. (2012). Furthermore, we report for the first time the detection of GRB 100213C and GRB 111210B. These triggers were reported via private IPN communication, as stated in Section 2.2.

A list of all LAT detections is given in Table 2. For each event, we state the trigger date and time (both in UT and in MET), the final LTF localization with error, the off-axis and zenith angles at trigger time, whether an ARR was issued, the likelihood TS value and LLE significance, the redshift, and the references to the corresponding GCN circulars published by the LAT Collaboration. For those events detected only with the

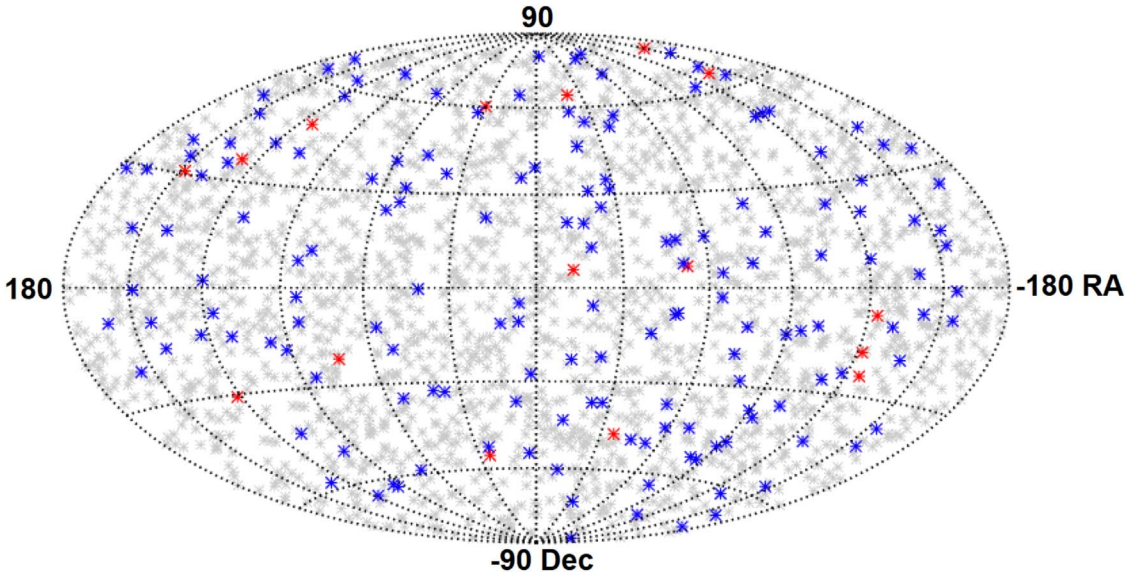

Figure 5. Sky distribution of 2357 GBM-triggered GRBs (from 2008 July 14 to 2018 July 31) in equatorial coordinates (gray asterisks). Blue (red) asterisks indicate 160 (16) long (short) LAT-detected GRBs included in the 2FLGC over the same time period.

LLE technique, we report the best possible localization of the burst as determined by, e.g., GBM or *Swift*.

In our sample, 34 GRBs have a measured redshift (19%), as compared to 10 (29%) in 1FLGC. For comparison, the fraction of *Swift*-detected bursts with redshift is ∼29%.[74] The smaller fraction of LAT bursts with a measured redshift in the 2FLGC with respect to the 1FLGC is not surprising, as ∼50 new GRBs were discovered by our analysis, which have not been previously reported to the community. In addition, the improvements to the analysis techniques enable us to detect fainter GBRs, which are more difficult targets for follow-up observations.

On average, the (90% containment, statistical only) uncertainty in LAT detections is 0.°36 with a range from 0.°04 to 2.°0. In order to assess the LAT location accuracy, we also checked for joint detections by *Fermi*-LAT and *Swift* and found that 75 bursts (∼40%) have a BAT position, while 67 bursts (∼36%) have an XRT position. By comparing LAT and *Swift*/XRT localizations of the codetected GRBs, we find that ∼70% of the *Swift* localizations are inside the LAT 90% confidence region. The majority of the remaining XRT positions are only marginally outside the LAT region, indicating that the LAT localization error is slightly underestimated (∼0.°1).

4.1.1. Comparison with the First LAT GRB Catalog

The changes and improvements in the 2FLGC mean that the results reported here will differ from those in the 1FLGC. In the time interval of the 1FLGC, 2008 August to 2011 July (3 yr), we now recover more events: instead of 28 standard likelihood detections, we now have 50 detections. Three of these new detections are short GRBs, namely, GRB 081102B, GRB 090228A, and GRB 110728A. Four of the new detections come from non-GBM triggers.

The 1FLGC included 21 GRBs also detected with the LLE technique below 100 MeV. During the same period, we now find 25 LLE detections. Four of those—GRB 090531B, GRB 100225A, GRB 101123A, and GRB 110529A—are LLE-only bursts as reported also in the 1FLGC, with the first and the last one being short GRBs. The total number of LLE-only detections is lower with respect to the 1FLGC, where we retrieved seven LLE-only bursts. Indeed, this is not surprising, since we now detect more events with the likelihood analysis thanks to Pass 8 and to the improved LTF pipeline.

As a result of the new analysis, we do not include in the current catalog two events that were included in the 1FLGC: GRB 091208B and GRB 110709A. Both GRBs were long, with estimated LAT durations of ∼40 s; however, only three photons were detected for each GRB, and their detection was marked as marginal. The highest-energy photon in GRB 091208B was 1.2 GeV, while GRB 110709A had no detected emission above 500 MeV. By selecting Pass 8 data and applying the new detection algorithm, the significance of these two detections further decreased, thus resulting in their exclusion from the 2FLGC.

4.1.2. LAT Detections after 2011 July

We have also cross-checked the current catalog with the LAT detections that were publicly announced through GCN Circulars in the time period from 2011 July until 2018 August. Using the standardized catalog analysis described in Section 3.2, we now detect 31 previously unreported GRBs, for which no GCN has been issued. As expected, this is a much smaller relative increase than during the period of the 1FLGC, since Pass 8 data and the improved detection algorithm have been used since 2015.

Moreover, we do not retrieve eight GRBs that have previously been publicly announced by the *Fermi*-LAT Collaboration, namely, GRB 120916A (GCN 13777), GRB 130206A (GCN 14190), GRB 131018B (GCN 15357), GRB 140329A (GCN 16047), GRB 150127A (GCN 17356), GRB 150724B (GCN 18065), GRB 161202A (GCN 20229), and GRB 170810A (GCN 21452). In general, these are all GRBs that at the time of detection were reported with low significance, or with few photons. All these cases were analyzed at the time of the GCN writing either on ad hoc time intervals chosen by the burst advocates or on the 10 real-time LTF temporal windows. These differ from the five fixed time intervals chosen for the catalog analysis presented in Section 3.2, thus leading to different results. GRB 130206A and GRB 150127A were previously reported through GCNs as marginal LLE detections, both with a significance $<3\sigma$, again not matching the current catalog requirements.

[74] https://swift.gsfc.nasa.gov/archive/grb_table/

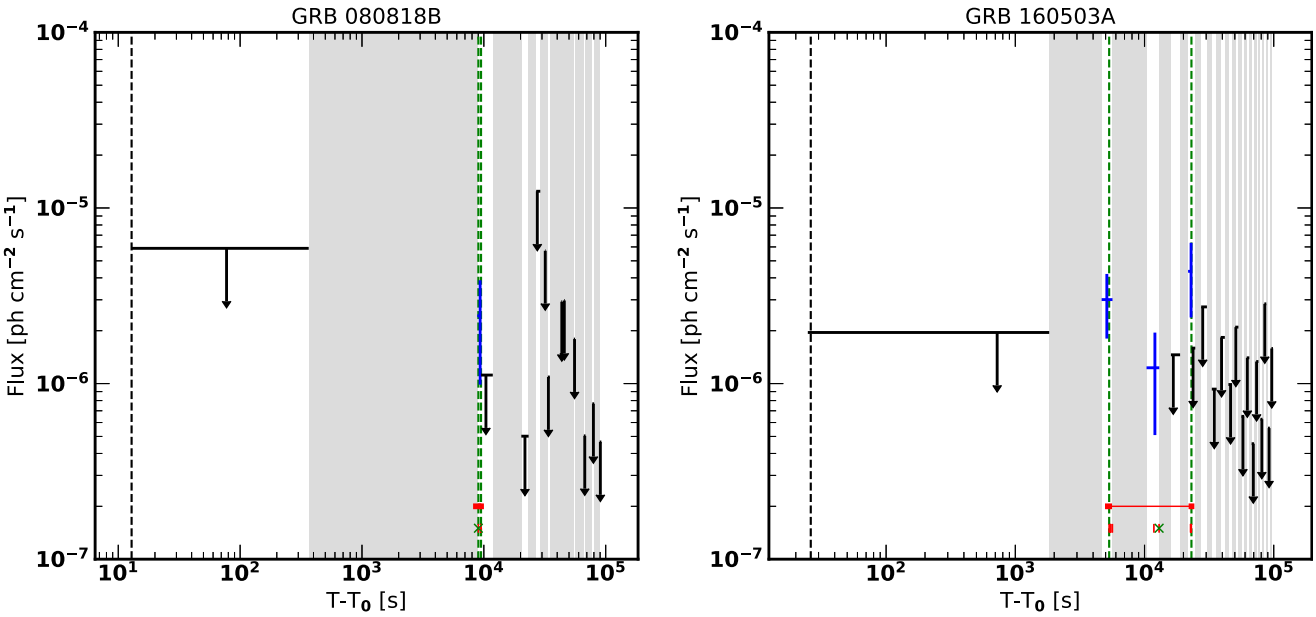

Figure 6. Temporal extended emission for two GRBs detected by LAT at very late times, namely, GRB 080818B (left panel) and GRB 160503A (right panel). Markers and colors are the same as in Figure 3.

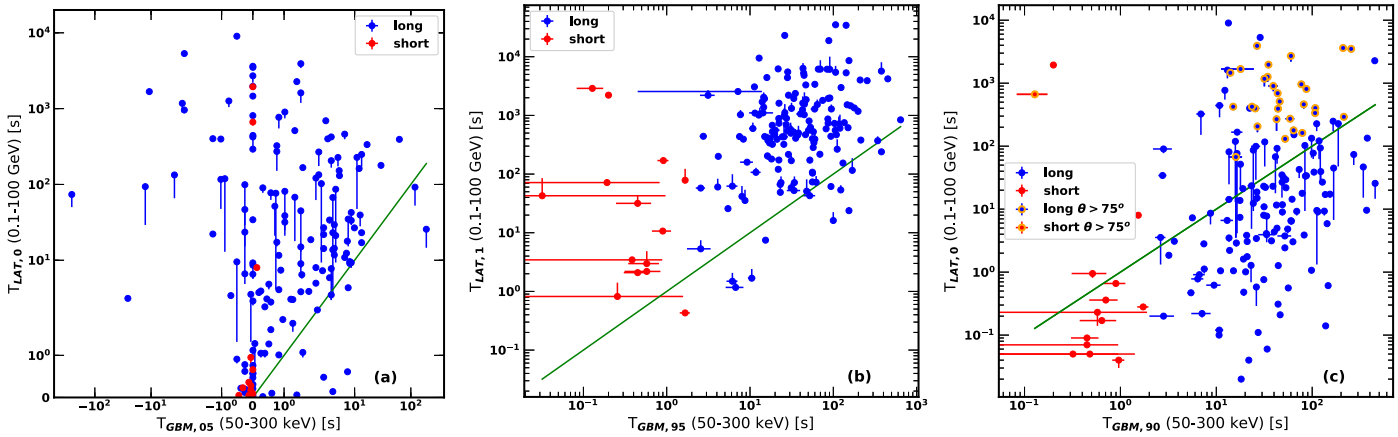

Figure 7. (a) $T_{\rm LAT,0}$ and (b) $T_{\rm LAT,1}$ calculated in the 100 MeV–100 GeV energy range vs. the same quantities calculated in the 50–300 keV energy range. Panel (c) shows the onset times ($T_{\rm LAT,0}$) in the 100 MeV–100 GeV vs. the durations ($T_{\rm GBM,90}$) in the 50–300 keV energy range. The solid line denotes where values are equal. Blue and red circles represent long and short GRBs, respectively. In panel (c), we additionally mark the GRBs that were outside the FOV at trigger time with a thick orange contour.

4.2. LAT Onset Times and Duration

In the following paragraphs we discuss the temporal properties of the bursts in our sample. As presented in Section 2.5, the classification of GRBs into long and short classes is derived from the low-energy duration as measured by GBM in the 50–300 keV energy band. The LAT durations are calculated in the 100 MeV–10 GeV energy range. Table 3 summarizes the various temporal characteristics of the GRBs in our catalog. This includes the values of $T_{\rm GBM,05}$, $T_{\rm GBM,95}$, and $T_{\rm GBM,90}$ for GBM; $T_{\rm LLE,05}$, $T_{\rm LLE,95}$, and $T_{\rm LLE,90}$ for LLE; and $T_{\rm LAT,0}$, $T_{\rm LAT,1}$, and $T_{\rm LAT,100}$ for the LAT. Two GRBs, GRB 100213C and GRB 111210B, were reported only by the IPN through private communication: we do not provide any duration information for those. We mark all non-GBM durations in Table 3 with an asterisk in the $T_{\rm GBM,05}$ column.

For some GRBs, the LAT detection of the first photon occurs at very late times. This could be due to high-energy photons not being emitted during the initial phase, but it could also be due to observational constraints, where the GRB location is outside the FOV for long intervals. This is illustrated for two GRBs in Figure 6. In both panels, blue points are photon flux measurements, while upper bounds are displayed as black arrows. In the left panel, the first shaded gray area marking when GRB 080818B was outside the FOV spans almost 10 ks ($T_{\rm LAT,0} = 9.0 \pm 0.6$ ks). The estimated duration of the burst, $T_{\rm LAT,100} = 500 \pm 200$ s, is almost not visible owing to the late time of the detection. Similarly, in the right panel, the first detection of GRB 160503A occurs at 5.3 ks, again after a period of several kiloseconds where the burst was first not detected and then outside the FOV. In this case, the duration was $T_{\rm LAT,100} \sim 18$ ks.

In Figure 7(a) we compare the onset times estimated in the LAT energy band (100 MeV–100 GeV) with the ones estimated in the GBM energy band (50–300 keV). A negative $T_{\rm GBM,05}$ value in the low-energy band means that the burst

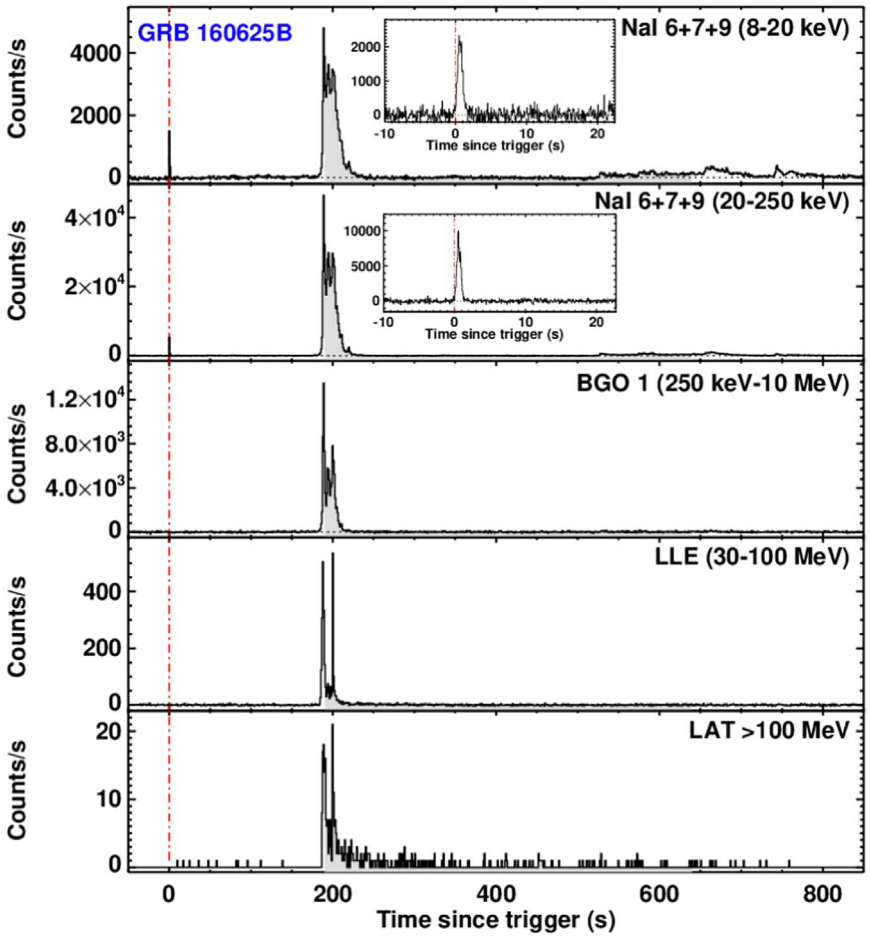

Figure 8. Composite light curve of GRB 160625B: summed GBM/NaI detectors (first two panels), GBM/BGO (third panel), LLE (fourth panel), and LAT rates above 100 MeV (bottom panel). The gray shaded area indicates the $T_{\rm GBM,90}$ calculated in the 50–300 keV energy range. The dashed red lines marks the GBM trigger time. A zoom-in around trigger time is shown in two insets for each energy range of the NaI detectors, highlighting the peak detected at low energies that caused the trigger in GBM. This peak does not show any counterpart at higher energies. The association of the low-energy (<250 keV) late-time emission (from 500 to 800 s post-trigger) with the main GRB emission episode has been cross-checked by the GBM Team (FGGC).

onset occurred before the trigger time. In general, we notice that the high-energy emission starts significantly later with respect to the low-energy one, for both long and short bursts. Burst durations are compared in panel (b) of the same figure. Here, the end of the signal at high energies ($T_{\rm LAT,1}$) appears to be significantly later than the one measured in the GBM energy band. Both these characteristics were already reported in the 1FLGC. Our results confirm and strongly support the claim that when high-energy emission is observed in GRBs, this emission is delayed and lasts longer compared to that in the low-energy band.

In Figure 7(c) we show the onset time ($T_{\rm LAT,0}$) of the high-energy emission versus the burst duration ($T_{\rm GBM,90}$) in the 50–300 keV range. It is worth noting that the $T_{\rm LAT,0}$ of the majority of GRBs (both long and short ones) occurs before the prompt emission measured by the GBM is over. Events that were outside the nominal LAT FOV (∼75°) at the time of the GBM trigger are marked with thick orange contours. They compose the majority of GRBs where the onset of the high-energy emission came after the low-energy emission had faded, indicating that most such events are due to observational bias. This effect will be further investigated below.

As shown in panels (a) and (b) of Figure 7, there are just a few outliers that have high-energy emission that is not delayed and/or has shorter duration compared to the low-energy band. However, since the procedure to calculate onset times and durations differs between the two energy ranges, we caution that further analysis is needed before strong conclusions can be drawn about individual GRBs. The difference is in most cases less than a few seconds. The most prominent outlier to the right of the line is GRB 160625B, where the GRB $T_{\rm GBM,05}$ is ∼190 s, whereas $T_{\rm LAT,0}$ is ∼25 s. However, this burst showed three emission episodes spread over a period of more than ∼10 minutes, as shown in Figure 8. The first one triggered the GBM, a second one 3 minutes later resulted in LAT onboard trigger, and then the GBM triggered again 10 minutes after the first trigger. It is thus not surprising that the $T_{\rm GBM,05}$ is much greater than the arrival time of the first LAT photon.

Short GRBs in general have more similar onset times in LAT and GBM. They also exhibit shorter durations in the high-energy range, although they last still significantly (generally more than an order of magnitude) longer than at lower energies. The short GRB 170127C is the short burst with the longest-lasting high-energy duration, more than 2 ks.

In our sample, 16 GRBs have high-energy emission lasting over 5 ks, and four have durations over 10 ks, namely, GRB 160623A (∼35 ks), GRB 130427A (∼34 ks), GRB 140810A (∼18 ks), and GRB 160503A (∼18 ks). Figure 9 shows the temporal extended emission for the two longest bursts, GRB 130427A in the left

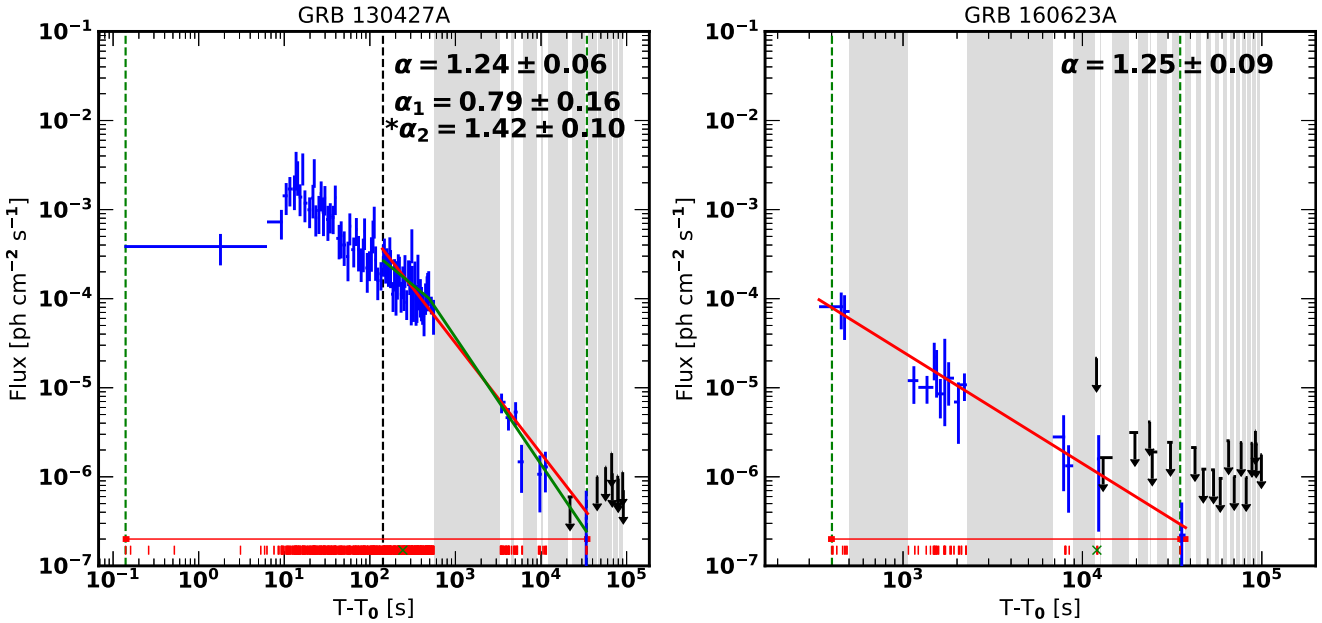

Figure 9. Temporal extended emission for the two longest LAT GRBs, GRB 130427A (left panel) and GRB 160623A (right panel). For the bright GRB 130427A we display the results of the fit for a simple PL model with temporal index α (red line) and with a BPL with indices α_1 and α_2 (green line). For GRB 160623A, only the result of the fit with a simple PL is shown.

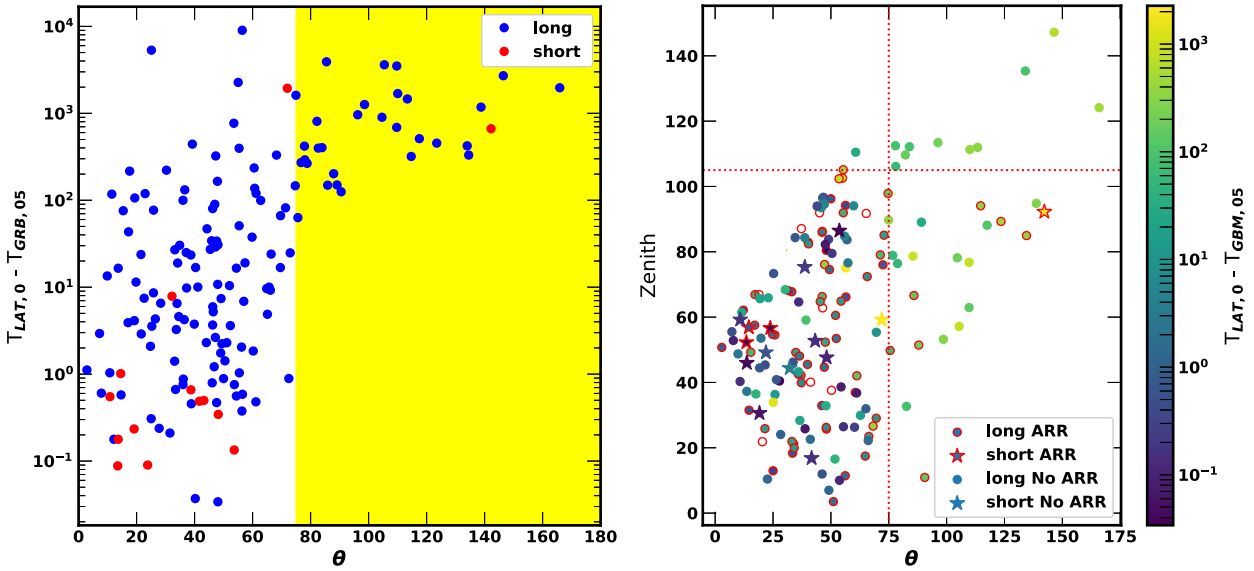

Figure 10. Left panel: difference of the $T_{\rm LAT,0}$ and the $T_{\rm GBM,05}$ with respect to the incident angle of the GRB at the time of the trigger. The yellow region highlights the GRBs that were outside the LAT FOV ($\theta \sim 75^\circ$) at the time of the GBM trigger. Right panel: zenith angle (ζ) vs. incident angle (θ). The symbols are colored as a function of the difference of the $T_{\rm LAT,0}$ and the $T_{\rm GBM,05}$ (left panel, y-axis). Circles mark long GRBs, while stars mark short GRBs. Bursts that triggered an ARR are marked with red contours. The vertical dashed line marks the LAT FOV, while the horizontal line marks the zenith angle cut used in the analysis ($\zeta_{\rm MAX} = 105^\circ$). In general, LAT-detected events at $\zeta > 105^\circ$ and $\theta > 75^\circ$ are seen at very late times or thanks to ARRs.

panel and GRB 160623A in the right panel. In each panel, we also indicate the fit results to the temporal decay, giving the corresponding model parameters in the top right corner. This will be further discussed in Section 4.7.

As already mentioned, a possible bias in the estimation of the onset time in the LAT is related to the initial position of the GRB at the time of the GBM trigger. For a GRB outside the nominal LAT FOV at trigger time, the first significant detection would happen only when the GRB reenters the FOV. We further illustrate this effect in Figure 10. In the left panel the delay of the LAT onset time with respect to the GBM one is plotted as a function of the incident angle of the GRB, while in the right panel we plot the zenith angle as a function of the incident angle. It is evident that all GRBs that were outside the LAT FOV at trigger time have a large delay ($\gtrsim$100 s) with respect to the GBM trigger, which corresponds to the time needed for the GRB to reenter the LAT FOV. On the other hand, we also measure significant delays for GRBs that were in the FOV at the time of the GBM trigger, supporting the intrinsic nature of the delay of the high-energy component.

In the right panel of Figure 10, we highlight GRBs that resulted in an ARR, marking each symbol with a red contour.

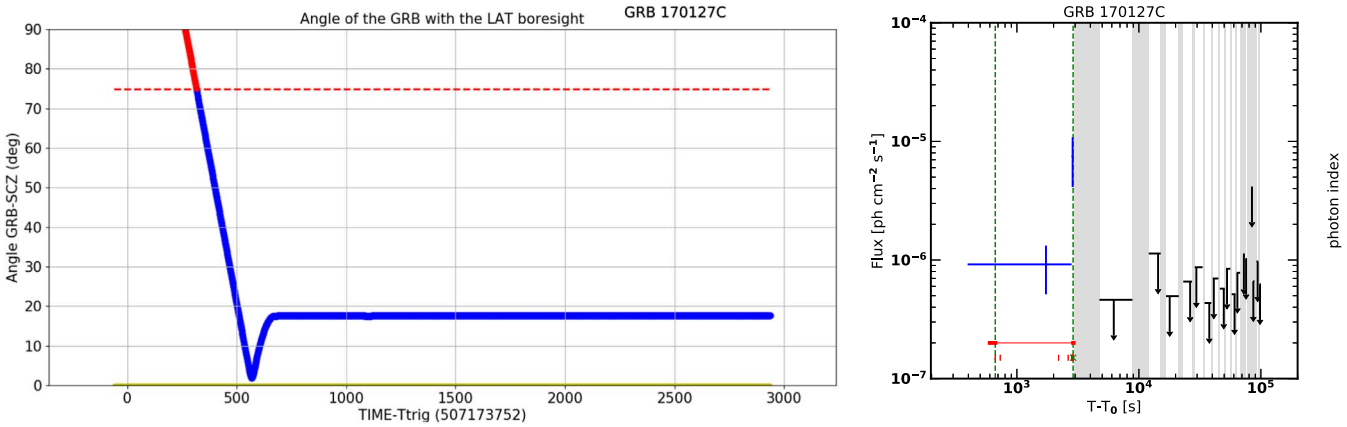

Figure 11. Left panel: off-axis angle for GRB 170127C as a function of time since the GBM trigger. The horizontal red line corresponds to $\theta = 75°$. Right panel: temporal extended emission for GRB 170127C. The blue circle is the photon flux measurement with a significance of TS > 10, while, for lower values of TS, upper bounds are displayed as black arrows. The horizontal red line indicates the estimated duration of the burst, and the thick parts of it correspond to the uncertainty on the $T_{\rm LAT,0}$ and $T_{\rm LAT,100}$ parameters. The red vertical markers indicate the arrival time of each photon with probability >90% to be associated with the GRB, with the green cross being the event with maximum energy.

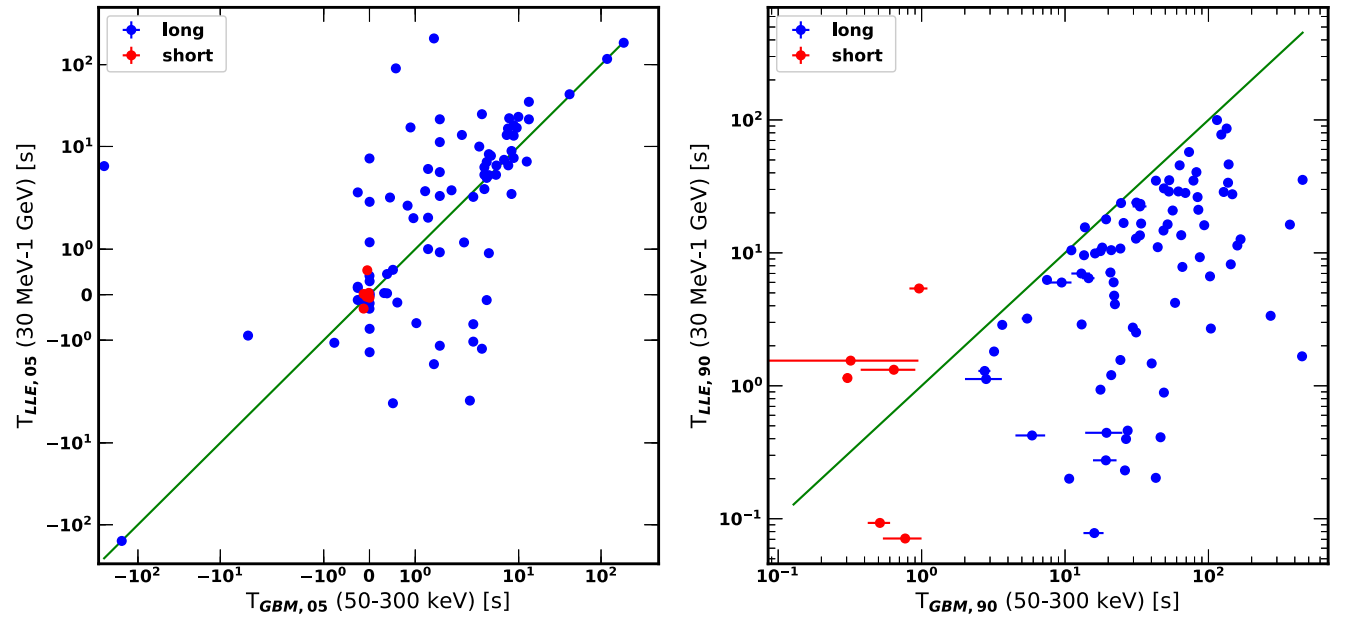

Figure 12. Onset times ($T_{\rm LLE,05}$; left panel) and durations ($T_{\rm LLE,90}$; right panel) calculated using LLE data in the 30 MeV–1 GeV energy range vs. the corresponding quantities ($T_{\rm GBM,05}$ and $T_{\rm GBM,90}$) calculated using GBM data in the 50–300 keV energy range. The solid green line denotes where values are equal. Blue and red circles represent long and short GRBs, respectively.

Most of the bursts for whom an ARR was issued were in the LAT FOV at the time of the trigger, whereas in seven cases the GRBs were outside the LAT FOV and the detection happened only at later times. To better illustrate this effect, we display the case of the short GRB 170127C in Figure 11. This burst was at a zenith angle of $\zeta \sim 94°$ and at an off-axis angle $\theta \sim 142°$ when it triggered the GBM (it is the outlier sGRB seen to the far right in both panels of Figure 10). The trigger resulted in an ARR, and the spacecraft slewed to move the location of the burst close to the center of the FOV (at $\sim$17°). This can be seen in the left panel of Figure 11, where the blue circles show the evolution of θ as a function of time after the trigger. In the right panel, we show the photon flux light curve resulting from the time-dependent analysis. The first detection is at $\sim$400 s, well beyond the end of the GBM signal ($T_{\rm GBM,95} = 0.13$ s).

4.3. LLE Onset and Duration

If we restrict our considerations to the LLE analysis, where the bulk of the emission is in the energy range from 30 MeV to 1 GeV, we see that the left panel of Figure 12 shows how the onset times are relatively similar to the onset times as measured by the GBM. Here, two GRBs are not shown: GRB 120624B and GRB 150513A. Both GRBs triggered *Swift* before they triggered GBM, 257 s (Barthelmy et al. 2012) and 157 s (Kocevski et al. 2015) before the GBM trigger time, respectively. As a result, since all our calculations are referred to GBM trigger times, $T_{\rm LLE,05}$ is negative and omitted from the figure (see Table 3).

In contrast to the emission above 100 MeV, the right panel of Figure 12 indicates that the duration of the signal in LLE is systematically shorter than the duration of the signal in the GBM, as was seen also in the 1FLGC. If we assume that the

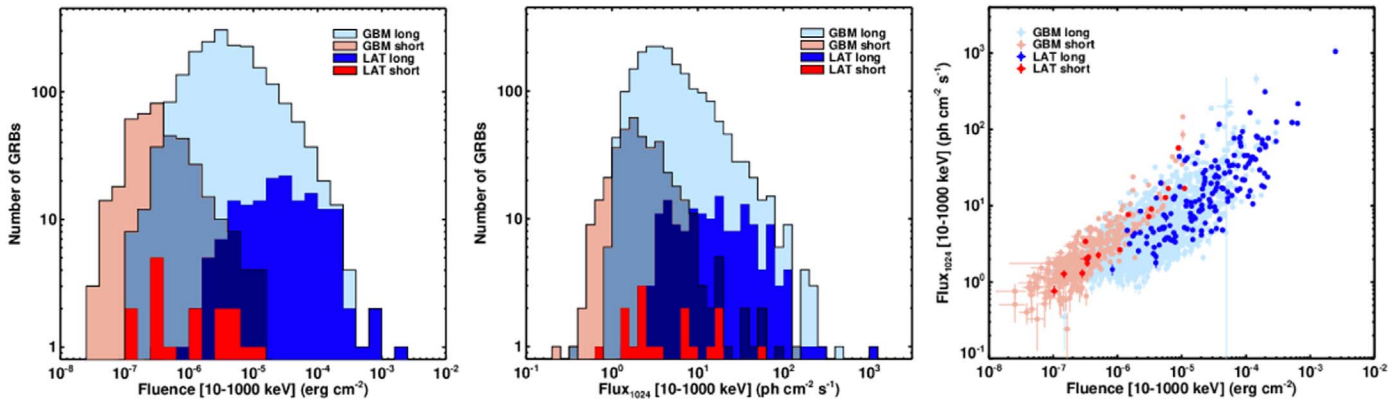

Figure 13. Left panel: distribution of energy fluence calculated in the 10–1000 keV energy range for 178 bursts detected by the LAT compared to the entire sample of 2357 GRBs detected by GBM over the same time period. Middle panel: distribution of peak photon flux in the 10–1000 keV energy range for the same sample of LAT and GBM-detected populations. Right panel: GBM peak photon flux (10–1000 keV), as measured on a 1024 ms timescale, vs. the energy fluence (10–1000 keV) derived using a spectral model fit to a single spectrum over the entire duration of the burst.

LLE emission is dominated by the same emission episodes as in the GBM, we can infer that the pulses that make up the time profile of the prompt emission are systematically shorter in the LLE range than at lower energies. This behavior has previously been reported by Norris et al. (1996) and Norris (2002) using BATSE data, as well as for several LAT-observed GRBs (e.g., Axelsson et al. 2012; Bissaldi et al. 2017; Vianello et al. 2018).

4.4. Comparison to the GBM Population

Since the majority of our triggers come from the GBM, and the GBM has observed nearly all GRBs in our sample, we examine how the LAT-detected bursts are drawn from the general GBM population covering the same 10 yr time period. For this comparison, we extracted the peak photon flux, as measured on a 1024 ms timescale, and energy fluence measured by the GBM in the 10–1000 keV energy range from the FGGC. Here the GBM fluence is derived from the parameters of the best-fit spectral model applied to GBM data over a time interval where the signal-to-noise ratio (S/N) exceeds a predefined value (S/N > 3.5; see Gruber et al. 2014, for more details). This requirement ensures that there are enough counts to perform a spectral fit, but as a result, the time interval does not always coincide with $T_{\rm GBM,90}$. Note that eight GRBs, two triggered by *Swift* and six by the IPN, were not detected by the GBM and are omitted from this comparison and from the following figures.

Figure 13 shows the distribution of the energy fluence (left panel) and of the peak photon flux (middle panel) for 178 bursts detected by the LAT compared to the entire sample of 2357 GRBs detected by GBM over the same time period. Here we have also made a distinction between short and long bursts for both the LAT (16 sGRBs and 162 lGRBs) and GBM (400 sGRBs and 1957 lGRBs) populations, showing a bifurcation in the range of flux and fluence values covered by these two classes of bursts. The right panel shows the peak photon flux plotted against the energy fluence for the LAT bursts compared again to the entire GBM burst catalog. Again, we separate short and long bursts for both the LAT and GBM populations.

These comparisons show that although the majority of the LAT-detected GRBs come from the GBM-detected bursts with the highest peak flux and fluence, they cover a large range. LAT-detected short (long) bursts are present with a fluence $>10^{-7}$ erg cm^{-2} ($>8\times10^{-7}$ erg cm^{-2}) and with a peak flux >0.8 photons cm^{-2} s^{-1} (>1.5 photons cm^{-2} s^{-1}). The LAT-detected long GRBs cover more than two orders of magnitude in both distributions, and the prominence of bright GRBs is even less pronounced in the short GRB sample. The spread is also evident from the right panel of Figure 13, where the cluster of LAT events is only slightly shifted with respect to the GBM one. The burst with the highest fluence (and flux) is GRB 130427A. It is worth noting that Figure 13 does not include any selection on the θ angle.

4.5. Flux, Fluences, and Photon Indices from the Time-integrated Analysis

The results of the likelihood analysis are summarized in Table 4. For each time window, we report the number of detected and predicted LAT events in the ROI, the resulting TS, the spectral index obtained using a PL fit, and the LAT flux and fluence calculated in the 100 MeV–100 GeV energy range. For 34 GRBs with known redshift we also report the total radiated energy ($E_{\rm iso}$).

Figure 14 shows the distributions of fluxes (left panels) and fluences (right panels) as a function of the measured duration of the signal in the "GBM" (top row) and "LAT" (bottom row) time windows. LAT fluxes decrease with increasing burst duration in both time windows, as expected. In the "GBM" time window, the LAT fluence seems to be clustered around a value of 10^{-6} erg cm^{-2} for the majority of lGRBs (regardless of duration), while sGRBs show slightly lower values. Both groups have bursts that are very much brighter than the average. At late times, there is instead a tendency for the fluence to increase with duration. The same conclusion can be drawn from the fluence values in the "LAT" time window, where most of the values are distributed around $\sim5\times10^{-6}$ erg cm^{-2} and there is a less evident spread toward higher values.

Comparing our results to Figure 11 in the 1FLGC, we find that the four "hyperfluent" GRBs are no longer outliers. Instead, they are part of a continuous distribution. The range in both flux and fluence has also increased dramatically as compared to the sample in the 1FLGC.

In Figure 15 we then compare the LAT fluence calculated in the 100 MeV–100 GeV energy range during the "GBM" time window with the GBM fluence calculated between 10 keV and

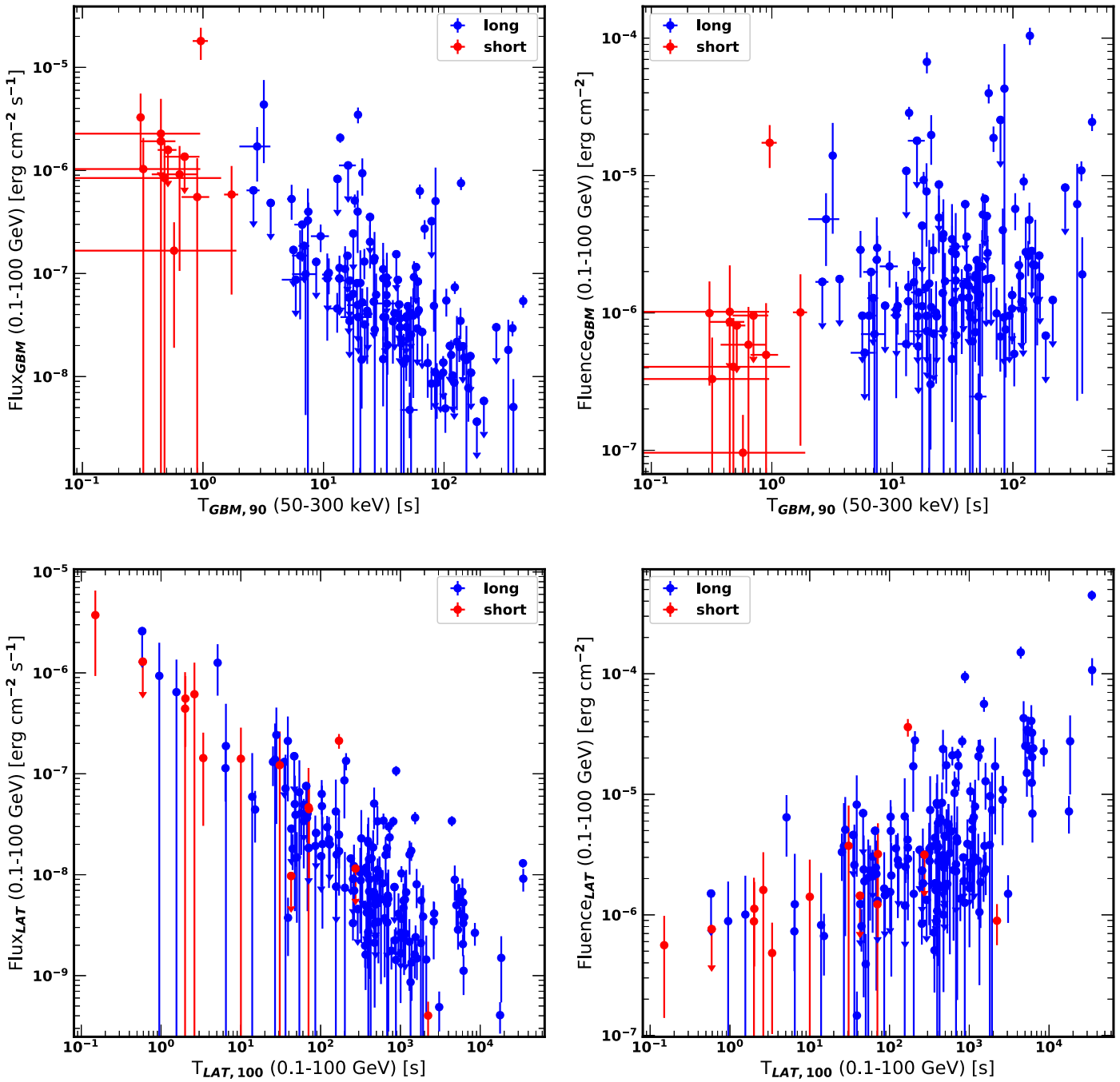

Figure 14. Fluxes (left panels) and fluences (right panels) calculated in the 100 MeV–100 GeV energy range vs. GRB durations. Top panels show fluxes and fluences evaluated in the "GBM" time window vs. durations calculated in the 50–300 keV energy range ($T_{\rm GBM,90}$). Bottom panels show fluxes and fluences evaluated in the "LAT" time window vs. durations calculated in the 100 MeV–100 GeV energy range ($T_{\rm LAT,100}$). Blue and red circles represent long and short GRBs, respectively.

1 MeV (left panel) and with the LAT fluence calculated in the same energy range during the "EXT" time window (right panel). In the left panel, it can be noted that the "GBM" time window is dominated by the low-energy emission, with the 100 MeV–100 GeV energy range contributing only a small fraction of the emission for the majority of long GRBs. Indeed, most events are clustered to the left of the solid and dashed lines, which indicate equality and a factor of 10 less, respectively. For short GRBs this difference seems less pronounced, and several lie close to the solid line of equality. Comparing the "GBM" and "EXT" time windows in the right panel, the points are instead much closer to the line of equality, suggesting that the high-energy emission in the two time windows is comparable. As in Figure 14, the four "hyperfluent" GRBs of the 1FLGC (GRB 080916C, GRB 090510, GRB 090902B, and GRB 090926A) are no longer outliers.

In Figure 16 we also compare the photon index measured by the LAT during the "GBM" time window ($\Gamma_{\rm GBM}$) and the "EXT" time window ($\Gamma_{\rm EXT}$). Both indices are plotted as a function of the GRB duration as calculated in the 50–300 keV energy range (top panels) and of the LAT flux calculated in the "GBM" (bottom left panel) and "EXT" (bottom right panel)

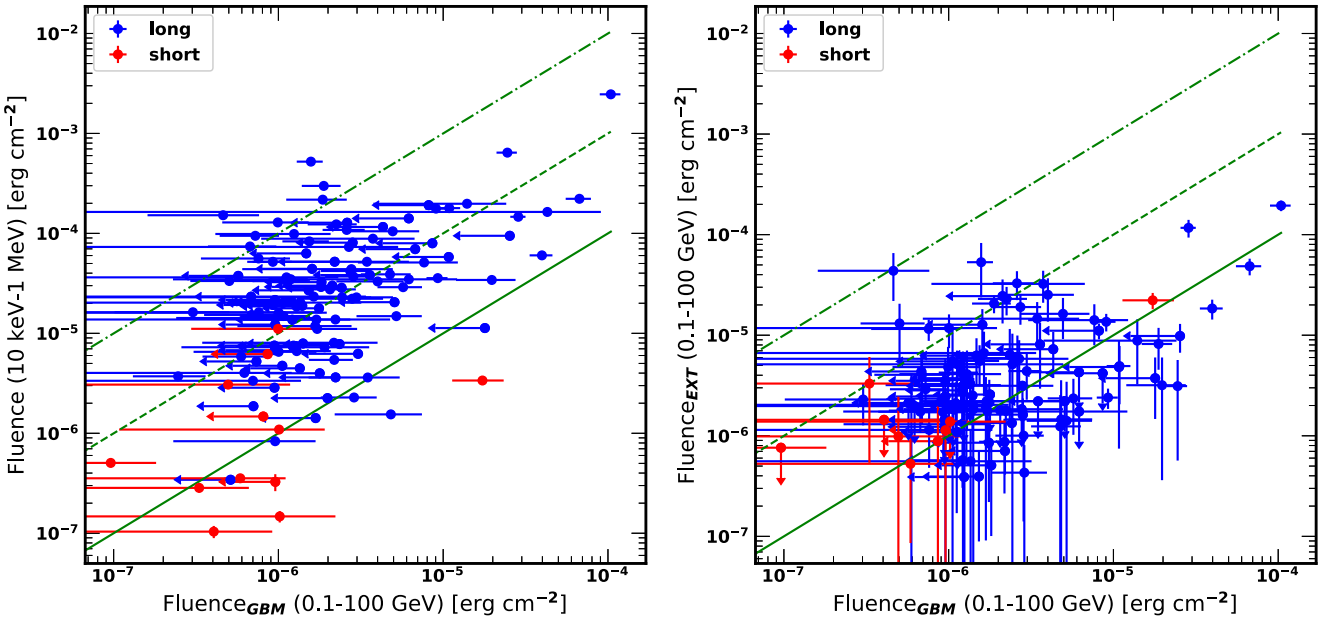

Figure 15. Left panel: fluences calculated in the 10–1000 keV energy range vs. fluences calculated in the 100 MeV–100 GeV energy range. All values are estimated in the "GBM" time window. Right panel: fluences calculated in the 100 MeV–100 GeV energy range evaluated in the "EXT" time window vs. the same quantities evaluated in the "GBM" time window. The solid green lines denote where values are equal. The dashed and dot-dashed green lines are shifted by factors of 10 and 100, respectively.

time windows. The photon index shows no sign of being correlated with either the GBM duration or the flux in either time window, and it is similar for long and short GRBs. The value is indeed similar between the two time windows but is slightly harder in the "EXT" window. In the "GBM" time window, the values of the photon index are more scattered, with a mean value of $\Gamma_{\rm GBM} = -2.49$ and a 10th (90th) percentile of -3.22 (-1.86). In the "EXT" time window, the values are more uniform, with a mean of $\Gamma_{\rm EXT} = -2.03$ and a 10th (90th) percentile of -2.45 (-1.6). For comparison we recall the same values reported in the 1FLGC: -2.08 ± 0.04 in the "GBM" time window and -2.00 ± 0.04 in the "EXT" time window. While the latter is in agreement with the current value, the photon index during the "GBM" time window was much harder than the one we derive in the 2FLGC. Interestingly, it showed a weak inverse correlation with the duration of the burst (see Figure 26 of the 1FLGC). This correlation is now less evident in the larger sample of bursts, but the $\Gamma_{\rm GBM}$ distribution still underlines the agreement with previous findings that the spectra of short-duration GRBs tend to be harder. No clear trend can be seen in the comparison with flux (bottom panels), except a slight tendency for low-flux GRBs to show harder spectra when looking in the "EXT" window.

4.6. Energetics

In order to more closely study the energetics of the bursts in this catalog, and to put the detections in a wider context, we focus on the GRBs with known redshift. We decided to compare our sample to other bursts with measured redshift detected by *Swift* and GBM. As of the end of 2018 July, *Swift*-BAT has detected 1246 GRBs, of which ∼35% have a measured redshift. In the case of the GBM-detected GRBs, only ∼5% have measured redshift. The redshift distributions of 405 bursts detected by *Swift*-BAT (gray histogram), 116 bursts detected by GBM (cyan histogram), and 34 bursts detected by LAT (blue histogram) are shown together in Figure 17. We see no obvious difference between the three distributions.

We next compare the isotropic radiated energy ($E_{\rm iso}$) and the bolometric gamma-ray peak luminosity ($L_{\rm iso}$) of LAT-detected GRBs to the same quantities in the *Swift* and GBM samples. The values for $E_{\rm iso}$ are computed according to Equation (3) in the 1 keV–10 MeV energy range. In the case of GBM-detected GRBs, we adopt the fluence listed in the FGGC as computed from the best-fit spectral model, which is usually calculated on a slightly different time interval with respect to the burst $T_{\rm GBM,90}$, according to the burst brightness.

In order to compute $E_{\rm iso}$ of *Swift*-detected events (with no GBM observation), we used the parameters of the best-fit spectral models obtained in the 15–350 keV energy range reported in the *Swift*-BAT online catalog[75] (see Lien et al. 2016, for more details). These are calculated over a time interval corresponding to a duration that contains 100% of the burst emission. For both the GBM and BAT $E_{\rm iso}$ calculation, we only consider bursts for which the spectral parameters are globally well constrained (see Gruber et al. 2014). Thus, we find 116 (405) GBM (BAT) GRBs that satisfy these criteria, out of which 108 (376) are lGRBs and 8 (29) are sGRBs. The LAT sample comprises 32 lGRBs (2 of the 34 were not detected by the GBM, as previously discussed) and only one sGRB (090510).

We also calculate the isotropic luminosity $L_{\rm iso}$, which takes into account the GRB prompt emission spectrum and is defined in a 1 s time interval centered around the time of the peak flux. It can be expressed as

$$L_{\rm iso} = 4\pi\, d_L^2\, P(E_1, E_2, z), \tag{7}$$

[75] https://swift.gsfc.nasa.gov/results/batgrbcat/

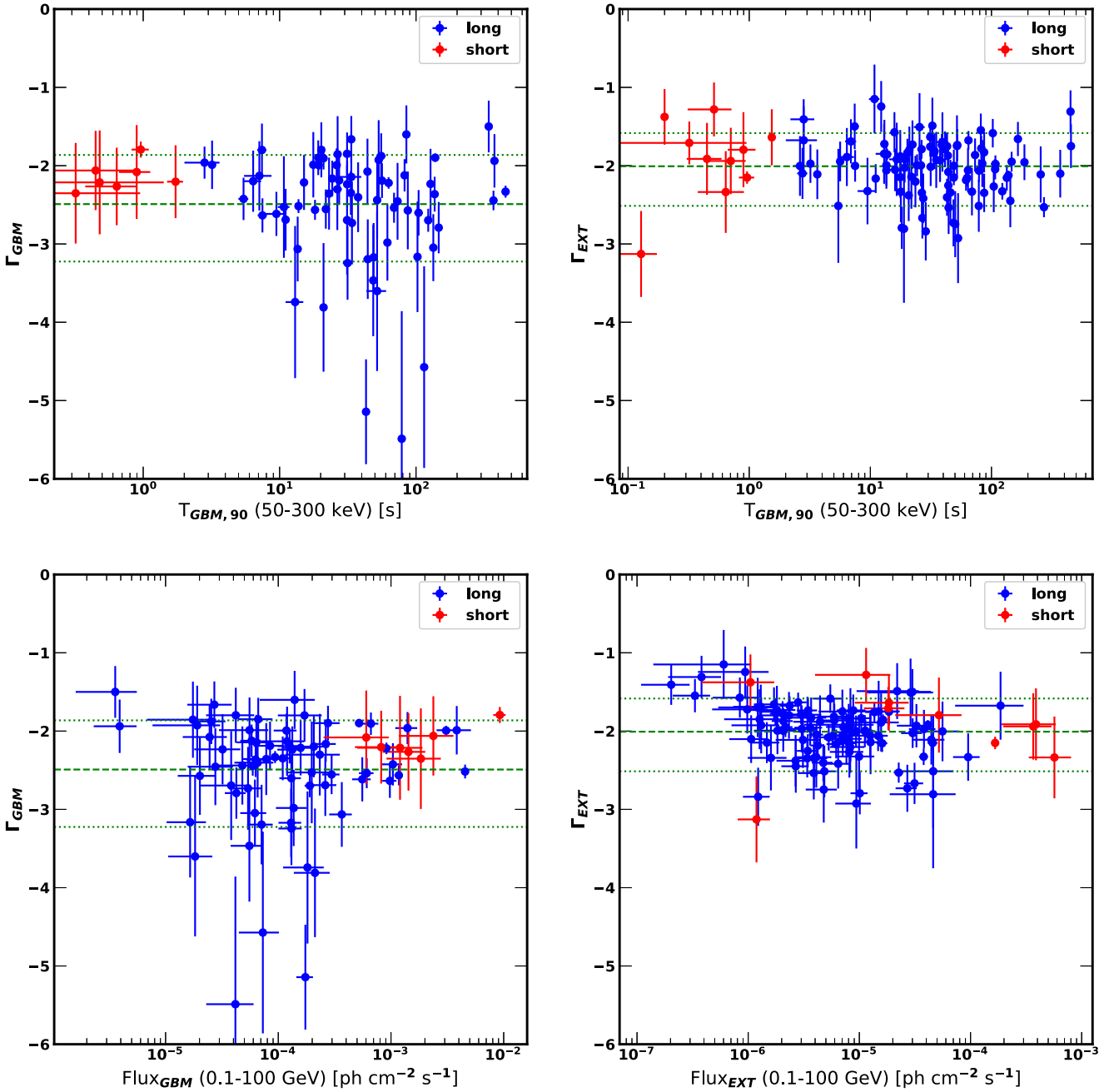

Figure 16. Photon indices $\Gamma_{\rm GBM}$ (left panels) and $\Gamma_{\rm EXT}$ (right panels) calculated in the 100 MeV–100 GeV energy range vs. duration calculated in the 50–300 keV energy range (top panels) and LAT 100 MeV–100 GeV fluxes (bottom panels). These are calculated in the "GBM" (bottom left) and "EXT" (bottom right) time windows, respectively. The green dashed lines denote the mean values and the dotted lines the 10th and 90th percentiles of each distribution. Blue and red circles represent long and short GRBs, respectively.

where $P(E_1, E_2, z)$ represents the bolometric peak flux, defined as

$$P(E_1, E_2, z) = \int_{E_1/(1+z)}^{E_2/(1+z)} E\, N(E) dE. \quad (8)$$

As with $E_{\rm iso}$, $L_{\rm iso}$ is computed in the 1 keV–10 MeV energy range, for GBM-detected GRBs, using the 1 s peak flux of the best-fit model as reported in the FGGC. We again consider only GRBs whose time-integrated spectra are well defined, as reported in the GBM and *Swift*-BAT GRB catalogs. This leaves us with 394 BAT GRBs and with the same number (116) of GBM GRBs. The slightly lower number of BAT GRBs is expected, as the time interval (and thereby the number of photon counts) is smaller.

Figure 18 shows the distribution of $E_{\rm iso}$ (left panel) and $L_{\rm iso}$ (right panel) as a function of redshift. *Swift*-BAT and GBM bursts are indicated by gray and black points, respectively, with long (short) bursts marked with filled (open) symbols. LAT long and short bursts are marked with the standard blue and red circles, respectively, used in this paper. LAT-detected GRBs populate the top portion of both distributions, as was previously seen in the 1FLGC. At that time, this figure only contained nine LAT-detected GRBs with redshift. It is

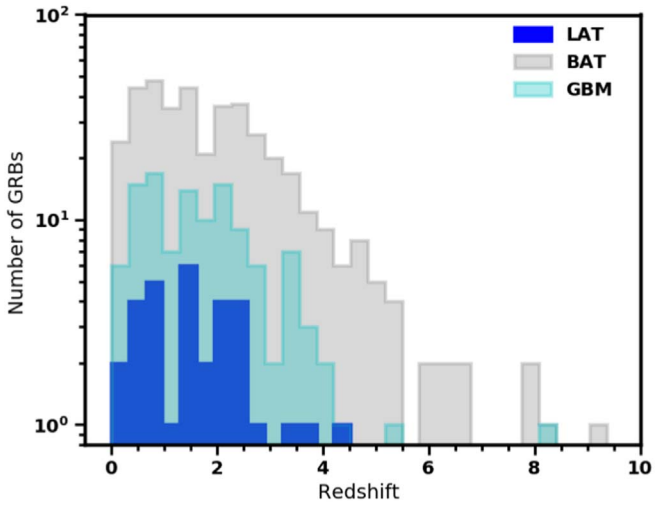

Figure 17. Redshift distribution of 34 GRBs detected by LAT (blue histogram), 405 GRBs detected by *Swift*-BAT (gray histogram), and 116 GRBs detected by GBM (cyan histogram).

worth noting that quite a few bursts have a moderate 1 keV–10 MeV $E_{\rm iso}$ ($\lesssim 10^{-53}$ erg) yet have nevertheless been detected by the LAT.

4.7. Time-resolved Light Curves

We now turn to the temporal decay of the high-energy extended emission. Using the analysis described in Section 3.6.2, we were able to determine the evolution of the flux as a function of time for 115 long and 11 short GRBs in our sample. This is shown in the two panels of Figure 19, displaying the temporal decay of long (left panel) and short (right panel) bursts separately. Each event is marked with a different color. The light curves of both sGRBs and lGRBs show a fairly large spread in the observer frame.

In order to determine the corresponding temporal decay index, we perform a fit of all the light curves maximizing the χ^2, with two different spectral models, namely, (1) a simple PL,

$$F(t) = F_0 \left(\frac{t}{T_0}\right)^{-\alpha}, \tag{9}$$

where α is the temporal decay index, T_0 is the GRB trigger time, and F_0 is the normalization flux; and (2) a BPL,

$$F(t) \propto t^{-p} \begin{cases} p = \alpha_1 & \text{for } t < T_b \\ p = \alpha_2 & \text{for } t \geqslant T_b, \end{cases} \tag{10}$$

with index α_1 for times before the break time T_b and index α_2 afterward. If there are at least three flux points (with TS > 10) in the light curve after the $T_{\rm GBM,95}$, we fit a PL, and if there are at least four flux points, we also try a BPL.

The results of the fits are presented in Table 5. By fitting the flux temporal decay with a BPL, we find a significant improvement in 12 cases. We show three examples in Figure 20 (GRB 090510, GRB 150627A, and GRB 180720B; a fourth, GRB 130427A, has already been shown in the left panel of Figure 9). The BPL fit is indicated with a solid green line, and the corresponding fit values are given in the upper right corner of each panel. The PL fit is shown with a red solid line for comparison. In all but two cases the light curves manifest a steep-to-shallow decay, while for GRB 171120A and GRB 180720B (right panel in Figure 20) the decay steepens after the break.

The distribution of late-time temporal decay indices (α or α_2) is displayed in Figure 21, together with a Gaussian fit (black dashed line) to the distribution. The distribution comprises 88 GRBs, including 86 long and 2 short bursts. Among the long (short) GRBs, 77 (1) are best fit with the PL model, while 11 (1) prefer a BPL model. This is a large increase compared to the 1FLGC, where only nine GRBs had enough data to allow the decay index to be determined, ranging from 0.8 (for GRB 090902B) to 1.8 (for GRB 080916C) and with a mean value of $\sim$1.1. We now find a mean value of 0.99 ± 0.04 with a standard deviation of 0.80 ± 0.07, still in agreement with the results presented in the 1FLGC.

These results and their interpretation will be discussed in more detail in Sections 5.6 and 6.3, but it is worth noting that there are several cases in which a BPL would likely be required if the data in the "GBM" time window had been included. Furthermore, several GRBs show features in the light curve that deviate from both a PL and BPL. Four light curves exemplifying both these cases are displayed in Figure 22.

In the figure, GRB 131108A (top left) exemplifies how some bursts display strong variability in the LAT > 100 MeV light curve during the GBM emission. GRB 140206B (top right) instead shows the possible presence of a late-time high-energy pulse. GRB 160625B (bottom left) shows a strong pulse with a very sharp decay. GRB 160816A (bottom right panel) would clearly require a break to accommodate the data in the "GBM" time window. However, in the "EXT" time window used for the fits, a PL model is statistically preferred. These peculiar features are all observed for the first time in the 2FLGC. Some light curves, like GRB 140206B (top right panel in Figure 22), show a sharp step between the end of the "GBM" and the beginning of the "EXT" time window (marked by the vertical black dashed line). In these cases, a fit of the complete data set would again favor a BPL model rather than the PL one currently used in the "EXT" time window. In a few even more extreme cases, the light curve could not be fit at all in the "EXT" time window, since there is only a single point in the light curve after the "GBM" time window.

In Figure 23, we show the 100 MeV–100 GeV luminosity evolution for the 34 GRBs in our sample with measured redshift. Among those, there is only one short burst, namely, GRB 090510. The three panels of the figure show first the light curves in the observer frame (left), the evolution as a function of time in the source frame (middle), and finally the luminosity divided by isotropic energy ($E_{\rm iso}$; right), calculated in the 1 keV–10 MeV energy range. Each correction brings the light curves closer together, and in the right panel there is a remarkable alignment of all the GRBs. This analysis was done following the one presented by Nava et al. (2014), where a similar result was found. It is worth noting that in the right panel of Figure 23 one of the GRBs, GRB 160623A, does not align with the others, indicating a possible outlier. This burst was occulted by Earth for a large part of its duration, and the GBM trigger occurred $\sim$50 s after the start of the GRB based on the Konus-*Wind* light curve. This likely leads us to underestimate the total energy release $E_{\rm iso}$ of the burst and thus to overestimate the normalization of the light curve. In the right panel we also include a linear fit to all 34 GRBs, indicated by the solid line. The decay index is 1.25 ± 0.03. For

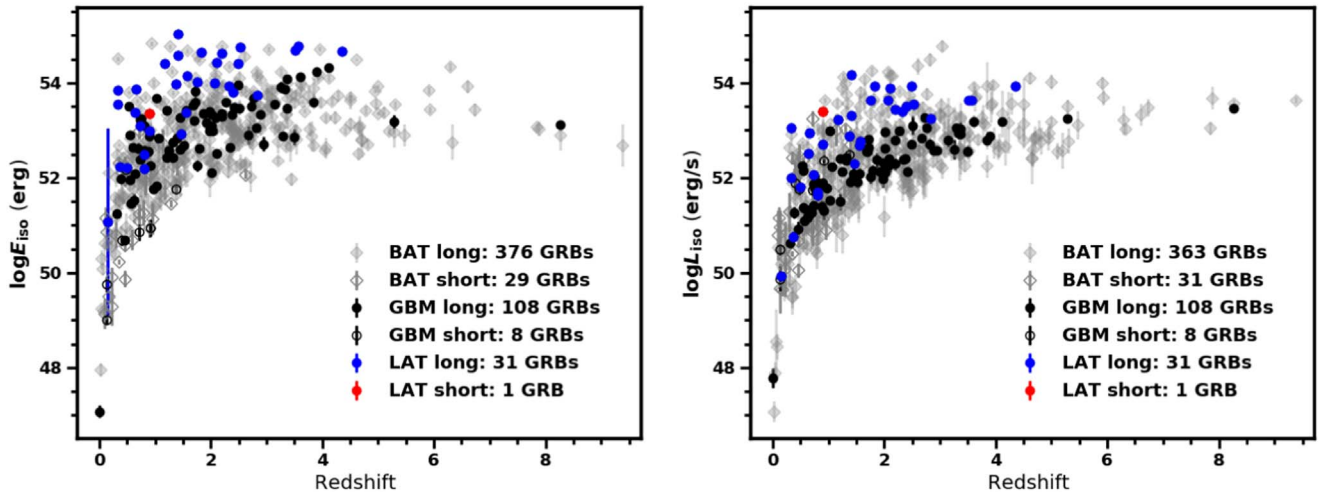

Figure 18. Left panel: isotropic radiated energy vs. redshift. Right panel: isotropic luminosity vs. redshift. Blue/red circles indicate the LAT long/short GRBs, and black and gray circles indicate GBM/*Swift*-BAT GRBs, with short bursts always marked by open symbols.

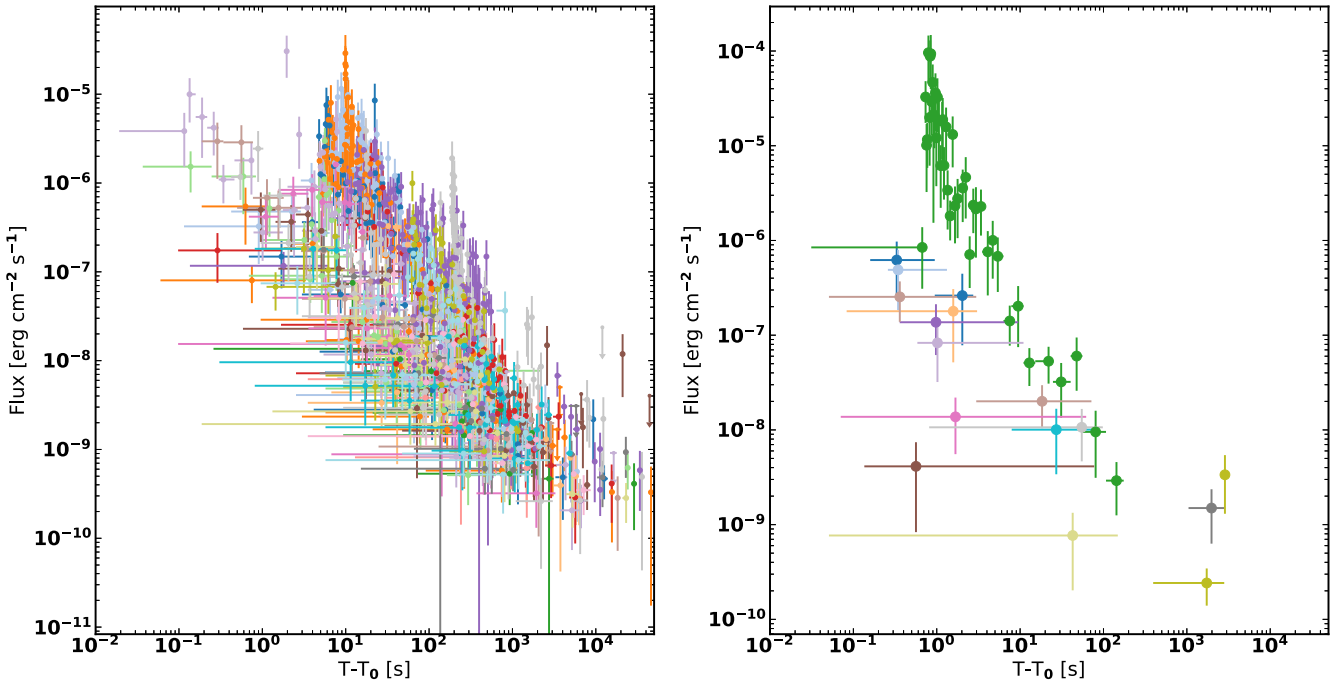

Figure 19. Flux calculated in the 100 MeV–100 GeV energy range vs. elapsed time after trigger for 115 long (left panel) and 11 short (right panel) bursts. Each color represents a separate GRB.

comparison, we also show a dashed line with decay index 10/7 (see further Section 5.6).

4.8. High-energy Events

The highest-energy GRB photon ever recorded by *Fermi* thus far is a 94.1 GeV event connected with GRB 130427A (Ackermann et al. 2014). While displaying photon energies of a few hundred MeV is a common feature among the LAT-detected GRBs, higher energies are relatively rare. Table 6 summarizes the highest-energy photon characteristics for each burst in our sample. It lists the total number of photons detected with probability >90% of belonging to the burst, as well as the energy, arrival time, and probability of the highest-energy photon detected in the "GBM" time window. We also list the same quantities calculated in the time-resolved analysis.

Figure 24 shows the fraction of GRBs detected above selected energy thresholds (250 MeV, 500 MeV, 1 GeV, 5 GeV, 10 GeV, 50 GeV). A sharp drop from ∼70% to ∼30% is seen at 5 GeV. There are three GRBs with emission above 50 GeV (2%), namely, GRB 130427A (95 GeV), GRB 140928A (52 GeV), and GRB 160509A (52 GeV).

Our sample of 34 GRBs with measured redshift also allows us to study the source-frame-corrected energies. This is shown as the dashed line in Figure 24. This distribution shows a more gradual decrease with energy: almost 80% of the included GRBs have a maximum source-frame photon energy above 5 GeV, and ∼12% (four GRBs) above 100 GeV. The highest

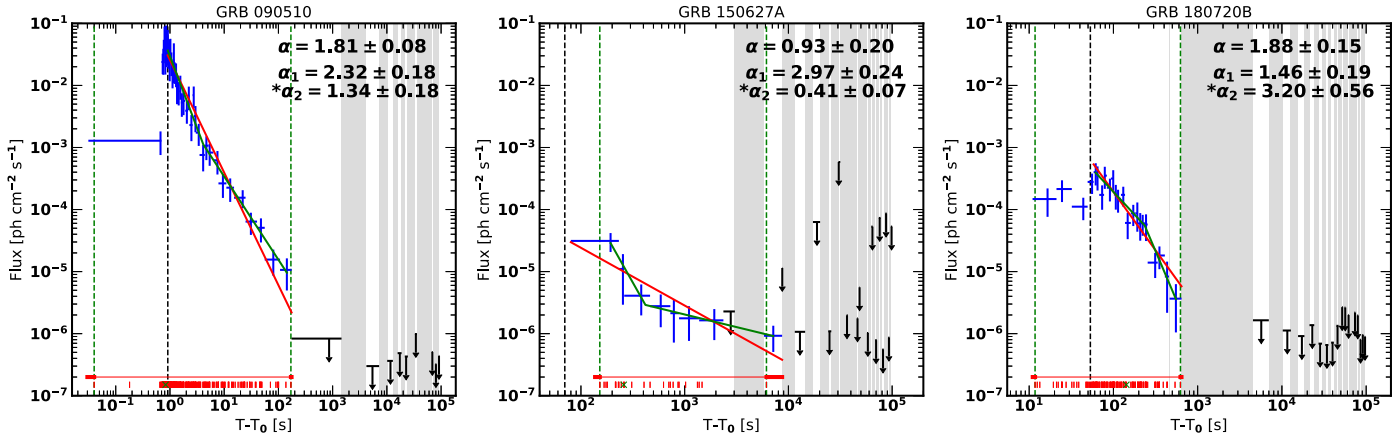

Figure 20. Temporally extended emission for three GRBs that are best fit by a BPL model (a fourth one, GRB 130427A, is shown in the left panel of Figure 9). GRB names are shown in the title in each panel. The red vertical markers indicate the arrival times of the events with probability >0.9 to be associated with the GRB, with the green cross being the event with maximum energy. The green vertical dashed lines indicate the first and the last event. The vertical dashed black line marks the $T_{\rm GBM,95}$. The PL and BPL fits are indicated with solid red and green lines, respectively. Fit parameters are given in the top right corner of each panel. The asterisk highlights the value selected as the temporal decay index in the analysis (which, in these cases, always corresponds to α_2 of the BPL model).

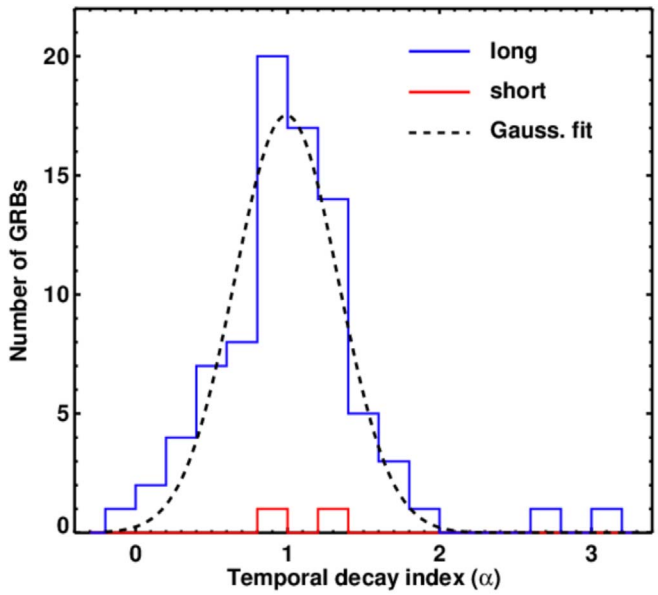

Figure 21. Distribution of the temporal decay indices for 86 long (blue histogram) and 2 short (red histogram) bursts, calculated in the "ETX" time window. A Gaussian fit of the lGRB indices (mean 0.99 ± 0.04; standard deviation 0.80 ± 0.07) is superimposed on the distributions (dashed black line).

source-frame energy is a 147 GeV photon from GRB 080916C, at $z = 4.35$ (Atwood et al. 2013b). The figure also includes a linear fit to the bin centers of the source-frame distribution. The fit is remarkably good, showing that the fraction of GRBs decreases as $A \times \log(E/1\ \mathrm{MeV}) + B$, where $A = -49 \pm 4$ and $B = 266 \pm 21$.

Figure 25 shows the energy of the highest-energy photon in each GRB as a function of arrival time (left panel). In the right panel of the figure, the arrival time is shown as a fraction of $T_{\rm GBM,90}$, calculated in the 50–300 keV range. No clear pattern can be distinguished, with long and short bursts overlapping in the right panel. The one clear outlier in the right panel is the short GRB 170127C, where the highest-energy photon (500 MeV) was detected almost 3 ks after the trigger. This GRB was outside the LAT FOV at T_0, and the data therefore only cover the time from around 300 s after the trigger (see also Section 4.2 and Figures 10 and 11).

In order to check for more high-energy photons to be detected beyond the standard energy range (>100 GeV), we performed an additional analysis up to 300 GeV. No LAT detection was made above 100 GeV. Table 7 presents the 29 GRBs in the sample detected above >10 GeV. All high-energy photons with a probability >90% and with an observed energy >10 GeV are reported for each burst. As in Table 6, we specify the photon energy (listed in decreasing order), its arrival time, the GRB redshift, and the source-frame-corrected energy ($E_{\rm sf}$). Values of $E_{\rm sf} > 100$ GeV are marked in bold. The only short burst listed in this table is GRB 090510: in this case, a ∼30 GeV photon was detected 830 ms after the GBM trigger time. GRB 130427A holds the record with 17 photons detected above 10 GeV, with the highest event ever detected from a GRB (the 94.1 GeV photon) observed 243 s post-trigger. The second burst with the most HE photons is GRB 090902B, with seven photons detected above 10 GeV. There are two bursts where a high-energy photon is detected at very late times (>10 ks): GRB 130427A (∼34 ks) and GRB 160623A (∼12 ks).

5. Discussion

We will now discuss our results and compare them to previous results, in particular what was seen in the 1FLGC. The discussion generally follows the outline of Section 4, starting with the LAT sample as a whole, then continuing with a comparison to the GBM sample. Finally, we will consider the energetics, temporal decay, and possibilities for detections at very high energy (VHE). The aim of this section is to put our results in a wider context; broader implications in the framework of theoretical models will be discussed in Section 6.

5.1. Detectability of LAT Bursts and LAT Detection Rate

Before launch it was estimated that the LAT would detect 10–12 GRBs per year above 100 MeV (Band et al. 2009). The results from the first GRB catalog showed 28 GRBs detected in the first 3 yr of the mission, slightly below expectations. The current work instead shows that the LAT has exceeded

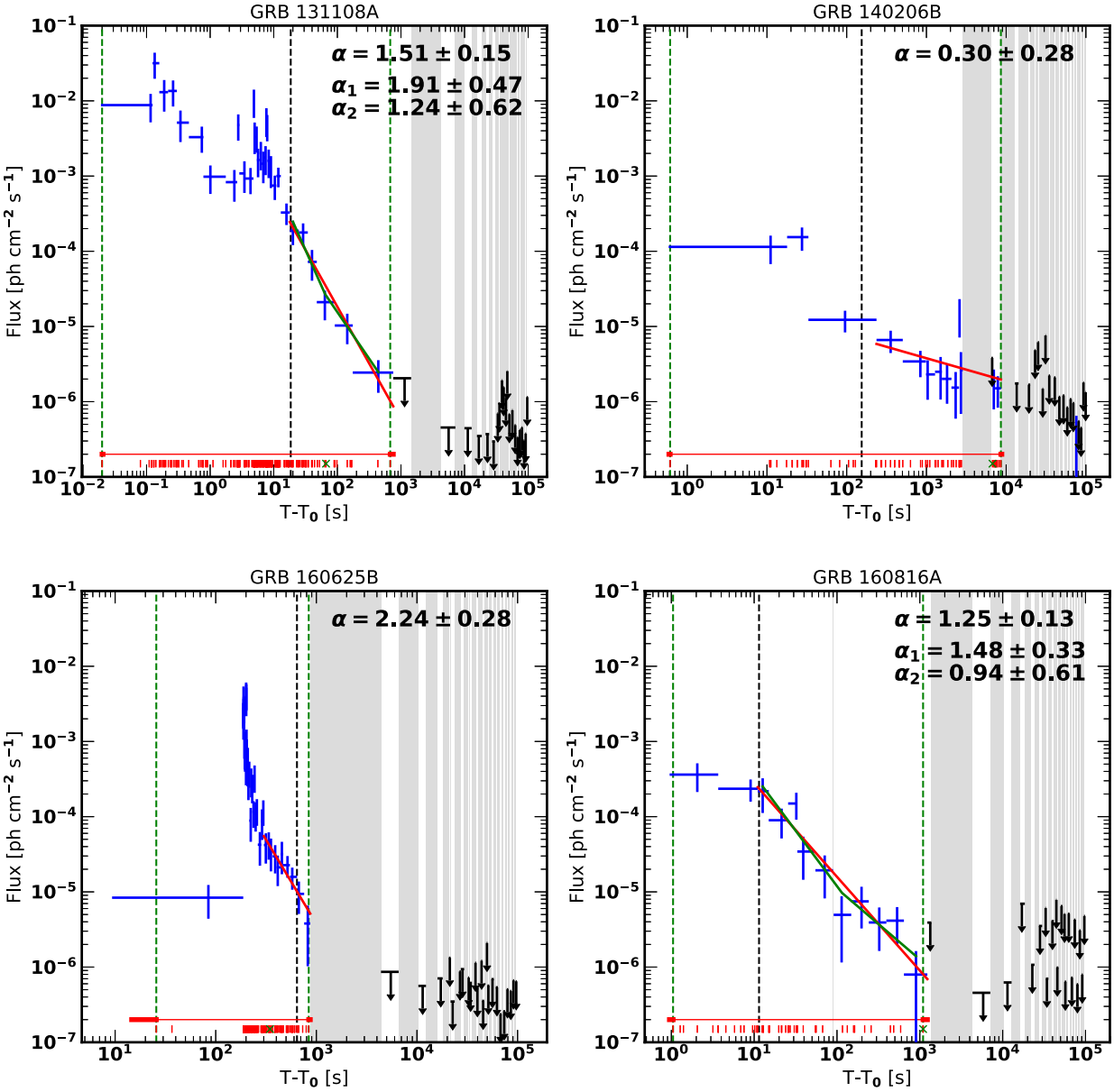

Figure 22. Temporal extended emission for four GRBs showing a peculiar behavior (the name of each GRB is shown in the title of each panel). Markers are the same as in Figure 20.

expectations, with 169 GRBs detected above 100 MeV in 10 yr. This is in large part due to the continuous improvements in event analysis and detection algorithms.

It is interesting also to look specifically at the highest energies of the LAT-detected GRBs. As can be seen from Figure 24, only a small fraction of GRBs are seen in the upper energy range of the LAT. For example, 20% of the GRBs have detected emission above 10 GeV, corresponding to ∼3 GRBs per year. We will further discuss the occurrence of these highest-energy events in Section 5.5.2.

Another interesting aspect to discuss is that while the highest-energy photon most often arrives after the $T_{\rm GBM,90}$ (right panel of Figure 25), there is also a large fraction where it arrives during this interval. Interestingly, this fraction seems to vary slightly with energy: below 1 GeV more than half of the events arrive during $T_{\rm GBM,90}$, whereas 70% of events arrive later at energies above 10 GeV. We also note that there is little difference between the short and long GRB populations regarding normalized arrival time, although the maximum energy of sGRBs appears on average a bit lower. This could link the highest-energy photons to a process common in the two scenarios, and independent from the progenitor, such as external shocks in the circumburst medium. This will be further discussed in Section 6.

As of writing, the observing pattern adopted after the solar array malfunction (see Section 2.1) could potentially lead to a loss in GRB detections, as events occurring in the unobserved hemisphere of the sky may not be monitored until long after the event. However, studying the detections reported in this catalog, no such event was detected even during the previous observing strategy. The exception to this are the ARRs, as they could bring bright events into the FOV. It is thus likely that the detection rate will be slightly impacted while ARRs remain disabled. Even if the LAT detects late-time emission, without ARRs there is the risk of losing high-energy prompt emission.

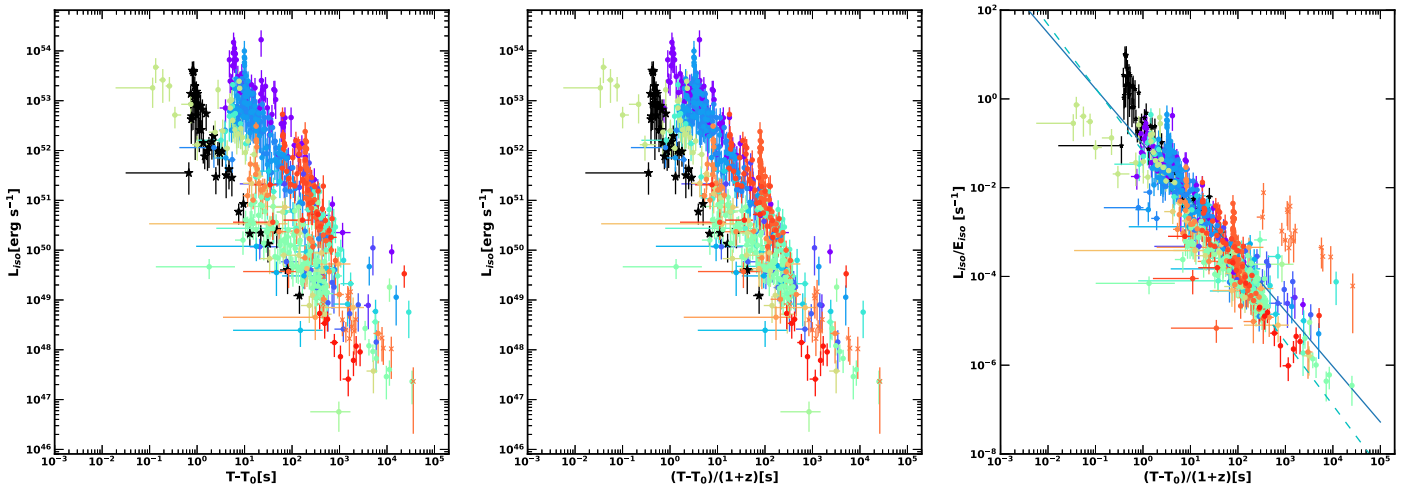

Figure 23. Isotropic luminosity $L_{\rm iso}$ calculated in the 100 MeV–100 GeV rest-frame energy range for the 34 GRBs in our sample with measured redshift. The left panel shows $L_{\rm iso}$ vs. the time elapsed since the trigger. GRB 090510 is the only short GRB with known redshift, and it is marked with black stars. In the middle panel $L_{\rm iso}$ is plotted against the time elapsed since the trigger in the rest frame. In the right panel, we show $L_{\rm iso}$ divided by the isotropic energy (calculated in the 1 keV–10 MeV rest-frame energy range) vs. the time elapsed since the trigger in the rest frame. We mark GRB 160623A, which represents an outlier of the distribution (see text for explanation), with orange crosses. The solid line shows a linear fit, giving a decay index of 1.25 ± 0.03. For comparison, we also show a dashed line with decay index $10/7$.

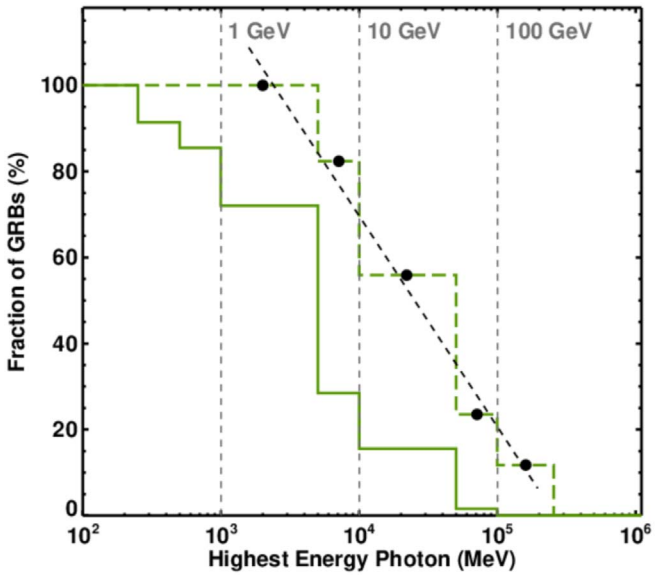

Figure 24. Fraction of GRBs with the highest-energy photon detected above selected threshold energies (250 MeV, 500 MeV, 1 GeV, 5 GeV, 10 GeV, 50 GeV; green solid line). The distribution of the source-frame-corrected energies for the redshift sample is indicated with the dashed green line. The dashed black line denotes a linear fit to the values corresponding to the center of each bin.

5.2. Onset and Duration of the High-energy Emission

As in the 1FLGC, we can firmly establish the general trend that high-energy emission from GRBs tends to have delayed onset and longer duration as compared to emission at lower energies. However, Figure 7(c) also shows that when high-energy emission is detected, it starts during the prompt phase in >60% of the cases. The majority of the other GRBs were outside the LAT FOV at trigger time, meaning that the fraction is likely even higher. This is an interesting result that provides valuable input to models of the emission mechanisms and will be discussed further in Section 6.

Figure 7 shows how varied the difference between $T_{\rm GBM,05}$ (calculated in the 50–300 keV range) and $T_{\rm LAT,0}$ (100 MeV–10 GeV) can be. In some cases, the LAT emission is completely contemporaneous with the GBM. In other cases, the LAT emission starts hundreds or even thousands of seconds later. Considering only bursts that were in the LAT FOV at the time of trigger, there are a number of cases where the high-energy emission came much later than the one at lower energies. For example, GRB 160503A shown in the right panel of Figure 6 was at $\theta = 25.1^\circ$ at $T_{\rm LAT,0}$, and it remained in the FOV for over 2 ks without any high-energy emission being seen. The first detection instead came much later, at 5 ks. These extreme delays are much longer than the ones seen in the 1FLGC and represent a new result in the 2FLGC.

In addition to greater delays, we now report much longer durations. In the 1FLGC, the longest duration reported was >800 s for GRB 090902B. In the 2FLGC, many GRBs have durations of order 10^3 s, with the longest duration being 35 ks (GRB 160623A). In general, the durations have increased also for most bursts contained in the 1FLGC, likely due to better sensitivity as a result of Pass 8 (we note, however, that the duration estimates were made using a different technique as described in Section 3.6.2, so the numbers are not directly comparable).

5.3. Comparison with GBM Flux and Fluence Distribution

As already presented in Section 4, the LAT-detected GRBs tend to sample the upper range of the GBM flux and fluence distribution (Figure 13). At the high end of the GBM fluence distribution, the LAT detects a high fraction of the GRBs; above $\sim 10^{-4}$ erg cm^{-2} the two distributions practically overlap (left panel). The few additional bursts seen by the GBM could be explained by some GRBs being outside the LAT FOV or at high zenith angles. The effect of the θ angle is further investigated in Ajello et al. (2018), who show that this is the main factor determining LAT detectability. The bias toward high GBM flux and fluence for LAT-detected bursts is therefore not related to a difference in sensitivity between the instruments.

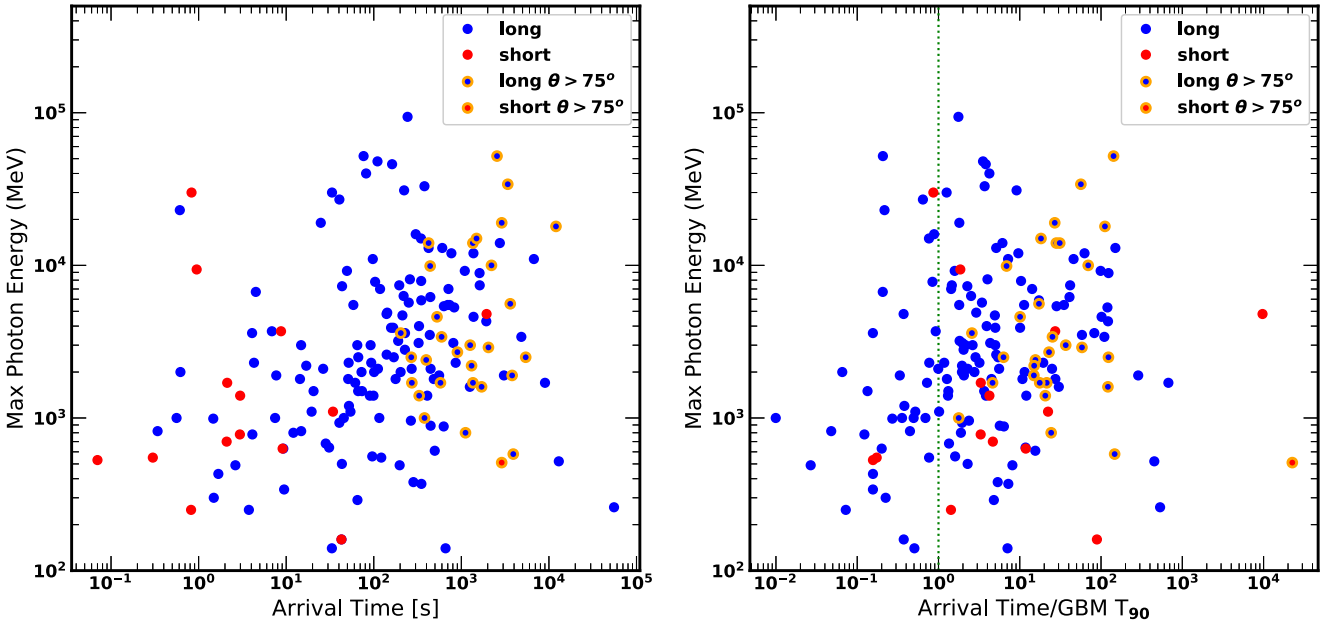

Figure 25. Energy vs. arrival time for the highest-energy photon of each GRB. In the right panel, the arrival time is normalized to the duration (T_{90}) calculated in the 50–300 keV energy range (indicated by the dashed vertical line). Blue and red circles represent long and short GRBs, respectively.

Looking at the high end of the flux distribution (middle panel of Figure 13), the fraction of GRBs not seen by the LAT is higher. This shows that the flux might not be such a good indicator for high-energy emission. While the fluence is a measure of the total energy output, the flux simply shows the "strength" of the peak. The light curves also show clear differences, and peaks at low energies are not necessarily mirrored at high energies. An example of this is GRB 180728A, where the GBM peak flux was about 230 photons $\mathrm{cm}^{-2}\,\mathrm{s}^{-1}$ (Veres et al. 2018), but no detection was made at high energy even though the burst was inside the LAT FOV ($\theta \sim 35^{\circ}$). This is likely due to the low value of E_{peak}, 80 keV; indeed, the flux was dominated by energies below 50 keV.

However, the LAT has also detected GRBs that have relatively low fluence in the GBM. These outliers are predominantly short GRBs, where the low fluence is naturally explained by the short duration. The fluence distribution of sGRBs in the GBM is also shifted to lower values overall. Also for sGRBs there is a tendency for the LAT to sample the higher fluence end of the GBM population, but this is much less marked than for the lGRBs.

The result that the LAT detections are biased toward the brighter GRBs was clear already in the 1FLGC. However, with the larger sample, the picture presented here becomes more nuanced. The sGRBs show that high-energy emission can be produced even at lower fluence, raising the question of why not more lGRBs are detected. There may be differences in the emission mechanisms or environments between the classes that explain why low-fluence sGRBs are more likely to be detected in high-energy emission than lGRBs of similar fluence. For instance, lGRBs are expected to have a denser circumburst medium, as they are coupled to massive stars that have strong stellar winds.

The possibility of GeV emission from sGRBs is particularly interesting in the light of GW170817 and the associated sGRB 170817A (Abbott et al. 2017a, 2017b; Goldstein et al. 2017). This event was outside the LAT FOV and had a fairly low fluence of 2.8×10^{-7} erg cm^{-2}. However, Figure 13 shows that the LAT has detected GRBs with a similar fluence. This is very promising in view of the upcoming observation period scheduled to start in spring 2019, showing a strong potential for LAT detections of similar events (see also Ajello et al. 2018).

5.4. Origin of Emission below 100 MeV

In our sample almost twice as many GRBs are detected above 100 MeV (169) as in the 30–100 MeV LLE range (91). Several studies have found evidence for a separate spectral component behind the emission above 100 MeV, and high-energy cutoffs between the LLE and LAT energy ranges have also been seen (e.g., Vianello et al. 2018). The behavior of the emission below 100 MeV further shows more similar temporal behavior to the GBM range than do the data above 100 MeV (see Figures 7 and 12). The LLE-only GRBs in our sample would then be the result of the low-energy emission being strong enough (and/or E_{peak} at high enough energy) to extend into the LLE range. As the burst evolves, E_{peak} moves to lower energies, and the emission in the LLE range will therefore appear to fade before that at lower energies. This explains the fact that the duration at 30–100 MeV is almost always shorter than the one measured by the GBM. This picture also explains the fact that the LLE emission appears to start earlier than the GBM emission in a few cases (left panel in Figure 12). As the duration is shorter in the LLE range, this will naturally make the value of $T_{\mathrm{LLE},05}$ shorter as well. Again, it is just a sign that the emission in the GBM range lasts much longer than the one in the LLE range.

For GRBs detected in both LAT and LLE energy ranges, the duration is generally shorter in the 30–100 MeV band. While direct comparison of the $T_{\mathrm{LLE},90}$ and $T_{\mathrm{LAT},100}$ should be done with caution, the large differences in duration here clearly point to an intrinsic origin rather than observational bias. For example, in the LLE range the effective area is up to a factor of 2–3 lower than that above 1 GeV; however, the $T_{\mathrm{LAT},100}$ can be more than an order of magnitude longer than the $T_{\mathrm{LLE},90}$.

Although there is much to suggest that the LAT emission is often the result of a separate component, we caution that there are also cases where the GRB spectrum is seen in the full range from keV to GeV and well fit by a single component extending also to energies above 100 MeV (e.g., Abdo et al. 2009c; Axelsson et al. 2012). So while the dominance of LAT-only detections supports a separate emission process >100 MeV in general, proper spectral analysis must be made to draw conclusions about an individual burst.

5.5. Energetics in the Prompt and Afterglow Phases

We first investigate the energy output in different time windows. Figure 14 allows us to qualitatively compare the energy output during the total duration of each GRB as measured in the 50–300 keV (GBM) and 100 MeV–10 GeV (LAT) ranges. In the "GBM" duration window, the flux (top left panel) is inversely proportional to the duration. A possible interpretation is that a limited amount of total energy is available for any given GRB. A longer duration then means that the average flux will decrease. Comparing the fluences (top right panel), long and short GRBs are clearly separated, with all but one of the sGRBs having fluence below 10^{-6} erg cm^{-2}. Within each group, fluence is independent of duration, suggesting that the separation arises as a result of different energy budgets, as might be expected if the groups arise from two different progenitor scenarios.

In contrast, long and short GRBs show no clear separation in the "LAT" duration window (bottom panels). While the populations occupy slightly different regions of the plots, there is a smooth transition between them. This may indicate that the emission in this window is dominated by the afterglow and that this process is similar regardless of progenitor. In the right panel, the fluence shows a tendency to increase with duration. This could have many explanations: a variable energy budget, meaning that more energetic afterglows last longer; an effect of differences in the circumburst medium, leading to varying radiative efficiency; or variations in the viewing angle with respect to the jet. We caution that there is likely also an observational bias: GRBs with favorable conditions can be studied longer; these will then have both a higher number of detected photons (i.e., greater fluence) and a longer measured duration.

Looking closer at the energetics, we can compare the LAT 100 MeV–10 GeV fluence to that of the 10 keV–1 MeV range in the GBM. We make this comparison in the "GBM" time window (left panel of Figure 15), which can be seen as a proxy for the prompt phase of the burst. We again stress that no joint spectral fits have been made and that the fluences are calculated based on different spectral fits in each range: the GBM fits are taken from the FGGC, while a PL fit is used for the LAT range (see Section 3.6). In the 1FLGC, it was found that the high-energy fluences from the joint GBM-LAT spectral fit agreed with those from LAT-only analysis, with a small discrepancy seen only for the brightest GRBs. Therefore, we do not expect any significant bias in our results, but a more thorough study needs to be performed before detailed conclusions can be drawn. Such analyses will be presented in future publications.

As found in the 1FLGC, the bulk of the population emits most of its radiation in the GBM energy range, with the high-energy emission reaching $\lesssim$20% of that in the lower band. However, given the larger sample in the 2FLGC, it is clear that this mainly applies to long GRBs. The short GRBs are more clustered around the line of equality, and several have higher fluence in the 100 MeV–10 GeV range than in the 10 keV–1 MeV one. We therefore conclude that short GRBs in the prompt phase tend to emit a relatively larger fraction of their energy at higher energies, as compared to long GRBs.

In the next step we compare the relative energy output in the 100 MeV–10 GeV range during the "GBM" (prompt) and "EXT" (afterglow) time windows of each burst (right panel of Figure 15). Similar to the results found in the 1FLGC, most GRBs are clustered around the line of equality, meaning that in the LAT energy range comparable amounts of energy are released in the prompt and afterglow phases. For long GRBs there is a large fraction where the fluence during the afterglow phase is greater than that during the prompt phase. The short GRBs instead tend to have equal fluence in the two time windows.

In the 1FLGC, there appeared to be a correlation between the photon index and GBM duration, with shorter bursts tending to have harder spectra. This was coupled to the general property that short GRBs on average have harder spectra. Figure 16 shows that this overall trend is not held up in the current larger sample. Furthermore, although the short GRBs on average have slightly harder spectra in the "GBM" time window (top left panel), this difference is not seen in the "EXT" window (top right panel). This could merely be an indication that the GRB spectra are sometimes "contaminated" by emission from lower energies, i.e., the β value of the Band function. This value is typically just below -2, and the distribution has a long tail to lower values (Gruber et al. 2014). The larger number of lGRBs means that we are more likely to see the effect in this population. Comparing the spectral index between the "GBM" and "EXT" windows, the small difference ($\Delta\Gamma \sim 0.5$) might indicate that we are seeing the early afterglow already in the "GBM" window. This possibility will be discussed further in Section 6.

The bottom left panel of Figure 16 shows that the spectral index is not dependent on flux in the "GBM" window. Instead, the bottom right panel would appear to suggest a correlation between flux and photon index in the "EXT" time window, such that stronger emission is coupled to softer spectra. This is especially obvious in bursts with lower flux. However, we caution that this is likely an observational bias. Weaker bursts will only be detected if they have harder spectra.

5.5.1. Intrinsic Energetics

In the 1FLGC, there were 10 LAT-detected GRBs with measured redshift. In the 2FLGC, the number has increased to 34, allowing us to better study their intrinsic properties. Already Figure 13 suggests that the LAT GRBs are among the brightest. Comparing with the *Swift* and GBM samples in Figure 18, it is clear that this is an intrinsic property and that the LAT preferentially detects brighter GRBs, regardless of redshift. The two panels in Figure 18 show that in order for the LAT to detect a GRB at high redshift, such a burst must be intrinsically very bright. For example, all detected GRBs at $z > 1$ have $E_{\rm iso} > 10^{52}$ erg, while detecting a GRB at $z > 4$ requires $E_{\rm iso} > 10^{54}$ erg. After 10 yr, GRB080916C is still the most distant GRB observed by the LAT, at $z = 4.35$.

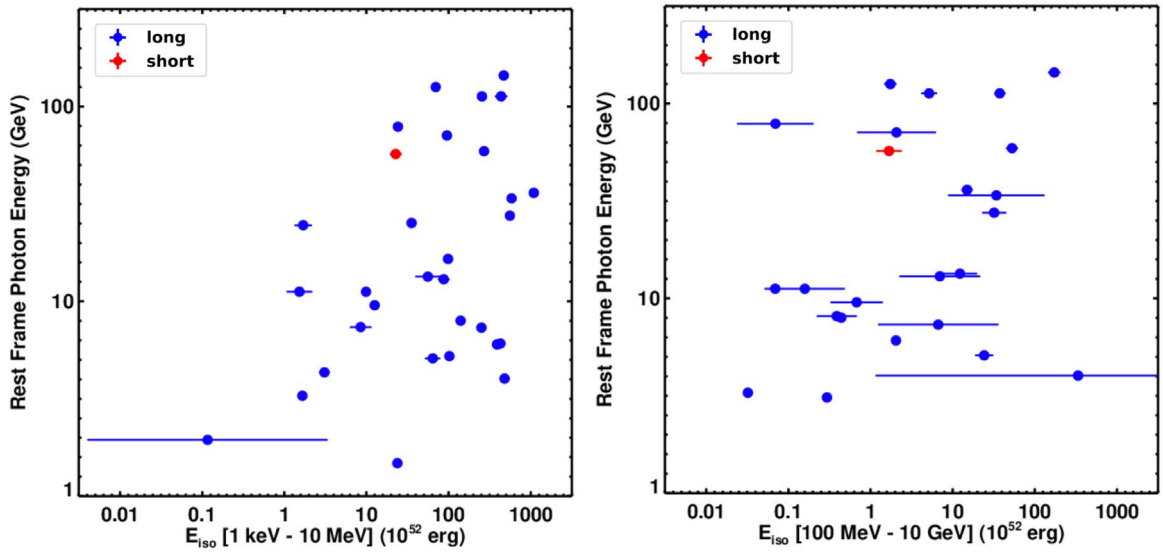

Figure 26. Energy of the highest-energy photon calculated in the rest frame vs. $E_{\rm iso}$ in the 1 keV–10 MeV (left panel) and in the 100 MeV–10 GeV (right panel) energy ranges for each GRB with redshift estimation. Blue and red circles represent long and short GRBs, respectively.

5.5.2. The Highest-energy Photons

We now turn to the highest-energy photons detected by the LAT, as presented in Figure 24. Although less than 80% of GRBs do not reach above 5 GeV in the observer frame, the figure indicates that higher energies are more common in the source frame, with ∼15% of GRBs reaching source-frame-corrected energies above 100 GeV. We note, however, that as there is only one sGRB with measured redshift, the rest-frame distribution is dominated by lGRBs. Interestingly, the fraction of GRBs detected drops smoothly as the threshold energy in the rest frame increases. It is tempting to connect this behavior to the underlying spectral distribution, such that we are seeing the limit determined by the intrinsic spectral shape, which seems to be similar for all GRBs (see Figure 16). In bright bursts more high-energy emission is produced, allowing GeV emission to be observed. Faint bursts will produce too little GeV emission, and the LAT will only detect MeV photons.

Although it is clear that the high-energy emission in general can last a long time, the highest-energy photon in a given GRB in some cases arrives relatively soon after the trigger. For example, this photon arrives within <2 s from the trigger time for ∼50% of the sGRBs in the left panel of Figure 25. The right panel of Figure 25 also shows that among the GRBs with a maximum photon energy >10 GeV, the highest-energy photon is in some cases detected before the emission in the 50–300 keV energy range is over. Particle acceleration in GRBs must be efficient in order to produce such high-energy gamma-rays within such a short time. Considering internal opacity of the jet outflow also leads us to conclude that a high bulk Lorentz factor is necessary in order for us to be able to detect these photons. Indeed, these considerations have been used to estimate a Lorentz factor well above 500 in several LAT-detected bursts (see, e.g., Abdo et al. 2009a, 2009c).

In the 1FLGC, there was a trend for the photons with highest source-frame energy to appear in the GRBs with highest 1 keV–10 MeV $E_{\rm iso}$ (Figure 21 in the 1FLGC), and the one short GRB with redshift (GRB 090510) did not follow the pattern seen in long GRBs. However, these results were based on only nine GRBs. With the greater statistics in the 2FLGC, the trend not only persists but also is extended over a greater range, as shown in the left panel of Figure 26. This indicates that the maximum rest-frame energy produced is simply a function of the total energy output. The right panel instead shows the relation between the highest energy and $E_{\rm iso}$ calculated during the "GBM" time window in the LAT energy range (100 MeV–100 GeV). In this range, the correlation is less obvious and the points are more scattered. As the energy output in the LAT range is much smaller than at lower energies (see the left panel in Figure 15), it is perhaps not surprising that the low-energy $E_{\rm iso}$ is a more reliable estimator of the energy budget. However, there are a small number of GRBs that deviate from the general trend, showing low rest-frame energies despite a large $E_{\rm iso}$. More detailed studies are required in order to understand this behavior. In both panels the region of GRB 090510, which is still the only short GRB with a redshift measurement, is populated also by long GRBs. This again points to similar conditions for long and short GRBs. Finally, the high-energy gamma-rays from GRBs offer a valuable way to probe more physics than the burst itself. For example, the interaction of >10 GeV gamma-rays from sources at cosmological distance with optical and UV photons of the extragalactic background light (EBL) causes absorption of gamma-rays, modifying the high-energy part of the spectrum. High-redshift GRBs can thereby serve as a probe of EBL opacity (Desai et al. 2017). For example, EBL attenuation could contribute to the differences between the observer and rest-frame distributions in Figure 24.

5.6. High-energy Emission Temporal Profile

In the 1FLGC the study of the temporal decay of the extended emission led to the hypothesis that this is part of an early afterglow component very similar to the afterglow component seen in the X-ray band. The stable decay index with a value around $\alpha = 1$ for the small sample of bursts in the 1FLGC was taken as support for adiabatic expansion within the fireball scenario. The index reported here remains centered around $\alpha = 0.99$. If the extended component is fast-cooling afterglow emission from either a radiative or an adiabatic fireball in a constant-density environment, the decay indices (given a photon index of −2) would be $10/7$ or 1, respectively (Katz & Piran 1997; Sari 1997; Ghisellini et al. 2010). The

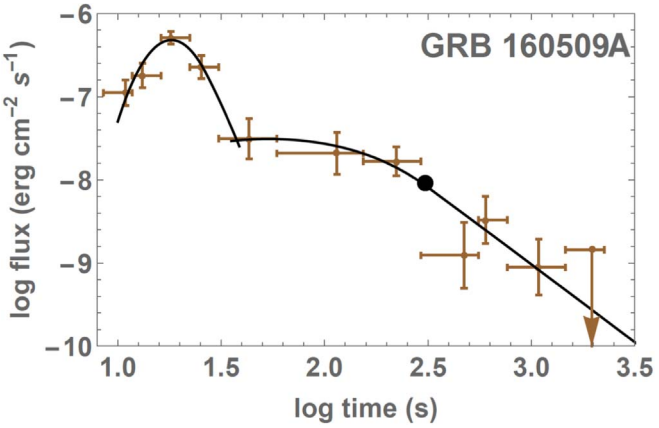

Figure 27. Light curve of GRB 160509A, together with the fit using the Willingale et al. (2007) model (solid line). The black circle indicates the end time of the plateau emission and its corresponding flux.

peak in the decay index distribution would thus primarily suggest the adiabatic scenario. Nevertheless, the range of measured indices allows also for a radiative fireball in at least a few individual bursts.

The luminosity distribution seen in Figure 23 shows that the GRBs with known redshift all have similar decay indices. Yet although the slope of the luminosity decay is similar among the GRBs, its distribution versus the elapsed time since the trigger time is scattered (left panel). In the middle panel, the time axis for each light curve has been corrected to the time in the rest frame, which reduces the spread. If the luminosity is divided by the isotropic energy of each burst, measured in the 1 keV–10 MeV range, the resulting light curves cluster even more (right panel in Figure 23), as reported by Ghisellini et al. (2010) and Nava et al. (2014). With higher statistics with respect to these studies (which were limited to a few LAT GRBs observed up until 2013), the clustering points to a strong correlation between the isotropic luminosity of the high-energy emission and the prompt isotropic energy calculated in the range 1 keV–10 MeV.

In the analysis performed in Sections 3.6.2 and 4.7, some light curves are found to be best fit with a spectral break. Such features may be related to the X-ray afterglow plateaus, which are well established, but their nature is still debated. To investigate this, we analyze all LAT GRBs with TS $\geqslant$ 64, with a sufficient number of photons. This choice of TS is dictated by the need of observing the γ-ray afterglow for a sufficiently long time to allow us to characterize the nature of the deviation from a PL. We then determine whether the light curves can be fitted within the phenomenological Willingale et al. (2007) model, used to fit the X-ray plateaus (the details of the analysis will be presented in M. Dainotti et al. 2019, in preparation).

We find that four GRBs (GRB 160509A, GRB 090902B, GRB 150627A, GRB 160816A) show a late-time flattening reminiscent of the X-ray plateaus (their light curves can be seen in Figures 20 and 22). The light curve of GRB 160509A, together with the Willingale et al. (2007) model, is presented in Figure 27. From this resemblance we infer that there is indication of the existence of a plateau in a few *Fermi*-LAT light curves. Our recovered values for T_γ, which is the time at the end of the plateau emission, are smaller than those typically found in the X-ray regime (from hundreds to a few thousand seconds; Willingale et al. 2007). This suggests that more energetic bursts have smaller plateau durations. Although a one-to-one comparison is difficult owing to the lack of corresponding X-ray observations for those bursts, it is nevertheless interesting to mention this trend for future reference and possible new observations.

5.7. Prospects for GRB Detections at VHE

The detection of VHE emission from GRB 190114C reported by the MAGIC Collaboration (Mirzoyan 2019) opened up a new era in the observations of GRBs. The bright source was seen across the electromagnetic spectrum, from radio to VHE. While studies of this burst are certain to yield interesting results, more VHE detections will be necessary to build an understanding of the mechanisms behind such emission.

The Cherenkov Telescope Array (CTA; Actis et al. 2011; The CTA Consortium et al. 2019) will mark an important milestone in the VHE range, covering the whole sky with unprecedented sensitivity. The CTA can steer to a GRB location in less than 30 s after receiving a trigger notice from a space-based instrument (see, e.g., Gilmore et al. 2013; Inoue et al. 2013). In an optimistic case, one can therefore assume that the CTA is on target within $\sim$50 s after the onset of the burst.

The GRB sample in the 2FLGC allows us to make a simple and phenomenological estimate of the detectability by VHE instruments. For this exercise, we use the observed LAT spectra as input for CTA simulations, considering only the 33 lGRBs with redshift measurements. We performed an ad hoc spectral analysis in a 2 hr interval starting at $T_{\rm LAT,0}$ +50 s in the energy range from 100 MeV to 100 GeV. The LAT data are fit using a PL spectrum. The output spectral parameters (flux, F_0, and photon index, Γ) were then used as input for the CTA tools software package `ctools`,[76] version 1.5.2, with the instrument response functions (IRFs) Prod2[77] referred to the CTA configuration in the Southern Hemisphere site. The CTA simulation requires as input the GRB location and spectral model and gives as output a TS map showing whether the source is detected or not. The extrapolation into the CTA range assumes either a PL or a cutoff PL (CUTPL) spectral model. The background is already taken into account in the used IRFs. We performed simulations over an energy range of 50 GeV–50 TeV, assuming that the CTA received the LAT detection notice with several different time delays: 0, 0.5, 1, 2, 4, 6, and 10 hr. We considered a 2 hr CTA observational interval following the notice time, assuming a flux temporal decay of $F = F_0\, t^{-\alpha}$, where α is the temporal decay index taken from Table 4. For the 0 hr delay we used all 33 GRBs, while for all the other analyses the number of cases was limited to the 27 GRBs where α could be constrained.

An important factor to consider in the VHE range (>50 GeV) is that the gamma-ray spectrum can be attenuated by $\gamma\gamma$ absorption due to the annihilation of high-energy photons with photons from the EBL. In order to include the EBL attenuation in our simulation, the cutoff energy of the CUTPL model was chosen as the critical energy defined by Ackermann et al. (2011). For the GRBs at redshift >1 (20 GRBs), we fixed the critical energy at 30 GeV (following Figure 2 of Ackermann et al. 2012b), while for the others at redshift <1 (13 GRBs) the

[76] http://cta.irap.omp.eu/ctools/users/index.html
[77] https://www.cta-observatory.org/science/cta-performance/

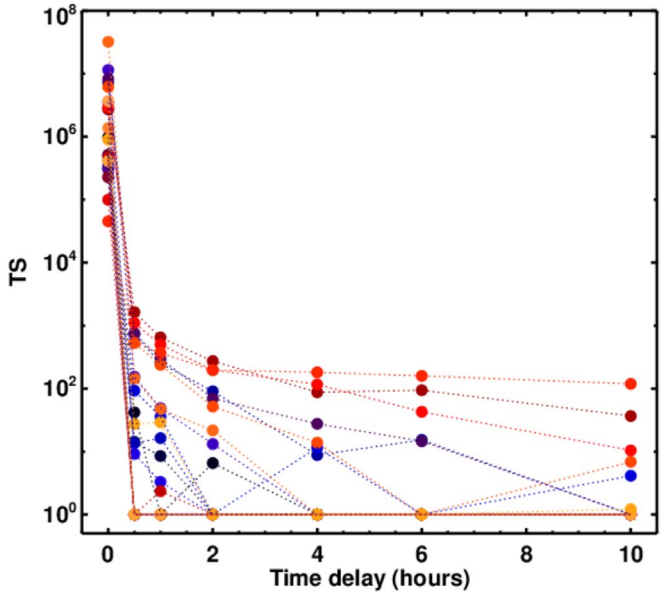

Figure 28. TS evolution with respect to the time delay (in hours) of the CTA alert reception, obtained from the analysis with a PL model, with respect to the beginning of the LAT-detected extended emission. The figure shows the TS values for 27 GRBs. For clarity, TS values less than 1 are fixed to 1.

critical energy was chosen following Ackermann et al. (2012b): $E_{\rm crit}(z) = 170(1+z)^{-2.38}$ GeV. Spectral analyses of the CTA simulated data were then performed using both PL and CUTPL spectral models.

The analyses performed without any time delay (0 hr) reveal that the CTA is able to detect all 33 GRBs with high TS, as shown in Figure 28 for the PL case. This shows that CTA telescopes would readily detect GRBs given ideal observational conditions during night time, i.e., assuming that the CTA was already on target or started observing immediately after a GRB trigger. However, the LAT data generally require more than 6 hr to be downlinked and analyzed on the ground. Figure 28 also shows the TS evolution with respect to the time delay between the LAT detection and the CTA alert reception time in the case of a PL model. The TS values decrease rapidly with time, and given a 10 hr delay from the LAT detection, the CTA can detect only two GRBs among 27 (with TS $>$ 25). In the case of the CUTPL model, all GRBs are detected only in the most optimistic observing condition, and the TS values fall below 25 for all 27 GRBs already with a 0.5 hr delay. These results show the strong need for rapid alerts and precise localizations to enable follow-up observations at VHEs.

We stress that the analysis presented here is the result of a very simplified scenario using a single spectral component. Extending this study to give more reliable estimates of the detectability with VHE instruments will require both more realistic models for the high-energy emission mechanisms in GRBs and using proper theoretical models of EBL.

5.8. LAT sGRBs and Implications for GW Observations

The recent detection of GW170817 and the coincident GRB 1701817A clearly showed a coupling between merging neutron stars, gravitational waves, and short GRBs. This has made the rapid search for counterparts also in the MeV–GeV range a high priority for the LAT. The LAT Collaboration has previously reported on follow-up studies of several GW triggers: GW150914 (Ackermann et al. 2016), LVT 151012 and GW151226 (Racusin et al. 2017), and GW170817 (Ajello et al. 2018). The first three triggers were associated with mergers of two black holes, so no electromagnetic counterpart was expected. In the last case, the location could only be observed by the LAT starting 1100 s after the GBM trigger time, and again no detection was made. Nevertheless, these events have shown the importance of a dedicated pipeline to search for high-energy counterparts for a larger class of transient events than just GRBs. The LTF pipeline described in Section 3.2 has formed the baseline for these searches. In addition, dedicated searches have been developed to cover various time intervals (also very long ones) around the GW triggers, which are thoroughly described in Vianello et al. (2017). A particular challenge is the large area given by the LIGO probability map (several hundred square degrees), much larger than for a typical GRB.

As already said, due to observational constraints, the LAT could observe the location of GW170817/GRB 170817A only after more than 1 ks. In the sample of 14 sGRBs presented here, most events are only detected up to a few seconds after the GBM trigger. However, GRB 160702A was not seen until ∼1900 s after the trigger and lasted for about 300 s. Also GRB 170127C has an unusually long duration: from ∼650 to ∼2900 s after the trigger. Neither of these events was especially bright (flux $< 10^{-5}$ erg cm^{-2} s^{-1}), showing that the LAT has the potential to find counterparts even to GW events that occur outside the FOV. Overall, the LAT has found high-energy counterparts to 5% of the sGRBs seen by the GBM. A critical discriminating factor that has been carefully addressed by Ajello et al. (2018) is the fact that the LAT can detect fainter sGRBs the earlier the observation starts, ideally within 100–200 s post-trigger. They calculated that the LAT can observe (either a detection or upper bound) ∼23% of the full-sky sGRB population within 100 s from their GBM trigger. Moreover, assuming that the LAT will have the same efficiency for GRB/GW triggers and a rate of joint GBM/GW events of 1 (2) per year, they obtained a ∼5% (∼10%) probability of detecting one or more GRB/GW events with the LAT in 1 yr, respectively. This was derived assuming that GRB/GW events will be representative of the entire GBM-detected sGRB population when observed in gamma-rays. Indeed, two other important factors affecting the detectability of such events by the LAT might be the off-axis viewing angle and the GRB distance.

Recently, von Kienlin et al. (2019) presented a search for GRBs in the entire 10 yr *Fermi*-GBM sample that show similar characteristics to GRB 170817A, i.e., a nonthermal pulse followed by a thermal component. They identified 13 candidates and concluded that the observed similarities likely arose as a result of the same processes that shaped the gamma-ray signal of GRB 170817A. We examined their sGRB sample and found that GRB 120915A has also been detected by the LAT and is included in the 2FLGC. The short duration in the LAT ($T_{\rm LAT,100} = 0.6 \pm 0.3$ s) clearly ties the high-energy emission to the prompt phase. This again shows that the LAT is likely to detect such events as long as they are in the FOV at the time of the GW trigger, as in the case of GRB 120915A (with $\theta = 11^{\circ}$).

6. Theoretical Implications

Observations of GRBs with *Fermi*-LAT have significantly broadened our understanding of the nature of high-energy

emission from these powerful transients and have led to renewed theoretical activities to model this emission (see, e.g., Gehrels & Razzaque 2013, for a review). Already the 1FLGC hinted at several new prominent characteristics of the high-energy emission: delayed onset compared to the GBM trigger; a hard spectrum, often requiring an additional component when modeling together with GBM data in the prompt phase; variable emission during the early prompt phase; and temporally extended emission beyond the prompt phase without measurable short-timescale variation. Although no joint GBM-LAT spectral fits have been performed for the 2FLGC, with its greatly enhanced sample the results presented here have firmly established at least the temporal properties as being general to the population as a whole. Modeling these characteristics gives us clues to the particle acceleration sites, environment, and radiation processes, while measurements of fluence, redshift, and energetics help us to classify the LAT-detected GRBs in the context of the broader GRB population.

Simultaneous multiwavelength observations of a handful of LAT-detected GRBs, e.g., GRB 090510 (Ackermann et al. 2010a), GRB 110731A (Ackermann et al. 2013a), and GRB 130427A (Ackermann et al. 2014; Maselli et al. 2014), have further helped constrain the origin of a few high-energy emission features, such as the temporally extended emission. Regardless of the origin of high-energy emission, merely the fact that we detect it implies that the bulk Lorentz factor of the GRB fireball (Lithwick & Sari 2001; Granot et al. 2008; Hascoët et al. 2012) is large. In particular, the fireball can be completely transparent to high-energy emission for sufficiently large bulk Lorentz factors (Razzaque et al. 2004). Furthermore, detection of $\gtrsim$10 GeV photons from GRBs has constrained models of the extragalactic background light (Abdo et al. 2010b) and the models leading to violation of Lorentz invariance (Abdo et al. 2009b). Finally, the detection of the short GRB 170817A by *Fermi*-GBM (Goldstein et al. 2017) in coincidence with the gravitational wave event GW170817 (Abbott et al. 2017a, 2017b, 2017c) has proven that at least some short GRBs originate from mergers of binary neutron stars.

The search for the origin of GeV emission from GRBs has intensified since *Fermi* was launched and the LAT has detected an increasing number of GRBs. The results presented here make these efforts even more promising, as the large sample of the 2FLGC shows that high-energy emission can be seen also from some fainter GRBs (see Figure 13). In the following, we will examine how GeV emission from GRBs can be used to test theoretical predictions. These examples are not exhaustive—rather, they are meant to illustrate various ways in which LAT observations can inform theoretical models.

6.1. Delayed Onset and Long Duration: Challenges for Emission Models

Synchrotron self-Compton (SSC) models for GeV emission are a natural extension of the synchrotron model for keV–MeV emission from GRBs, in the context of the internal shock scenario (see, e.g., Bošnjak et al. 2009; Wang et al. 2009; Ackermann et al. 2010a). However, in a simple SSC model the Compton emission can be delayed compared to synchrotron emission by at most the flux variability timescale ($\lesssim$1 s for long GRBs). Such models therefore cannot account for the $\gg$1 s delay observed in a large fraction of LAT GRBs (see Figure 7). SSC emission from late internal shocks, with much longer variability time at GeV than in MeV, can explain delayed LAT onset in some cases (see, e.g., Toma et al. 2009; Daigne et al. 2011).

A possible alternative for GeV emission during the prompt phase is hadronic emission, either proton-synchrotron radiation and radiation from $e^{\pm}$ pair cascades (Razzaque et al. 2010) or photohadronic interactions and associated cascade radiation (Asano et al. 2009). In contrast to many SSC models, hadronic models can account for delayed onset of GeV emission via a hard PL component with its flux increasing over time owing to proton acceleration and cooling of cascade particles. Hadronic models, however, require $\gtrsim$100 times more energy in the hadrons than in leptons, which is challenging to produce in GRBs. Furthermore, neither SSC nor hadronic emission mechanisms active during the prompt phase are able to explain the extended GeV emission beyond the keV–MeV $T_{\rm GBM,90}$.

The delayed onset, smooth light curve, and temporally extended emission $\gtrsim$100 MeV have led to the development of an early afterglow interpretation of high-energy radiation from the external forward shock (Kumar & Barniol Duran 2009; Ackermann et al. 2010a; Corsi et al. 2010; Ghisellini et al. 2010; Razzaque 2010). The PL spectrum and temporally extended emission are then interpreted as synchrotron radiation from the external shock. Modeling of simultaneous multi-wavelength (optical to GeV) data has shown this approach to generally fit observations for several GRBs, such as GRB 090510, GRB 110731A, and GRB 130427A. However, detection of $\gtrsim$10 GeV photons at late times from a number of GRBs (see Figure 25) is not easy to explain with the synchrotron interpretation (nor are the VHE photons from GRB 190114C seen by MAGIC). The maximum photon energy from electron-synchrotron radiation is $h\nu_{\rm max} \approx 0.24\ \phi^{-1}\ (1+z)^{-1}\Gamma\ (t)$ GeV, where $\phi^{-1} \lesssim 1$ is the acceleration efficiency for electrons and $\Gamma\ (t)$ is the bulk Lorentz factor (see, e.g., Razzaque 2010).

In light of the difficulties in simultaneously matching both the delayed onset and long duration of GeV emission, alternative models have also been proposed. For instance, several authors have pointed out that the prompt MeV emission should cause the creation of $e^{\pm}$ pairs in the medium ahead of the blast wave (e.g., Thompson & Madau 2000; Mészáros et al. 2001; Beloborodov 2002). This pair loading led Beloborodov (2005) to suggest that GeV emission arises owing to inverse Compton scattering of the prompt MeV radiation streaming through the external medium.

In Beloborodov et al. (2014), this scenario was shown to predict a delayed onset of ~1–10 s, in agreement with the majority of LAT GRBs. However, it is unclear whether also the much longer (>100 s) delays seen in a few GRBs can be explained. This would require either a very low Lorentz factor of the blast wave (not easy to reconcile with GeV emission) or a suppression of the blast-wave luminosity until it has reached a very large radius. Likewise, while the model can explain a GeV duration several times greater than that at lower energies, it may face difficulties for the LAT GRBs where the GeV duration is more than an order of magnitude longer (see panel (c) of Figure 7). Observational tests so far have also predicted rather large densities of the circumburst medium (comparable to stellar winds of $\sim 10^{-5}\,M_{\odot}\,{\rm yr}^{-1}$), which may prove challenging as more sGRBs are detected, as binary neutron stars are not expected to have a dense surrounding medium.

6.2. Fluence and Energetics of LAT GRBs: Probing the Central Engine

LAT GRBs constitute a subsample of the GBM GRBs with a flux distribution peaking at a higher value than the complete GBM sample (see Figure 13). This is also true for the fluence as evident from the same figure. On the other hand, the redshift distribution of the LAT GRBs is rather typical of *Swift*-detected GRBs (see Figure 17). As a result, the isotropic energy release and peak luminosity (Figure 18) are also typically higher for the LAT GRBs across the redshifts. These results have implications for the GRB central engines.

The nature of the GRB central engine is a fundamental question in astrophysics. A newly born magnetar is one of the two leading hypotheses (the other is a newly born black hole). The vacuum/force-free electromagnetic spin-down power of a neutron star with surface (equatorial) dipole magnetic field $B_{\rm dip}$ and spin period P is given by (Spitkovsky 2006)

$$\dot{E}_{\rm FF} \approx \frac{4\pi^4 B_{\rm dip}^2 R^6}{P^4 c^3} \sim 10^{49}\left(\frac{B_{\rm dip}}{10^{15}\,{\rm G}}\right)^2 \times \left(\frac{P}{1\,{\rm ms}}\right)^{-4}\left(\frac{R}{10\,{\rm km}}\right)^6 {\rm erg\ s^{-1}}, \quad (11)$$

where R is the neutron star radius. The maximum isotropic γ-ray power is then $\sim 10^{49}$–10^{51} erg s^{-1}, after taking into account a jet-beaming factor of up to $\sim$200 for a $\sim 6^\circ$ jet opening angle. In comparison, the measured peak luminosity for a number of LAT-detected GRBs exceeds these values, e.g., GRB 080916C ($\approx 6\times 10^{53}$ erg s^{-1}) and GRB 090510 and GRB 160625B ($\approx 4\times 10^{53}$ erg s^{-1}). The observations of LAT GRBs therefore significantly constrain the parameter space of the models with a magnetar as the GRB central engine (see, e.g., Duncan & Thompson 1992; Usov 1992; Metzger et al. 2011).

6.3. Closure Relations: Test of the Standard External Forward Shock Model

As described in Section 6.1, a possible explanation for the temporally extended emission is synchrotron emission from an external forward shock developed by collisions between outgoing ejecta and the circumburst medium. According to the model, a PL distribution of electrons radiates synchrotron emission, and the spectrum and corresponding light curve are described as a series of BPLs (e.g., Sari et al. 1998; Chevalier & Li 2000; Zhang et al. 2006; Gao et al. 2013). The indices of each segment of both spectrum and corresponding light curve are either constant or a function of the electron spectral index, and the relation between the spectral and temporal indices is called the "closure relation." The closure relations have different forms depending on the physical conditions, such as the electron cooling regime, surrounding environment profile, electron spectral index, and jet geometry.

A systematic analysis of 59 GRBs testing a set of closure relations against temporal and spectral indices computed from LAT extended emission was performed in Tak et al. (2019, submitted). Among the analyzed GRBs, 81% of them can be classified by a set of closure relations. A third of these allow both interstellar medium (ISM) and wind environments, while the remainder favor an ISM environment. The observed spectra and light curves of the extended emission in LAT GRBs are thus generally consistent with the standard external forward shock model in most cases, but there is still a significant fraction that cannot be explained by this model. The GRBs that do not match any closure relation tend to show a slower temporal decay ($\alpha < 1$). This implies the need for continuous energy injection or other physical sources to sustain the fluxes.

As already mentioned in Section 5.6, some light curves show a break or even hints of a plateau at late times. Such features can cause problems for the models used above, and instead a more phenomenological approach needs to be adopted. Using the parameters derived from fitting the light curves with the Willingale et al. (2007) model, we tested also these GRBs against the closure relations. Unfortunately, due to the large uncertainties, no conclusive results could be reached at least at this stage. Thus, further analysis and future observations are required to cast light on this topic. Additional tests in other theoretical frameworks (e.g., the models proposed by Beloborodov et al. 2014; Ito et al. 2014) will be the object of a forthcoming paper.

7. Summary and Conclusions

We have here presented the second *Fermi*-LAT GRB catalog. Compared to the 1FLGC, there are several changes and improvements to the analysis, beyond the three times longer timescale:

1. Pass 8 data have replaced Pass 6 data.
2. Over the past 2 yr, a new detection algorithm has been developed at energies above 100 MeV.
3. A BB algorithm has been employed to look for detections at 30–100 MeV.
4. All available triggers (both GBM and other space-based missions) were used in the search for LAT counterparts.

All potential detections have been processed by a dedicated and standardized analysis. This differs from both the analysis performed for the 1FLGC and the standard LAT real-time analysis. In total we find 186 detections, a much larger sample than the 35 GRBs of the 1FLGC.

The results presented in the 2FLGC have strengthened some of the conclusions from the 1FLGC, most notably the temporal characteristics. A major difference from the 1FLGC is a new definition of the duration, where we consider the first and last detected photon. Nevertheless, the properties of later onset and longer duration for the high-energy emission remain unchanged. Other trends suggested by the 1FLGC, most notably regarding the energetics and differences between long and short GRBs, have been shown not to hold with the larger sample in the 2FLGC.

While this catalog describes the temporal properties of the detections at both keV and MeV energy ranges, the spectral analysis is limited to the LAT range (100 MeV–100 GeV). This has shown to be problematic in some cases, such as when testing for breaks in the spectrum. These results are not surprising, as the division between the energy ranges is purely artifical. Nevertheless, a joint analysis is beyond the scope of this paper and will instead be the focus of a dedicated study presented in a separate publication.

The larger sample in this catalog is also reflected in the 34 GRBs with measured redshift. This has allowed us to better investigate the energetics also in the rest frame, probing both the highest-energy photons and the closure relations. The remarkable alignment seen in the decay of the luminosity further points to a strong correlation between isotropic

luminosity in the rest-frame MeV–GeV range and isotropic energy as measured at lower energies.

The 2FLGC presents the results of the first 10 yr of *Fermi*-LAT; it represents an initial step in understanding the processes behind high-energy emission from gamma-ray bursts. It is our hope that the *Fermi* data presented here will lead to a large number of follow-up analyses and continue to drive the evolution of theoretical models. Within the *Fermi*-LAT Collaboration, several such studies are already underway: focused studies on the closure relations, energetics, and the connection to VHE emission. The large sample of the 2FLGC will also allow more complete analysis of the detectability of MeV emission from GRBs, as well as detailed comparison between the energy output in the LAT range during the prompt versus afterglow phases. The collaboration is also in the process of setting up an online repository, similar to the analysis of the 2FLGC, which will automatically be updated with each new GRB detection. The past few years have truly shown the strength of *Fermi* observations, and its importance will continue for many years to come. This is especially true as the era of multimessenger studies of GRBs has just begun.

The *Fermi*-LAT Collaboration acknowledges generous ongoing support from a number of agencies and institutes that have supported both the development and the operation of the LAT, as well as scientific data analysis. These include the National Aeronautics and Space Administration and the Department of Energy in the United States; the Commissariat à l'Energie Atomique and the Centre National de la Recherche Scientifique/Institut National de Physique Nucléaire et de Physique des Particules in France; the Agenzia Spaziale Italiana and the Istituto Nazionale di Fisica Nucleare in Italy; the Ministry of Education, Culture, Sports, Science and Technology (MEXT), High Energy Accelerator Research Organization (KEK), and Japan Aerospace Exploration Agency (JAXA) in Japan; and the K. A. Wallenberg Foundation, the Swedish Research Council, and the Swedish National Space Agency in Sweden.

Additional support for science analysis during the operations phase is gratefully acknowledged from the Istituto Nazionale di Astrofisica in Italy and the Centre National d'Études Spatiales in France. This work performed in part under DOE Contract DE-AC02-76SF00515. M. Axelsson gratefully acknowledges funding from the European Union's Horizon 2020 research and innovation program under the Marie Skłodowska-Curie grant agreement No. 734303 (NEWS).

Appendix A
Tables

A1. Sample of LAT Bursts

The complete list of the *Fermi*-LAT 10 yr catalog GRBs is presented in Table 2. The first column gives the GRB name as it appeared in the corresponding GCN. The following two columns display the GRB trigger date (in UTC) and time (in Mission Elapsed Time, or MET, in seconds from 2001 January 1 UT 00:00:00). Columns (4) through (6) report the best reconstructed position using only *Fermi*-LAT data. Coordinates are expressed in the equatorial frame of epoch J2000. The localization error (Column (6)) is the error obtained from the LTF analysis. The boresight angle θ and the zenith angle ζ at trigger time are given in Columns (7) and (8). Column (9) indicates the presence or absence of an ARR. The detection significance of the LTF and LLE analysis are listed in Columns (10) and (11). The LTF TS value corresponds to the highest TS obtained during one of the four time windows listed in Table 1. LLE-only events, for which no position calculation was possible, report the best location available for that event. The reference to the burst location is then given in Column (12). When available, we report the redshift of the host galaxy in Column (13), together with its corresponding reference (Column (14)).

A2. Comparison of Duration Estimation

Table 3 presents the different burst duration estimations. The GRB class (listed in Column (2); L = long, S = short) is derived from the GBM duration in the 50–300 keV energy range (long bursts have $T_{\rm GBM,90} > 2$ s, and short bursts have $T_{\rm GBM,90} < 2$ s). All GBM values ($T_{\rm GBM,05}$, $T_{\rm GBM,95}$, and $T_{\rm GBM,90}$; Columns (3)–(5)) are taken from the FGGC. The LLE onset times and durations ($T_{\rm LLE,05}$, $T_{\rm LLE,95}$, and $T_{\rm LLE,90}$), listed in Columns (6)–(8), are calculated in the 30 MeV–1 GeV energy range. The LAT onset time $T_{\rm LAT,0}$, end time $T_{\rm LAT,1}$, and duration $T_{\rm LAT,100}$, calculated in the 100 MeV–100 GeV energy range, are given in Columns (9)–(11).

A3. Likelihood Analysis in Different Time Window

Table 4 reports the likelihood analysis results in the different time windows. The definition of the time windows is explained in Table 1. The time range of each interval in which we perform the analysis is given in Column (2). Columns (3) and (4) display the number of selected events in the ROI and the number of events predicted by the best-fit model obtained after likelihood maximization, respectively. The TS is given in Column (5). Note that only intervals with TS > 20 are displayed in the table. Columns (6) through (9) contain the value of the spectral index, flux, and fluence in each interval and, when possible, the isotropic energy calculated in the 100 MeV–100 GeV rest-frame energy band.

A4. Temporally Extended High-energy Emission

Table 5 displays the temporally extended high-energy emission analysis results. Columns (2) and (3) give the peak flux and peak flux time. These are followed by the fit parameters of the simple PL (α; Column (4)) and BPL (α_1, α_2, and T_b; Columns (5)–(7)). Column (8) reports the best-fit decay index, indicating whether the SPL or the BPL is the preferred model. The last column indicates the total duration of the extended emission.

A5. Highest-energy Events

For each GRB, Table 6 shows the highest-energy photon detected in the GBM time window (Columns (2)–(5)), as well as the highest-energy photon found overall in the time-resolved analysis (Columns (6)–(9)). For each time span the values given are the total number of photons found with probability >90% to be associated with the GRB, the energy of the most energetic photon, its arrival time, and the probability to be associated with the GRB.

Table 7 lists the 29 GRBs from which at least one photon with energy greater than 10 GeV has been detected. For each such photon, the energy and arrival time are given. For GRBs with a measured redshift, this is listed along with the corresponding source-frame energy ($E_{\rm sf}$) of each photon.

Table 2
Sample of *Fermi*-LAT GRBs, from 2008 to 2018 August

GRB Name	Date (UT)	Trigger Time (MET)	R.A. (deg, J2000)	Decl. (deg, J2000)	Loc. Err. (deg)	θ (deg)	ζ (deg)	ARR	LTF TS	LLE Sig. (σ)	Loc. GCN	Redshift	GCN
080818B	2008 Aug 18 22:40:49	240792050.080	109.46	15.0	0.47	56.4	75.0	0	26	⋯		⋯	
080825C	2008 Aug 25 14:13:48	241366429.110	234.83	−3.84	0.65	60.2	26.3	0	56	8		⋯	
080916C	2008 Sep 16 00:12:45	243216766.620	119.89	−56.7	0.07	49.0	83.8	0	2200	46		4.35	Greiner et al. (2009)
081006	2008 Oct 6 14:29:34	244996175.170	135.0	−61.95	0.38	10.8	40.3	0	97	⋯		⋯	
081009	2008 Oct 9 03:20:58	245215259.060	251.57	18.92	0.28	69.6	55.4	0	50	⋯		⋯	
081024B	2008 Oct 24 21:22:40	246576161.860	323.01	20.84	0.31	19.2	30.6	0	83	8		⋯	
081102B	2008 Nov 2 08:45:00	247308301.510	212.95	30.33	0.58	48.2	47.6	0	26	⋯		⋯	
081122A	2008 Nov 22 12:28:12	249049693.210	338.82	37.57	0.27	21.5	25.9	1	38	⋯		⋯	
081203A	2008 Dec 3 13:57:11	250005432.570	233.49	63.96	0.39	78.0	106.1	0	30	⋯		2.10	Landsman et al. (2008)
081224	2008 Dec 24 21:17:55	251846276.410	201.1	72.67	0.33	15.4	49.2	1	29	⋯		⋯	
090102	2009 Jan 2 02:55:30	252557732.850	127.56	33.46	0.65	85.5	78.7	0	20	⋯		1.55	de Ugarte Postigo et al. (2009)
090217	2009 Feb 17 04:56:42	256539404.560	205.01	−8.39	0.46	33.7	46.2	0	100	16		⋯	
090227A	2009 Feb 27 07:25:57	257412359.000	4.56	−44.63	0.34	21.6	45.4	0	33	6		⋯	
090227B	2009 Feb 27 18:31:01	257452263.407	11.8	32.2	1.80	72.7	86.6	1	⋯	15	FGGC	⋯	
090228A	2009 Feb 28 04:53:20	257489602.920	98.6	−28.79	0.21	23.8	56.6	1	41	⋯		⋯	
090323	2009 Mar 23 00:02:42	259459364.630	190.75	17.07	0.09	56.5	66.2	1	230	18		3.57	Chornock et al. (2009)
090328	2009 Mar 28 09:36:46	259925808.510	90.67	−41.95	0.12	65.7	72.4	1	290	20		0.74	Cenko et al. (2009)
090427A	2009 Apr 27 23:26:32	262567594.000	235.86	−14.05	0.11	134.0	135.4	0	40	⋯		⋯	
090510	2009 May 10 00:22:59	263607781.970	333.57	−26.62	0.05	13.5	52.3	1	2600	24		0.90	Rau et al. (2009)
090531B	2009 May 31 18:35:56	265487758.492	252.06	−36.05	⋯	21.9	49.2	0	⋯	10	FGGC	⋯	
090626	2009 Jun 26 04:32:08	267683530.880	170.19	−33.56	0.29	22.6	10.4	0	100	9		⋯	
090720B	2009 Jul 20 17:02:56	269802178.900	203.638	−51.198	0.99	56.3	94.2	1	35	⋯		⋯	
090902B	2009 Sep 2 11:05:08	273582310.320	264.95	27.33	0.04	50.3	37.6	1	3600	8		1.82	Cucchiara et al. (2009c)
090926A	2009 Sep 26 04:20:26	275631628.990	353.56	−66.37	0.06	48.0	80.4	1	3200	29		2.11	Malesani et al. (2009)
091003	2009 Oct 3 04:35:45	276237347.580	251.54	36.62	0.10	12.2	62.1	1	170	⋯		0.90	Cucchiara et al. (2009b)
091031	2009 Oct 31 12:00:28	278683230.850	71.81	−57.73	0.23	24.6	39.4	0	110	17		⋯	
091120	2009 Nov 20 04:34:40	280384482.230	226.7	−21.36	0.18	48.1	25.7	1	38	⋯		⋯	
091127	2009 Nov 27 23:25:45	281057147.490	36.65	−19.14	0.31	25.8	54.5	1	34	⋯		0.49	Cucchiara et al. (2009a)
100116A	2010 Jan 16 21:31:00	285370262.240	305.0	14.51	0.06	25.9	36.3	0	130	31		⋯	
100213C	2010 Feb 13 12:44:41	287757883.000	282.45	15.15	0.06	146.4	147.2	0	45	⋯		⋯	
100225A	2010 Feb 25 02:45:31	288758733.150	311.93	−60.51	0.34	57.0	83.7	0	47	10		⋯	
100325A	2010 Mar 25 06:36:08	291191770.030	330.26	−26.99	0.87	7.8	52.9	0	30	⋯		⋯	
100414A	2010 Apr 14 02:20:21	292904423.990	192.15	8.56	0.09	69.6	29.0	1	190	⋯		1.37	Cucchiara & Fox (2010)
100423B	2010 Apr 23 05:51:25	293694687.750	120.18	13.36	0.19	47.9	32.8	0	31	⋯		⋯	
100511A	2010 May 11 00:49:56	295231798.230	111.38	−0.99	0.07	48.0	26.2	1	93	⋯		⋯	
100620A	2010 Jun 20 02:51:29	298695091.120	87.68	−50.66	1.24	25.2	73.3	0	29	⋯		⋯	
100724B	2010 Jul 24 00:42:06	301624928.090	123.59	75.86	0.10	50.0	96.2	1	110	40		⋯	
100728A	2010 Jul 28 02:17:30	301976252.610	88.79	−15.41	0.18	60.5	36.9	1	63	⋯		1.57	Kruehler et al. (2010)
100826A	2010 Aug 26 22:58:22	304556304.900	277.71	−25.27	1.13	73.0	85.1	1	29	21		⋯	
101014A	2010 Oct 14 04:11:52	308722314.620	26.5	−48.54	0.09	55.0	102.6	1	67	12		⋯	
101107A	2010 Nov 7 00:16:25	310781787.120	170.27	23.88	0.20	36.6	28.4	0	47	⋯		⋯	
101123A	2010 Nov 23 22:51:34	312245496.973	135.16	1.91	1.00	77.4	97.8	0	⋯	8	FGGC	⋯	
101227B	2010 Dec 27 09:45:06	315135908.570	240.21	−15.93	0.32	13.7	37.3	0	27	⋯		⋯	
110120A	2011 Jan 20 15:59:39	317231981.230	61.62	−12.02	0.20	14.6	31.5	1	67	6		⋯	
110123A	2011 Jan 23 19:17:45	317503067.050	240.61	28.37	0.22	55.4	91.9	1	62	⋯		⋯	

Table 2
(Continued)

GRB Name	Date (UT)	Trigger Time (MET)	R.A. (deg, J2000)	Decl. (deg, J2000)	Loc. Err. (deg)	θ (deg)	ζ (deg)	ARR	LTF TS	LLE Sig. (σ)	Loc. GCN	Redshift	GCN
110213A	2011 Feb 13 05:17:11	319267033.280	42.98	49.11	0.22	98.6	53.2	0	28	⋯		1.46	Milne & Cenko (2011)
110328B	2011 Mar 28 12:29:19	323008161.190	121.66	41.52	0.16	36.0	43.3	0	50	29		⋯	
110428A	2011 Apr 28 09:18:30	325675112.400	5.42	65.01	0.18	34.6	84.3	0	52	⋯		⋯	
110518A	2011 May 18 20:38:10	327443892.000	67.19	−34.27	0.19	165.9	124.1	0	40	⋯		⋯	
110529A	2011 May 29 00:48:42	328322924.870	118.33	67.91	1.50	30.0	79.9	1	⋯	15	FGGC	⋯	
110625A	2011 Jun 25 21:08:18	330728900.230	286.38	6.4	0.13	87.9	51.4	1	55	⋯		⋯	
110721A	2011 Jul 21 04:47:43	332916465.760	333.53	−38.58	0.12	40.2	82.9	1	220	61		⋯	
110728A	2011 Jul 28 01:20:22	333508824.810	173.57	4.34	0.62	41.7	16.8	0	43	⋯		⋯	
110731A	2011 Jul 31 11:09:29	333803371.950	280.42	−28.65	0.24	2.9	50.7	1	390	20		2.83	Tanvir et al. (2011)
110903A	2011 Sep 3 02:39:34	336710376.420	197.26	58.85	0.07	44.3	93.9	0	49	⋯		⋯	
110921B	2011 Sep 21 21:52:45	338334767.090	5.77	−26.59	0.39	33.9	21.2	1	50	7		⋯	
111210B	2011 Dec 10 08:37:39	345199061.000	122.51	44.09	0.82	28.3	24.1	0	34	⋯		⋯	
120107A	2012 Jan 7 09:12:15	347620337.410	245.01	−70.59	0.34	46.8	96.7	0	30	⋯		⋯	
120226A	2012 Feb 26 20:54:17	351982459.030	302.97	48.98	0.68	37.1	42.2	1	37	12		⋯	
120316A	2012 Mar 16 00:11:02	353549464.560	57.35	−56.41	0.31	9.9	48.7	0	57	5		⋯	
120328B	2012 Mar 28 06:26:20	354608782.953	228.14	22.8	1.00	68.5	106.6	0	⋯	8	FGGC	⋯	
120420B	2012 Apr 20 20:35:13	356646915.070	108.77	15.17	0.29	109.7	76.8	0	29	⋯		⋯	
120526A	2012 May 26 07:16:40	359709402.760	53.82	−35.23	0.11	109.7	62.9	0	110	⋯		⋯	
120624B	2012 Jun 24 22:23:54	362269436.930	170.91	8.94	0.21	68.2	26.6	1	450	9		2.20	de Ugarte Postigo et al. (2013a)
120709A	2012 Jul 9 21:11:40	363561103.370	318.8	−50.42	0.40	27.8	40.5	0	84	9		⋯	
120711A	2012 Jul 11 02:44:53	363667496.290	94.64	−70.88	0.13	134.5	85.0	1	140	⋯		1.41	Tanvir et al. (2012)
120729A	2012 Jul 29 10:56:12	365252175.660	13.26	49.91	0.38	82.6	32.7	0	35	⋯		0.80	Tanvir & Ball (2012)
120830A	2012 Aug 30 07:07:03	368003226.540	88.59	−28.79	0.62	38.7	75.3	0	44	⋯		⋯	
120911B	2012 Sep 11 06:26:12	369037575.000	172.66	−37.5	0.60	66.1	22.2	0	340	18		⋯	
120915A	2012 Sep 15 00:00:41	369360044.640	240.95	57.04	1.76	10.8	59.2	0	32	⋯		⋯	
120919B	2012 Sep 19 01:14:23	369710066.070	302.73	−37.73	0.14	22.9	65.9	0	30	⋯		⋯	
121011A	2012 Oct 11 11:15:25	371646928.697	260.2	41.14	0.01	55.9	84.8	0	⋯	8	GCN13845	⋯	
121029A	2012 Oct 29 08:24:19	373191862.930	229.07	−25.56	0.21	61.2	42.0	1	40	⋯		⋯	
121123B	2012 Nov 23 10:35:55	375359758.710	28.62	−24.06	0.50	78.8	76.4	0	27	⋯		⋯	
121225B	2012 Dec 25 10:00:53	378122456.583	310.45	−34.83	1.50	64.3	90.7	0	⋯	8	FGGC	⋯	
130305A	2013 Mar 5 11:39:11	384176354.369	116.765	52.025	0.06	41.5	99.6	0	⋯	19	GCN14257	⋯	
130310A	2013 Mar 10 20:09:41	384638984.500	142.38	−17.1	0.47	75.6	49.8	1	47	11		⋯	
130325A	2013 Mar 25 04:51:54	385879917.300	122.97	−19.15	0.18	47.3	76.1	1	60	⋯		⋯	
130327B	2013 Mar 27 08:24:04	386065447.050	218.26	−69.76	0.21	46.3	86.2	1	250	⋯		⋯	
130427A	2013 Apr 27 07:47:06	388741629.420	173.14	27.73	0.04	46.4	62.8	1	4200	15		0.34	Xu et al. (2013)
130502B	2013 May 2 07:51:11	389173874.760	66.65	70.83	0.32	46.4	96.4	0	330	8		⋯	
130504C	2013 May 4 23:28:57	389402940.520	91.55	3.78	0.12	47.6	52.3	1	91	29		⋯	
130518A	2013 May 18 13:54:37	390578080.530	355.59	47.53	0.19	40.3	82.4	1	140	19		2.49	Sanchez-Ramirez et al. (2013)
130606B	2013 Jun 6 11:55:33	392212536.630	218.57	−22.15	0.11	90.5	10.9	1	87	⋯		⋯	
130702A	2013 Jul 2 00:05:23	394416326.080	216.39	16.15	0.62	76.7	78.9	0	26	⋯		0.14	Leloudas et al. (2013)
130821A	2013 Aug 21 16:10:28	398794231.010	314.23	−11.52	0.18	34.9	49.2	1	170	16		⋯	
130828A	2013 Aug 28 07:20:00	399367203.150	259.72	28.21	0.29	39.9	45.5	1	150	9		⋯	
130907A	2013 Sep 7 21:41:13	400282876.090	215.92	45.7	0.26	105.4	57.2	0	30	⋯		1.24	de Ugarte Postigo et al. (2013c)

Table 2
(Continued)

GRB Name	Date (UT)	Trigger Time (MET)	R.A. (deg, J2000)	Decl. (deg, J2000)	Loc. Err. (deg)	θ (deg)	ζ (deg)	ARR	LTF TS	LLE Sig. (σ)	Loc. GCN	Redshift	GCN
131014A	2013 Oct 14 05:09:00	403420143.200	100.78	−20.76	0.81	72.5	76.0	1	98	17		⋯	
131029A	2013 Oct 29 23:20:48	404781651.580	200.85	48.03	0.18	59.8	94.1	0	110	⋯		⋯	
131108A	2013 Nov 8 20:41:55	405636118.760	156.81	9.57	0.22	20.4	21.9	1	1200	37		2.40	de Ugarte Postigo et al. (2013b)
131209A	2013 Dec 9 13:07:56	408287279.960	137.06	−33.9	1.16	19.8	53.6	0	29	⋯		⋯	
131216A	2013 Dec 16 01:56:32	408851795.063	91.59	−35.5	2.24	44.6	77.2	1	⋯	7	FGGC	⋯	
131231A	2013 Dec 31 04:45:16	410157919.080	10.55	−1.72	0.05	37.2	39.9	1	240	18		0.64	Xu et al. (2014b)
140102A	2014 Jan 2 21:17:37	410390260.810	212.02	1.47	0.24	47.2	44.7	1	55	11		⋯	
140104B	2014 Jan 4 17:32:03	410549526.150	218.76	−8.98	0.18	17.6	36.5	0	62	⋯		⋯	
140110A	2014 Jan 10 06:18:37	411027520.940	29.12	−36.5	0.25	36.1	64.6	0	200	13		⋯	
140124A	2014 Jan 24 12:38:31	412259914.190	59.27	36.86	0.33	19.4	65.6	0	26	⋯		⋯	
140206B	2014 Feb 6 06:36:12	413361375.840	315.24	−8.79	0.08	46.2	86.0	1	300	39		⋯	
140219A	2014 Feb 19 19:46:32	414531995.240	158.2	7.26	0.85	96.2	113.4	0	26	⋯		⋯	
140323A	2014 Mar 23 10:22:53	417262976.120	356.52	−79.92	0.18	30.3	68.4	0	40	⋯		⋯	
140402A	2014 Apr 2 00:10:06	418090209.990	207.66	5.97	0.16	13.7	46.0	0	93	8		⋯	
140416A	2014 Apr 16 01:26:40	419304403.930	35.74	42.1	0.10	138.8	94.8	0	34	⋯		⋯	
140523A	2014 May 23 03:05:57	422507160.630	133.09	24.83	0.38	55.4	26.4	0	180	⋯		⋯	
140528A	2014 May 28 20:05:22	423000325.750	280.59	−59.46	0.36	46.2	66.3	1	31	⋯		⋯	
140619B	2014 Jun 19 11:24:40	424869883.520	132.66	−9.65	0.20	38.9	25.8	0	210	10		⋯	
140723A	2014 Jul 23 01:36:30	427772193.730	211.05	−3.57	0.51	54.4	38.6	0	110	8		⋯	
140729A	2014 Jul 29 00:36:53	428287016.710	193.9	15.42	0.26	26.5	40.9	0	69	⋯		⋯	
140810A	2014 Aug 10 18:46:10	429389173.090	118.93	27.4	0.07	123.5	89.3	1	79	⋯		⋯	
140825A	2014 Aug 25 06:55:25	430642528.000	89.01	−12.16	0.57	113.4	112.0	0	19	⋯		⋯	
140928A	2014 Sep 28 10:29:53	433592996.550	43.76	−55.92	0.10	110.0	111.3	0	57	⋯		⋯	
141012A	2014 Oct 12 18:33:17	434831600.670	289.92	−53.0	0.27	47.2	94.7	0	110	⋯		⋯	
141028A	2014 Oct 28 10:54:46	436186489.780	322.78	−0.64	0.27	36.4	48.1	1	130	31		2.33	Xu et al. (2014a)
141102A	2014 Nov 2 12:51:39	436625502.260	209.07	−46.73	0.68	52.3	53.5	1	34	⋯		⋯	
141113A	2014 Nov 13 08:17:43	437559466.500	182.32	77.38	0.71	53.7	86.4	0	37	⋯		⋯	
141207A	2014 Dec 7 19:11:21	439672284.100	159.8	3.95	0.20	61.1	36.8	0	260	15		⋯	
141221B	2014 Dec 21 21:31:48	440890311.780	99.12	−66.9	0.33	38.7	84.3	0	31	⋯		⋯	
141222A	2014 Dec 22 07:08:57	440924940.390	178.0	−57.31	0.08	45.9	93.5	0	150	8		⋯	
150118B	2015 Jan 18 09:48:17	443267300.770	240.23	−35.93	0.56	65.3	91.7	1	28	6		⋯	
150202B	2015 Feb 2 23:59:08	444614351.270	86.27	59.05	0.33	17.2	66.9	1	26	20		⋯	
150210A	2015 Feb 10 22:26:24	445299987.290	112.28	13.57	0.43	53.7	10.0	0	92	14		⋯	
150314A	2015 Mar 14 04:54:50	448001693.860	126.12	63.79	0.72	45.1	91.9	1	30	6		1.76	de Ugarte Postigo et al. (2015a)
150403A	2015 Apr 3 21:54:10	449790853.960	311.75	−62.46	0.23	55.3	105.1	1	46	17		2.06	Pugliese et al. (2015)
150416A	2015 Apr 16 18:33:25	450902008.965	58.75	52.96	1.93	68.6	90.7	0	⋯	9	FGGC	⋯	
150510A	2015 May 10 03:19:53	452920796.740	16.42	4.91	0.33	56.2	11.4	1	53	12		⋯	
150513A	2015 May 13 20:33:15	453241998.250	49.06	−22.91	0.04	51.8	16.5	0	⋯	8	GCN17810	⋯	
150514A	2015 May 14 18:35:05	453321308.350	74.92	−60.86	0.15	39.2	59.1	0	31	⋯		0.81	de Ugarte Postigo et al. (2015b)
150523A	2015 May 23 09:29:48	454066191.080	115.34	−45.43	0.08	24.8	54.7	1	220	8		⋯	
150627A	2015 Jun 27 04:23:23	457071806.680	117.5	−51.55	0.06	74.7	97.9	1	240	9		⋯	
150702A	2015 Jul 2 23:56:38	457574202.550	52.59	−56.88	0.54	117.5	88.1	0	33	⋯		⋯	
150820A	2015 Aug 20 21:07:15	461797639.642	258.65	−48.33	15.30	23.0	66.6	0	⋯	6	FGGC	⋯	

Table 2
(Continued)

GRB Name	Date (UT)	Trigger Time (MET)	R.A. (deg, J2000)	Decl. (deg, J2000)	Loc. Err. (deg)	θ (deg)	ζ (deg)	ARR	LTF TS	LLE Sig. (σ)	Loc. GCN	Redshift	GCN
150902A	2015 Sep 2 17:35:39	462908143.360	214.95	−69.38	0.18	37.3	87.1	1	140	21		⋯	
151006A	2015 Oct 6 09:54:57	465818101.825	147.426	70.504	0.00	30.6	80.5	0	⋯	24	GCN18403	⋯	
160101B	2016 Jan 1 05:10:12	473317816.860	1.36	55.23	1.37	9.0	59.0	0	⋯	13	FGGC	⋯	
160310A	2016 Mar 10 00:22:58	479262182.470	98.78	−7.12	0.06	62.8	29.9	0	28	⋯		⋯	
160314B	2016 Mar 14 22:17:53	479686677.730	167.78	45.71	0.79	60.7	110.5	0	29	⋯		⋯	
160325A	2016 Mar 25 06:59:21	480581965.510	16.21	−72.66	0.24	7.2	55.5	0	83	6		⋯	
160422A	2016 Apr 22 11:59:00	483019144.810	42.05	−57.9	0.10	53.5	102.4	1	36	⋯		⋯	
160503A	2016 May 3 13:36:32	483975396.000	358.99	−1.24	0.88	25.1	33.9	0	33	⋯		⋯	
160509A	2016 May 9 08:58:46	484477130.220	310.39	76.04	0.30	33.1	67.8	1	610	29		1.17	Tanvir et al. (2016)
160521B	2016 May 21 09:13:58	485514842.030	148.04	79.02	0.13	47.0	94.5	1	69	⋯		⋯	
160623A	2016 Jun 23 05:00:34	488350838.230	315.25	42.22	0.09	83.9	112.2	0	240	⋯		0.37	Malesani et al. (2016)
160625B	2016 Jun 25 22:40:16	488587220.275	308.57	6.93	0.07	41.2	40.1	1	1500	49		1.41	Xu et al. (2016)
160702A	2016 Jul 02 12:22:24	489154948.000	231.09	9.07	0.21	72.0	59.2	0	31	⋯		⋯	
160709A	2016 Jul 09 19:49:03	489786547.510	236.11	−28.51	0.27	47.6	82.2	0	210	15		⋯	
160816A	2016 Aug 16 17:30:57	493061461.980	322.32	37.14	0.23	33.4	18.3	1	190	7		⋯	
160821A	2016 Aug 21 20:34:30	493504474.040	171.29	42.29	0.12	19.0	66.9	1	220	31		⋯	
160829A	2016 Aug 29 08:01:37	494150501.650	201.72	−56.78	0.10	14.5	56.9	1	30	⋯		⋯	
160905A	2016 Sep 05 11:18:55	494767139.910	162.01	−50.88	0.10	17.1	57.5	1	140	22		⋯	
160910A	2016 Sep 10 17:19:39	495220783.160	221.31	38.81	0.59	71.4	79.0	1	38	20		⋯	
160917B	2016 Sep 17 10:56:11	495802575.859	201.36	20.93	3.73	52.3	29.9	0	⋯	7	FGGC	⋯	
160917A	2016 Sep 17 11:30:19	495804623.286	295.668	46.403	0.01	46.1	89.7	0	⋯	7	GCN19927	⋯	
161015A	2016 Oct 15 17:03:07	498243791.040	269.13	30.16	0.42	46.1	32.9	1	65	⋯		⋯	
161109A	2016 Nov 09 06:18:45	500365129.660	157.85	61.83	0.39	77.9	112.5	0	41	⋯		⋯	
170115B	2017 Jan 15 17:49:14	506195359.030	189.32	−46.63	0.74	36.0	42.5	1	67	13		⋯	
170127C	2017 Jan 27 01:35:47	507173752.790	338.98	−63.97	0.52	142.2	92.2	1	28	⋯		⋯	
170214A	2017 Feb 14 15:34:26	508779271.920	256.32	−1.88	0.08	33.2	21.9	1	1100	46		2.53	Kruehler et al. (2017)
170228A	2017 Feb 28 19:03:00	510001385.710	239.66	−6.49	2.02	65.1	32.0	0	31	⋯		⋯	
170306B	2017 Mar 06 14:07:22	510502047.270	154.54	51.55	0.71	54.4	64.9	1	34	⋯		⋯	
170329A	2017 Mar 29 09:17:06	512471831.940	356.68	9.77	0.60	46.2	12.0	0	51	⋯		⋯	
170405A	2017 Apr 05 18:39:22	513110367.880	219.59	−25.21	0.55	52.0	60.5	1	47	19		3.51	de Ugarte Postigo et al. (2017)
170409A	2017 Apr 09 02:42:00	513398525.490	347.53	−7.17	0.10	85.9	66.6	1	47	⋯		⋯	
170424A	2017 Apr 24 10:12:30	514721555.760	343.7	−45.12	0.69	57.4	76.6	0	34	12		⋯	
170510A	2017 May 10 05:12:25	516085950.730	160.21	−39.28	0.49	66.4	23.5	1	35	8		⋯	
170522A	2017 May 22 15:45:35	517160740.290	139.35	25.67	0.23	49.4	74.5	1	69	⋯		⋯	
170728B	2017 Jul 28 23:03:19	522975804.430	237.43	70.85	1.01	31.5	68.1	1	30	6		⋯	
170808B	2017 Aug 08 22:27:43	523924068.100	145.72	1.61	0.71	64.8	17.5	1	46	7		⋯	
170813A	2017 Aug 13 01:13:08	524279593.800	200.45	−5.49	0.75	41.1	22.6	0	27	⋯		⋯	
170825B	2017 Aug 25 07:22:01	525338526.420	285.64	−32.55	1.02	50.5	79.5	0	25	⋯		⋯	
170906A	2017 Sep 06 00:43:08	526351393.150	203.94	−47.12	0.10	89.1	89.1	0	190	⋯		⋯	
170921B	2017 Sep 21 04:02:11	527659336.510	123.93	52.67	0.26	104.6	78.2	0	28	⋯		⋯	
171010A	2017 Oct 10 19:00:50	529354855.570	66.54	−10.44	0.10	114.7	94.1	1	220	⋯		0.33	Kankare et al. (2017)
171011C	2017 Oct 11 19:26:27	529442792.950	168.48	10.03	0.82	43.2	52.7	0	36	⋯		⋯	
171102A	2017 Nov 02 02:33:35	531282820.990	187.72	54.01	0.82	45.4	64.8	1	29	⋯		⋯	
171120A	2017 Nov 20 13:20:02	532876807.370	163.82	22.41	0.20	25.0	13.0	1	120	⋯		⋯	
171124A	2017 Nov 24 05:37:56	533194681.510	335.52	35.24	0.20	19.2	44.5	0	92	⋯		⋯	

Table 2
(Continued)

GRB Name	Date (UT)	Trigger Time (MET)	R.A. (deg, J2000)	Decl. (deg, J2000)	Loc. Err. (deg)	θ (deg)	ζ (deg)	ARR	LTF TS	LLE Sig. (σ)	Loc. GCN	Redshift	GCN
171210A	2017 Dec 10 11:49:15	534599360.260	335.29	24.44	0.32	51.1	3.5	1	120	14		⋯	
171212B	2017 Dec 12 10:24:18	534767063.510	39.42	−70.63	0.43	11.5	61.5	0	26	⋯		⋯	
180113C	2018 Jan 13 10:02:05	537530530.407	174.63	−64.74	1.00	62.6	108.9	1	⋯	40	FGGC	⋯	
180210A	2018 Feb 10 12:24:38	539958283.550	1.83	18.49	0.12	34.2	20.0	1	160	⋯		⋯	
180305A	2018 Mar 05 09:26:08	541934773.660	49.67	32.1	0.11	74.9	89.7	0	29	8		⋯	
180526A	2018 May 26 11:04:09	549025454.000	108.48	3.64	0.27	82.2	109.7	0	46	⋯		⋯	
180703A	2018 Jul 03 21:01:40	552344505.490	6.56	−67.1	0.33	44.0	94.0	0	54	18		⋯	
180703B	2018 Jul 03 22:46:51	552350816.320	96.92	−29.88	0.44	32.2	44.4	0	41	⋯		⋯	
180718B	2018 Jul 18 18:18:24	553630709.460	44.48	−30.33	0.95	46.5	43.1	0	37	⋯		⋯	
180720B	2018 Jul 20 14:21:39	553789304.650	0.59	−2.95	0.11	49.1	7.0	0	660	24		0.65	

Note. For LLE-only GRBs, the localizations are from GCN 13845 (Racusin et al. 2012), GCN 14257 (Cummings & Palmer 2013), GCN 17810 (Kocevski et al. 2015), GCN 18403 (Goad et al. 2015), and GCN 19927 (Evans et al. 2016).

Table 3
Comparison between Duration Estimators for the Detected *Fermi*-LAT GRBs

GRB Name	Class	$T_{GBM,05}$ (s)	$T_{GBM,95}$ (s)	$T_{GBM,90}$ (s)	$T_{LLE,05}$ (s)	$T_{LLE,95}$ (s)	$T_{LLE,90}$ (s)	$T_{LAT,0}$ (s)	$T_{LAT,1}$ (s)	$T_{LAT,100}$ (s)
080818B	(L)	−0.51	12.86	13.38	⋯	⋯	⋯	9018.9	9482.8	500 ± 200
080825C	(L)	1.2	22.21	20.99	2.84	4.05	1.20	3.1	173.5	170.4 ± 0.7
080916C	(L)	1.3	64.26	62.98	1.00	46.55	45.55	3.0	1531.8	1500 ± 200
081006	(L)	−0.26	6.14	6.40	⋯	⋯	⋯	0.8	62.3	60 ± 20
081009	(L)	1.3	42.69	41.34	⋯	⋯	⋯	67.8	1250.1	1200 ± 200
081024B	(S)	−0.064	0.58	0.64	−0.04	1.28	1.32	0.2	2.2	2.02 ± 0.04
081102B	(S)	−0.064	1.66	1.73	⋯	⋯	⋯	0.3	0.4	0.15 ± 0.03
081122A	(L)	−0.26	23.04	23.30	⋯	⋯	⋯	23.5	66.5	40 ± 20
081203A	(L)	*	214.00	214.00	⋯	⋯	⋯	291.9	379.7	90 ± 10
081224	(L)	0.74	17.18	16.45	⋯	⋯	⋯	76.5	339.2	260 ± 40
090102	(L)	1.5	28.16	26.62	⋯	⋯	⋯	3915.9	4404.8	500 ± 300
090217	(L)	0.83	34.11	33.28	1.96	15.50	13.54	4.1	71.6	68 ± 10
090227A	(L)	0.003	16.19	16.19	1.15	11.05	9.90	2.9	204.3	201.4 ± 0.2
090227B	(S)	−0.016	0.29	0.30	0.04	1.18	1.14	⋯	⋯	⋯
090228A	(S)	*	0.45	0.45	⋯	⋯	⋯	0.1	2.1	2.0 ± 0.1
090323	(L)	8.7	142.59	133.89	7.24	93.41	86.18	9.3	5321.6	5312 ± 8
090328	(L)	4.4	66.05	61.70	8.05	37.02	28.97	14.4	6150.6	6140 ± 70
090427A	(L)	*	15.00	15.00	⋯	⋯	⋯	422.9	435.6	10 ± 10
090510	(S)	−0.048	0.91	0.96	0.54	5.93	5.40	0.0	170.0	170 ± 2
090531B	(S)	*	0.77	0.77	−0.07	0.00	0.07	⋯	⋯	⋯
090626	(L)	1.5	50.43	48.90	21.48	22.37	0.89	9.0	557.3	550 ± 90
090720B	(L)	−0.26	10.50	10.75	⋯	⋯	⋯	0.1	1.7	1.6 ± 0.4
090902B	(L)	2.8	22.14	19.33	−0.65	17.23	17.88	0.5	884.2	880 ± 60
090926A	(L)	2.2	15.94	13.76	1.15	16.71	15.56	2.2	4419.5	4420 ± 50
091003	(L)	0.83	21.06	20.22	⋯	⋯	⋯	1.0	392.0	390 ± 10
091031	(L)	1.4	35.33	33.92	−1.53	15.09	16.62	0.1	408.2	410 ± 30
091120	(L)	1.0	51.20	50.18	⋯	⋯	⋯	31.8	803.9	770 ± 20
091127	(L)	0.003	8.70	8.70	⋯	⋯	⋯	8.6	35.4	30 ± 10
100116A	(L)	0.58	103.11	102.53	89.94	96.59	6.66	77.5	730.4	650 ± 50
100213C	(L)	*	60.00	60.00	⋯	⋯	⋯	2707.2	3389.0	700 ± 300
100225A	(L)	−0.26	12.74	12.99	2.75	9.74	6.99	6.6	1012.4	1010 ± 20
100325A	(L)	−0.38	6.72	7.10	⋯	⋯	⋯	0.2	1.2	0.9 ± 0.2
100414A	(L)	1.9	28.35	26.50	⋯	⋯	⋯	18.7	5506.1	5490 ± 30
100423B	(L)	1.6	18.11	16.51	⋯	⋯	⋯	166.7	180.6	14 ± 7
100511A	(L)	0.83	43.27	42.43	⋯	⋯	⋯	11.6	6338.2	6300 ± 700
100620A	(L)	0.19	52.03	51.84	⋯	⋯	⋯	3.8	42.8	39 ± 6
100724B	(L)	8.2	122.88	114.69	2.63	102.44	99.81	9.1	53.6	45 ± 6
100728A	(L)	13	178.69	165.38	⋯	⋯	⋯	248.6	1340.5	1090 ± 40
100826A	(L)	8.7	93.70	84.99	18.20	39.28	21.09	33.5	61.4	28 ± 6
101014A	(L)	1.4	450.82	449.42	208.72	210.38	1.67	2270.7	4196.0	1930 ± 50
101107A	(L)	2.3	378.12	375.81	⋯	⋯	⋯	134.0	239.4	105 ± 4
101123A	(L)	41	145.41	103.94	43.43	46.13	2.70	⋯	⋯	⋯
101227B	(L)	0.77	154.12	153.35	⋯	⋯	⋯	17.3	23.8	7 ± 3
110120A	(L)	0.003	26.18	26.17	0.29	0.53	0.23	0.6	1112.8	1100 ± 200
110123A	(L)	0.70	18.56	17.86	⋯	⋯	⋯	51.6	527.0	480 ± 20
110213A	(L)	−0.77	33.54	34.30	⋯	⋯	⋯	1261.4	1944.2	700 ± 400
110328B	(L)	2.6	86.53	83.97	−3.05	23.23	26.27	102.5	737.2	630 ± 60
110428A	(L)	2.7	8.32	5.63	⋯	⋯	⋯	7.3	393.5	386.2 ± 0.3
110518A	(L)	*	35.00	35.00	⋯	⋯	⋯	1968.2	2364.2	400 ± 200
110529A	(S)	−0.13	0.38	0.51	0.01	0.11	0.09	⋯	⋯	⋯
110625A	(L)	3.8	30.72	26.88	⋯	⋯	⋯	205.9	577.2	400 ± 100
110721A	(L)	0.003	21.82	21.82	−0.75	5.25	6.00	0.0	120.6	121 ± 3
110728A	(S)	−0.13	0.58	0.70	⋯	⋯	⋯	0.4	3.0	2.6 ± 0.9
110731A	(L)	0.003	7.49	7.49	2.11	8.37	6.26	1.1	436.0	430 ± 10
110903A	(L)	−0.26	341.00	341.25	⋯	⋯	⋯	46.7	370.1	320 ± 50
110921B	(L)	0.90	18.56	17.66	17.07	18.01	0.93	7.4	321.6	310 ± 50
111210B	(L)	*	60.00	60.00	⋯	⋯	⋯	6.5	394.0	390 ± 70
120107A	(L)	0.064	23.10	23.04	⋯	⋯	⋯	1.3	48.8	50 ± 10
120226A	(L)	4.4	57.34	52.99	4.46	33.38	28.93	29.4	283.6	250 ± 20
120316A	(L)	1.5	28.16	26.62	11.31	11.71	0.40	15.0	545.0	530 ± 30
120328B	(L)	3.8	33.54	29.70	4.51	7.25	2.74	⋯	⋯	⋯
120420B	(L)	0.003	254.92	254.91	⋯	⋯	⋯	3501.7	3908.0	410 ± 10
120526A	(L)	3.1	46.72	43.65	⋯	⋯	⋯	692.2	3306.3	2600 ± 200

Table 3
(Continued)

GRB Name	Class	$T_{\rm GBM,05}$ (s)	$T_{\rm GBM,95}$ (s)	$T_{\rm GBM,90}$ (s)	$T_{\rm LLE,05}$ (s)	$T_{\rm LLE,95}$ (s)	$T_{\rm LLE,90}$ (s)	$T_{\rm LAT,0}$ (s)	$T_{\rm LAT,1}$ (s)	$T_{\rm LAT,100}$ (s)
120624B	(L)	−260	14.34	271.36	5.76	9.12	3.36	73.7	1103.9	1030 ± 30
120709A	(L)	−0.13	27.20	27.33	−0.12	0.34	0.46	0.1	695.9	700 ± 10
120711A	(L)	62	106.50	44.03	⋯	⋯	⋯	393.3	5431.6	5000 ± 800
120729A	(L)	−1.0	24.45	25.47	⋯	⋯	⋯	396.9	432.0	40 ± 10
120830A	(S)	*	0.90	0.90	⋯	⋯	⋯	0.7	10.7	10.0 ± 0.2
120911B	(L)	*	69.00	69.00	7.14	35.37	28.23	9.2	217.8	209 ± 2
120915A	(S)	−0.32	0.26	0.58	⋯	⋯	⋯	0.2	0.8	0.6 ± 0.3
120919B	(L)	2.0	120.07	118.02	⋯	⋯	⋯	121.2	605.3	500 ± 200
121011A	(L)	1.0	66.82	65.79	−0.63	7.21	7.84	⋯	⋯	⋯
121029A	(L)	−0.90	14.91	15.81	⋯	⋯	⋯	119.0	1926.5	1810 ± 70
121123B	(L)	2.3	44.80	42.50	⋯	⋯	⋯	268.0	1651.3	1400 ± 200
121225B	(L)	9.5	67.97	58.50	16.90	21.11	4.21	⋯	⋯	⋯
130305A	(L)	1.3	26.88	25.60	5.31	22.09	16.78	⋯	⋯	⋯
130310A	(L)	4.1	20.10	16.00	4.13	4.21	0.08	67.2	560.1	490 ± 30
130325A	(L)	0.77	7.68	6.91	⋯	⋯	⋯	324.1	1029.7	700 ± 200
130327B	(L)	2.0	33.28	31.23	⋯	⋯	⋯	8.0	523.2	520 ± 10
130427A	(L)	4.1	142.34	138.24	−0.12	46.19	46.30	0.1	34366.2	34400 ± 300
130502B	(L)	7.2	31.49	24.32	13.80	15.37	1.56	12.4	1316.6	1300 ± 200
130504C	(L)	8.7	81.92	73.22	13.54	70.90	57.36	42.6	590.3	550 ± 20
130518A	(L)	9.9	58.50	48.58	23.00	37.71	14.72	26.8	343.6	320 ± 10
130606B	(L)	5.4	57.60	52.23	⋯	⋯	⋯	130.5	527.3	400 ± 40
130702A	(L)	0.77	59.65	58.88	⋯	⋯	⋯	272.3	1283.3	1000 ± 100
130821A	(L)	3.6	90.62	87.04	24.79	34.07	9.28	33.9	6103.7	6000 ± 2000
130828A	(L)	13	150.27	136.96	35.08	68.78	33.70	17.1	616.8	600 ± 10
130907A	(L)	*	210.00	210.00	⋯	⋯	⋯	3618.4	4010.9	400 ± 300
131014A	(L)	0.96	4.16	3.20	1.68	3.49	1.81	1.9	200.4	199 ± 5
131029A	(L)	1.0	105.47	104.45	⋯	⋯	⋯	38.7	557.2	520 ± 50
131108A	(L)	0.32	18.50	18.18	0.04	10.99	10.96	0.0	678.1	680 ± 40
131209A	(L)	2.8	16.38	13.57	⋯	⋯	⋯	14.3	374.8	360 ± 60
131216A	(L)	0.003	19.27	19.26	−0.19	0.09	0.28	⋯	⋯	⋯
131231A	(L)	13	44.54	31.23	21.45	34.25	12.80	23.1	4824.2	4800 ± 700
140102A	(L)	0.45	4.10	3.65	2.38	5.25	2.87	3.1	60.2	60 ± 10
140104B	(L)	11	198.15	187.14	⋯	⋯	⋯	227.3	1174.0	900 ± 200
140110A	(L)	−0.26	9.22	9.47	0.15	6.13	5.98	0.6	159.4	159 ± 8
140124A	(L)	−13	108.87	121.54	⋯	⋯	⋯	93.6	468.2	370 ± 90
140206B	(L)	7.5	154.18	146.69	5.88	33.48	27.60	0.6	8585.0	8584.43 ± 0.01
140219A	(L)	−2.6	74.50	77.06	⋯	⋯	⋯	959.8	1802.0	840 ± 50
140323A	(L)	5.1	116.48	111.43	⋯	⋯	⋯	226.8	715.6	500 ± 100
140402A	(S)	−0.13	0.19	0.32	−0.31	1.24	1.55	0.1	71.7	72 ± 5
140416A	(L)	−2.8	28.96	31.74	⋯	⋯	⋯	1174.8	2207.4	1000 ± 300
140523A	(L)	0.58	19.78	19.20	⋯	⋯	⋯	1.6	470.2	470 ± 20
140528A	(L)	1.0	14.59	13.57	⋯	⋯	⋯	81.1	1377.9	1300 ± 300
140619B	(L)	−0.26	2.56	2.82	0.17	1.30	1.12	0.2	5.3	5 ± 1
140723A	(L)	*	56.32	56.32	−0.31	20.51	20.82	0.6	103.8	103 ± 1
140729A	(L)	0.51	56.06	55.55	⋯	⋯	⋯	4.8	73.4	68.6 ± 0.4
140810A	(L)	6.7	88.32	81.67	⋯	⋯	⋯	460.8	18827.5	18400 ± 100
140825A	(L)	*	14.00	14.00	⋯	⋯	⋯	1463.0	1702.3	200 ± 100
140928A	(L)	−11	7.17	17.92	⋯	⋯	⋯	1676.6	2554.7	880 ± 40
141012A	(L)	−26	11.78	37.63	⋯	⋯	⋯	3.1	107.0	100 ± 10
141028A	(L)	6.7	38.15	31.49	6.86	30.75	23.89	10.9	500.5	490 ± 80
141102A	(L)	−0.064	2.56	2.62	⋯	⋯	⋯	3.5	57.7	54 ± 1
141113A	(S)	−0.064	0.38	0.45	⋯	⋯	⋯	0.1	3.5	3.4 ± 0.1
141207A	(L)	1.3	22.27	20.99	1.69	12.17	10.48	1.8	734.3	730 ± 10
141221B	(L)	−1.3	31.23	32.51	⋯	⋯	⋯	22.2	58.5	36 ± 7
141222A	(L)	*	2.75	2.75	−0.03	1.26	1.29	34.2	440.6	410 ± 10
150118B	(L)	7.7	47.87	40.19	22.12	23.59	1.47	4.3	51.0	50 ± 20
150202B	(L)	1.5	168.96	167.43	4.86	17.51	12.65	44.9	115.7	70 ± 50
150210A	(L)	0.003	31.30	31.29	0.03	2.55	2.52	0.8	169.4	170 ± 20
150314A	(L)	0.61	11.30	10.69	−0.17	0.03	0.20	0.1	3064.3	3100 ± 100
150403A	(L)	3.3	25.60	22.27	9.97	14.08	4.11	399.5	970.5	600 ± 200
150416A	(L)	0.51	33.79	33.28	−3.28	19.07	22.36	⋯	⋯	⋯
150510A	(L)	0.38	52.29	51.90	0.03	16.41	16.38	2.4	172.5	170 ± 10
150513A	(L)	−160	1.79	158.98	−157.75	−146.39	11.36	⋯	⋯	⋯

Table 3
(Continued)

GRB Name	Class	$T_{\rm GBM,05}$ (s)	$T_{\rm GBM,95}$ (s)	$T_{\rm GBM,90}$ (s)	$T_{\rm LLE,05}$ (s)	$T_{\rm LLE,95}$ (s)	$T_{\rm LLE,90}$ (s)	$T_{\rm LAT,0}$ (s)	$T_{\rm LAT,1}$ (s)	$T_{\rm LAT,100}$ (s)
150514A	(L)	0.003	10.82	10.81	⋯	⋯	⋯	442.4	597.6	200 ± 200
150523A	(L)	1.8	84.22	82.43	2.92	43.39	40.48	3.9	6129.1	6130 ± 80
150627A	(L)	5.3	69.89	64.58	4.51	18.09	13.58	152.0	6143.0	6000 ± 1000
150702A	(L)	1.3	47.17	45.83	⋯	⋯	⋯	512.6	1853.3	1340 ± 20
150820A	(L)	−0.77	5.12	5.89	−1.06	−0.64	0.42	⋯	⋯	⋯
150902A	(L)	3.8	17.41	13.57	3.02	12.61	9.60	3.5	408.7	405 ± 2
151006A	(L)	1.5	94.98	93.44	−1.12	15.02	16.14	⋯	⋯	⋯
160101B	(L)	0.003	22.02	22.01	−1.26	3.50	4.76	⋯	⋯	⋯
160310A	(L)	−0.26	25.60	25.86	⋯	⋯	⋯	99.2	432.2	300 ± 200
160314B	(L)	−3.8	94.72	98.56	⋯	⋯	⋯	133.4	1285.4	1200 ± 200
160325A	(L)	2.0	44.99	42.95	13.82	14.02	0.20	5.0	1555.7	1600 ± 500
160422A	(L)	0.83	13.12	12.29	⋯	⋯	⋯	769.6	1061.4	300 ± 300
160503A	(L)	−2.6	26.11	28.67	⋯	⋯	⋯	5324.7	23075.4	17750 ± 70
160509A	(L)	8.2	377.86	369.67	8.81	25.12	16.31	9.6	5687.4	6000 ± 1000
160521B	(L)	0.32	3.14	2.82	⋯	⋯	⋯	90.2	2199.4	2100 ± 300
160623A	(L)	−1.3	106.50	107.78	⋯	⋯	⋯	401.5	35069.0	35000 ± 1000
160625B	(L)	190	641.84	453.38	184.86	220.27	35.41	25.6	840.5	810 ± 20
160702A	(S)	*	0.20	0.20	⋯	⋯	⋯	1941.5	2215.6	300 ± 100
160709A	(L)	*	5.44	5.44	0.41	3.62	3.21	0.5	25.8	25 ± 2
160816A	(L)	0.38	11.46	11.07	0.45	10.91	10.46	1.1	1094.8	1090 ± 70
160821A	(L)	120	161.54	43.01	117.29	152.21	34.92	92.1	1459.2	1370 ± 40
160829A	(S)	−0.064	0.45	0.51	⋯	⋯	⋯	0.9	31.7	31 ± 6
160905A	(L)	3.8	37.38	33.54	5.57	28.92	23.34	7.8	463.3	460 ± 20
160910A	(L)	4.6	28.93	24.32	7.70	18.47	10.78	86.4	216.4	130 ± 50
160917B	(L)	−4.6	9.98	14.59	−0.90	5.55	6.45	⋯	⋯	⋯
160917A	(L)	−0.26	19.20	19.46	−0.12	0.33	0.44	⋯	⋯	⋯
161015A	(L)	0.26	15.36	15.10	⋯	⋯	⋯	1.1	7.5	6.4 ± 0.2
161109A	(L)	3.8	27.39	23.55	⋯	⋯	⋯	423.4	890.9	500 ± 200
170115B	(L)	0.51	44.80	44.29	0.55	11.58	11.03	1.3	1027.9	1027 ± 10
170127C	(S)	*	0.13	0.13	⋯	⋯	⋯	664.8	2889.0	2220 ± 50
170214A	(L)	13	135.43	122.88	6.54	84.10	77.56	39.5	752.0	713 ± 8
170228A	(L)	1.6	62.24	60.67	⋯	⋯	⋯	6.5	72.4	70 ± 10
170306B	(L)	4.6	23.55	18.94	⋯	⋯	⋯	21.2	71.5	50 ± 10
170329A	(L)	0.26	33.79	33.54	⋯	⋯	⋯	3.9	52.4	48 ± 7
170405A	(L)	7.4	86.02	78.59	16.56	51.51	34.95	17.8	868.0	850 ± 60
170409A	(L)	29	93.44	64.00	⋯	⋯	⋯	178.4	440.3	260 ± 30
170424A	(L)	2.8	56.06	53.25	2.42	37.62	35.19	21.8	107.7	86 ± 2
170510A	(L)	2.8	130.56	127.75	−1.03	27.68	28.71	26.8	154.2	127 ± 5
170522A	(L)	0.58	8.00	7.42	⋯	⋯	⋯	2.8	41.6	40 ± 10
170728B	(L)	*	46.34	46.34	−0.01	0.40	0.41	0.2	469.3	469.070 ± 0.010
170808B	(L)	4.1	21.76	17.66	6.47	16.77	10.31	13.7	6205.9	6190 ± 40
170813A	(L)	−0.51	111.36	111.87	⋯	⋯	⋯	9.5	265.3	260 ± 70
170825B	(L)	−0.51	6.14	6.66	⋯	⋯	⋯	0.9	1.5	0.6 ± 0.3
170906A	(L)	12	90.88	78.85	⋯	⋯	⋯	162.1	1983.2	1821 ± 3
170921B	(L)	1.0	40.38	39.36	⋯	⋯	⋯	901.7	1058.6	200 ± 200
171010A	(L)	17	123.91	107.27	⋯	⋯	⋯	335.6	2984.8	2650 ± 50
171011C	(S)	−0.45	0.03	0.48	⋯	⋯	⋯	0.1	42.7	40 ± 20
171102A	(L)	7.7	56.06	48.38	⋯	⋯	⋯	34.9	401.0	366 ± 10
171120A	(L)	0.003	44.06	44.06	⋯	⋯	⋯	0.3	5276.0	5280 ± 10
171124A	(L)	−0.70	25.47	26.18	⋯	⋯	⋯	3.4	321.3	318 ± 7
171210A	(L)	3.6	146.69	143.11	−1.19	7.01	8.20	5.9	1518.1	1510 ± 70
171212B	(L)	−1.0	30.98	32.00	⋯	⋯	⋯	116.6	497.0	400 ± 100
180113C	(L)	5.4	29.95	24.58	5.85	29.54	23.69	⋯	⋯	⋯
180210A	(L)	4.1	43.01	38.91	⋯	⋯	⋯	23.1	1621.1	1600 ± 200
180305A	(L)	1.5	14.59	13.06	2.48	5.38	2.89	1613.8	2038.0	400 ± 400
180526A	(L)	*	87.00	87.00	⋯	⋯	⋯	808.9	1948.6	1140 ± 50
180703A	(L)	1.5	22.27	20.74	0.93	8.05	7.12	3.8	1614.0	1610 ± 80
180703B	(S)	0.13	1.66	1.54	⋯	⋯	⋯	8.0	78.5	70 ± 20
180718B	(L)	1.6	99.91	98.31	⋯	⋯	⋯	1.1	16.2	15 ± 3
180720B	(L)	4.4	53.25	48.90	0.91	31.47	30.55	11.8	625.0	613 ± 9

Table 4
Likelihood Analysis

GRB Name	Interval ($t_0 - t_1$) (s)	Trans. Ev. in the ROI	Trans. Ev. Predicted	Test Statistic (TS)	Spectral Index	Flux ($\times 10^{-5}$ cm^{-2} s^{-1})	Fluence ($\times 10^{-5}$ erg cm^{-2})	$E_{\rm iso}$ (100 MeV–10 GeV) ($\times 10^{52}$ erg)
080818B	LTF (0.0–10000.0)	65	5.0	23	-1.8 ± 0.4	0.08 ± 0.05	2 ± 2	⋯
080825C	GBM (1.2–22.2)	11	9.6	51	-3.8 ± 0.8	21 ± 7	0.11 ± 0.04	⋯
	LTF (0.0–100.0)	23	18.8	87	-3.0 ± 0.4	8 ± 2	0.26 ± 0.08	⋯
	EXT (22.2–173.5)	14	10.1	23	-2.4 ± 0.4	3 ± 1	0.2 ± 0.1	⋯
	LAT (3.1–173.5)	25	19.8	86	-2.8 ± 0.4	5 ± 1	0.29 ± 0.10	⋯
080916C	GBM (1.3–64.3)	255	246.8	2344	-2.22 ± 0.07	91 ± 6	4.0 ± 0.6	170 ± 10
	LTF (0.0–100.0)	290	277.7	2546	-2.21 ± 0.07	64 ± 4	4.5 ± 0.7	190 ± 10
	EXT (64.3–1531.8)	186	106.0	352	-2.2 ± 0.1	1.6 ± 0.2	1.8 ± 0.4	68 ± 9
	LAT (3.0–1531.8)	440	349.2	2173	-2.20 ± 0.06	5.1 ± 0.3	5.6 ± 0.8	230 ± 10
081006	GBM (-0.3–6.1)	8	8.0	97	-2.2 ± 0.4	21 ± 7	0.10 ± 0.07	⋯
	LTF (0.0–10000.0)	46	15.9	74	-2.1 ± 0.3	1.6 ± 0.5	14 ± 8	⋯
	EXT (6.1–62.3)	9	5.6	36	-1.9 ± 0.4	1.6 ± 0.7	0.1 ± 0.1	⋯
	LAT (0.8–62.3)	16	12.7	112	-2.0 ± 0.3	3.3 ± 1.0	0.2 ± 0.1	⋯
081009	LTF (0.0–4000.0)	67	14.6	49	-1.7 ± 0.2	0.20 ± 0.07	2 ± 1	⋯
	EXT (42.7–1250.1)	45	14.7	49	-1.8 ± 0.2	0.3 ± 0.1	0.8 ± 0.5	⋯
	LAT (67.8–1250.1)	44	13.6	46	-1.8 ± 0.2	0.3 ± 0.1	0.8 ± 0.5	⋯
081024B	GBM (-0.1–0.6)	6	6.0	76	-2.3 ± 0.5	140 ± 60	0.06 ± 0.05	⋯
	LTF (0.0–10.0)	14	13.9	152	-2.3 ± 0.3	21 ± 6	0.13 ± 0.07	⋯
	EXT (0.6–2.2)	6	6.0	75	-2.3 ± 0.5	60 ± 20	0.05 ± 0.04	⋯
	LAT (0.2–2.2)	11	11.0	138	-2.2 ± 0.4	80 ± 30	0.11 ± 0.08	⋯
081102B	GBM (-0.1–1.7)	6	6.0	70	-2.2 ± 0.5	80 ± 30	0.10 ± 0.09	⋯
	LTF (0.0–10.0)	6	5.8	50	-2.2 ± 0.5	14 ± 6	0.09 ± 0.09	⋯
	LAT (0.3–0.4)	5	5.0	88	-2.5 ± 0.6	800 ± 400	0.06 ± 0.04	⋯
081122A	LTF (0.0–100.0)	6	5.4	37	-1.8 ± 0.4	0.8 ± 0.3	0.2 ± 0.2	⋯
081203A	LTF (0.0–500.0)	7	6.0	34	-2.1 ± 0.4	0.3 ± 0.1	0.10 ± 0.10	1.0 ± 0.4
	EXT (214.0–348.1)	4	3.9	22	-2.4 ± 0.6	0.5 ± 0.3	0.04 ± 0.04	0.6 ± 0.3
081224	LTF (0.0–500.0)	21	6.1	27	-1.8 ± 0.3	0.19 ± 0.09	0.2 ± 0.2	⋯
090217	GBM (0.8–34.1)	22	21.1	177	-2.3 ± 0.3	11 ± 2	0.21 ± 0.09	⋯
	LTF (0.0–100.0)	30	25.5	162	-2.3 ± 0.2	4.5 ± 1.0	0.3 ± 0.1	⋯
	LAT (4.1–71.6)	27	23.6	156	-2.3 ± 0.3	6 ± 1	0.2 ± 0.1	⋯
090227A	LTF (0.0–500.0)	16	7.7	33	-2.0 ± 0.4	0.3 ± 0.1	0.1 ± 0.1	⋯
	LAT (2.9–204.3)	5	3.8	30	-1.7 ± 0.4	0.3 ± 0.2	0.1 ± 0.2	⋯
090227B	GBM (-0.0–0.3)	2	2.0	23	-6.00 ± 0.01	2000 ± 1000	0.10 ± 0.07	⋯
	LTF (0.0–1.2)	3	3.0	30	-5 ± 2	600 ± 300	0.15 ± 0.10	⋯
090228A	LTF (0.0–10.0)	6	5.8	60	-1.8 ± 0.3	9 ± 4	0.2 ± 0.2	⋯
	EXT (0.4–2.1)	4	3.9	39	-1.9 ± 0.5	40 ± 20	0.1 ± 0.1	⋯
	LAT (0.1–2.1)	4	4.0	38	-1.9 ± 0.5	30 ± 20	0.1 ± 0.1	⋯
090323	GBM (8.7–142.6)	23	19.2	89	-3.0 ± 0.4	6 ± 2	0.26 ± 0.07	30 ± 20
	LTF (0.0–4000.0)	73	63.8	392	-2.4 ± 0.2	2.8 ± 0.4	6 ± 2	260 ± 50
	EXT (142.6–5321.6)	80	49.8	169	-2.2 ± 0.2	0.8 ± 0.1	3 ± 1	90 ± 20
	LAT (9.3–5321.6)	102	67.2	206	-2.3 ± 0.2	1.0 ± 0.1	3.4 ± 0.9	120 ± 20
090328	GBM (4.4–66.0)	12	11.8	102	-3.0 ± 0.5	14 ± 4	0.27 ± 0.09	0.7 ± 0.2
	LTF (0.0–4000.0)	170	87.8	288	-2.2 ± 0.1	0.62 ± 0.08	1.7 ± 0.4	2.3 ± 0.3
	EXT (66.0–6150.6)	188	78.7	255	-2.2 ± 0.1	0.42 ± 0.06	1.9 ± 0.6	2.4 ± 0.5
	LAT (14.4–6150.6)	199	86.5	275	-2.2 ± 0.1	0.46 ± 0.06	2.0 ± 0.5	2.7 ± 0.4
090427A	LTF (0.0–500.0)	10	3.7	40	-1.3 ± 0.3	0.5 ± 0.3	2 ± 2	⋯
	EXT (15.0–435.6)	5	1.1	24	-0.8 ± 0.7	0.2 ± 0.2	4 ± 5	⋯
090510	GBM (-0.0–0.9)	64	64.0	1285	-1.8 ± 0.1	900 ± 100	1.7 ± 0.6	1.7 ± 0.3
	LTF (0.0–10.0)	221	220.8	3618	-1.99 ± 0.07	310 ± 20	3.5 ± 0.6	5.1 ± 0.4
	EXT (0.9–170.0)	205	197.8	1869	-2.15 ± 0.08	17 ± 1	2.2 ± 0.4	4.2 ± 0.4
	LAT (0.0–170.0)	267	262.2	2924	-2.05 ± 0.06	22 ± 1	3.6 ± 0.6	5.8 ± 0.5

Table 4
(Continued)

GRB Name	Interval ($t_0 - t_1$) (s)	Trans. Ev. in the ROI	Trans. Ev. Predicted	Test Statistic (TS)	Spectral Index	Flux ($\times 10^{-5}$ cm^{-2} s^{-1})	Fluence ($\times 10^{-5}$ erg cm^{-2})	$E_{\rm iso}$ (100 MeV–10 GeV) ($\times 10^{52}$ erg)
090626	LTF (0.0–4000.0)	51	31.2	120	-2.1 ± 0.2	1.0 ± 0.2	4 ± 1	⋯
	EXT (50.4–557.3)	38	23.5	102	-2.0 ± 0.2	1.1 ± 0.3	0.6 ± 0.3	⋯
	LAT (9.0–557.3)	41	25.1	101	-2.1 ± 0.2	1.1 ± 0.3	0.6 ± 0.3	⋯
090720B	GBM (−0.3–10.5)	7	6.5	50	-2.5 ± 0.6	20 ± 8	0.10 ± 0.07	⋯
	LTF (0.0–10.0)	7	6.5	51	-2.5 ± 0.6	21 ± 9	0.10 ± 0.07	⋯
	LAT (0.1–1.7)	5	4.9	51	-2.3 ± 0.5	100 ± 50	0.1 ± 0.1	⋯
090902B	GBM (2.8–22.1)	245	244.6	3795	-1.99 ± 0.06	310 ± 20	7 ± 1	37 ± 3
	LTF (0.0–100.0)	392	389.1	5006	-1.94 ± 0.05	84 ± 4	11 ± 2	54 ± 3
	EXT (22.1–884.2)	298	246.0	1723	-1.92 ± 0.06	4.1 ± 0.3	4.9 ± 0.9	23 ± 2
	LAT (0.5–884.2)	548	500.5	4089	-1.94 ± 0.04	8.3 ± 0.4	9 ± 1	47 ± 2
090926A	GBM (2.2–15.9)	252	251.9	3806	-2.52 ± 0.09	450 ± 30	2.9 ± 0.3	53 ± 4
	LTF (0.0–100.0)	386	383.3	4509	-2.26 ± 0.06	95 ± 5	6.2 ± 0.7	76 ± 4
	EXT (15.9–4419.5)	225	166.9	707	-1.86 ± 0.07	1.6 ± 0.1	12 ± 2	60 ± 5
	LAT (2.2–4419.5)	477	417.0	2652	-2.14 ± 0.05	4.2 ± 0.2	15 ± 2	149 ± 8
091003	GBM (0.8–21.1)	6	5.2	63	-1.8 ± 0.4	4 ± 2	0.2 ± 0.2	0.16 ± 0.08
	LTF (0.0–500.0)	47	29.4	171	-1.8 ± 0.2	0.9 ± 0.2	0.8 ± 0.4	0.9 ± 0.2
	EXT (21.1–392.0)	37	23.8	134	-1.8 ± 0.2	1.0 ± 0.2	0.7 ± 0.4	0.7 ± 0.2
	LAT (1.0–392.0)	42	28.0	174	-1.8 ± 0.2	1.2 ± 0.2	0.8 ± 0.4	0.8 ± 0.2
091031	GBM (1.4–35.3)	13	10.7	67	-2.7 ± 0.5	5 ± 2	0.07 ± 0.03	⋯
	LTF (0.0–100.0)	30	24.5	166	-2.2 ± 0.2	4.0 ± 0.9	0.3 ± 0.1	⋯
	EXT (35.3–408.2)	30	14.4	80	-1.8 ± 0.2	0.6 ± 0.2	0.4 ± 0.3	⋯
	LAT (0.1–408.2)	47	26.0	110	-2.1 ± 0.2	1.0 ± 0.2	0.4 ± 0.2	⋯
091120	LTF (0.0–4000.0)	67	22.0	45	-2.8 ± 0.4	0.4 ± 0.1	0.5 ± 0.2	⋯
	EXT (51.2–803.9)	40	16.9	37	-2.7 ± 0.4	0.5 ± 0.1	0.13 ± 0.05	⋯
	LAT (31.8–803.9)	41	17.6	37	-2.8 ± 0.4	0.5 ± 0.2	0.14 ± 0.05	⋯
091127	LTF (0.0–500.0)	14	6.2	34	-1.7 ± 0.3	0.19 ± 0.09	0.3 ± 0.3	0.06 ± 0.03
	LAT (8.6–35.4)	3	2.1	32	-1.2 ± 0.4	1.2 ± 0.9	0.4 ± 0.5	0.03 ± 0.02
100116A	GBM (0.6–103.1)	12	8.5	28	-3.2 ± 0.7	1.7 ± 0.6	0.05 ± 0.02	⋯
	LTF (0.0–4000.0)	67	25.7	129	-1.8 ± 0.2	0.7 ± 0.2	5 ± 2	⋯
	EXT (103.1–730.4)	52	16.5	103	-1.6 ± 0.2	0.5 ± 0.2	1.3 ± 0.7	⋯
	LAT (77.5–730.4)	60	23.6	122	-1.8 ± 0.2	0.8 ± 0.2	1.0 ± 0.5	⋯
100213C	LTF (0.0–4000.0)	181	9.8	42	-1.7 ± 0.3	0.16 ± 0.08	2 ± 1	⋯
	EXT (60.0–3215.3)	82	7.4	22	-2.0 ± 0.4	0.3 ± 0.2	1.0 ± 0.8	⋯
	LAT (2707.2–3215.3)	59	5.6	21	-1.9 ± 0.4	0.3 ± 0.2	0.3 ± 0.3	⋯
100225A	GBM (−0.3–12.7)	7	6.8	47	-3.7 ± 1.0	18 ± 7	0.06 ± 0.02	⋯
	LTF (0.0–100.0)	13	10.1	46	-2.3 ± 0.4	3 ± 1	0.2 ± 0.1	⋯
	EXT (12.7–1012.4)	36	7.2	27	-1.8 ± 0.4	0.13 ± 0.07	0.2 ± 0.2	⋯
	LAT (6.6–1012.4)	43	12.1	32	-2.2 ± 0.4	0.22 ± 0.09	0.2 ± 0.1	⋯
100325A	GBM (−0.4–6.7)	6	6.0	58	-2.1 ± 0.4	12 ± 5	0.07 ± 0.07	⋯
	LTF (0.0–10.0)	6	5.9	55	-2.1 ± 0.4	8 ± 4	0.07 ± 0.07	⋯
	LAT (0.2–1.2)	5	5.0	68	-1.9 ± 0.4	70 ± 30	0.1 ± 0.1	⋯
100414A	GBM (1.9–28.4)	5	4.7	35	-2.3 ± 0.5	20 ± 10	0.4 ± 0.3	2.1 ± 1.0
	LTF (0.0–4000.0)	97	48.8	211	-1.8 ± 0.1	0.43 ± 0.07	3 ± 1	7 ± 1
	EXT (28.4–5506.1)	121	50.2	210	-1.8 ± 0.1	0.30 ± 0.05	3 ± 1	7 ± 1
	LAT (18.7–5506.1)	125	52.6	216	-1.8 ± 0.1	0.31 ± 0.05	3 ± 1	7 ± 1
100423B	LTF (0.0–500.0)	19	9.0	31	-2.0 ± 0.4	0.4 ± 0.2	0.2 ± 0.2	⋯
	EXT (18.1–180.6)	11	5.8	28	-1.9 ± 0.5	0.8 ± 0.5	0.2 ± 0.2	⋯
	LAT (166.7–180.6)	2	2.0	23	-1.8 ± 0.6	3 ± 2	0.1 ± 0.1	⋯
100511A	LTF (0.0–500.0)	44	18.5	114	-1.5 ± 0.2	0.6 ± 0.2	1.5 ± 1.0	⋯
	EXT (43.3–6338.2)	175	30.4	89	-1.8 ± 0.2	0.18 ± 0.05	2 ± 1	⋯
	LAT (11.6–6338.2)	178	33.0	93	-1.8 ± 0.2	0.19 ± 0.05	2 ± 1	⋯
100620A	GBM (0.2–52.0)	6	5.8	28	-4 ± 1	1.8 ± 0.8	0.02 ± 0.01	⋯

Table 4
(Continued)

GRB Name	Interval ($t_0 - t_1$) (s)	Trans. Ev. in the ROI	Trans. Ev. Predicted	Test Statistic (TS)	Spectral Index	Flux ($\times 10^{-5}$ cm^{-2} s^{-1})	Fluence ($\times 10^{-5}$ erg cm^{-2})	$E_{\rm iso}$ (100 MeV–10 GeV) ($\times 10^{52}$ erg)
	LTF (0.0–100.0)	8	6.4	26	-3.5 ± 0.9	1.0 ± 0.4	0.03 ± 0.01	⋯
	LAT (3.8–42.8)	4	3.8	21	-4 ± 2	1.6 ± 0.9	0.015 ± 0.009	⋯
100724B	GBM (8.2–122.9)	9	8.5	53	-5 ± 1	7 ± 3	0.19 ± 0.07	⋯
	LTF (0.0–4000.0)	35	17.0	23	-3.7 ± 0.6	0.22 ± 0.07	0.22 ± 0.07	⋯
	LAT (9.1–53.6)	9	8.7	65	-4 ± 1	8 ± 3	0.08 ± 0.03	⋯
100728A	LTF (0.0–4000.0)	107	16.1	64	-1.7 ± 0.2	0.13 ± 0.04	1.3 ± 0.8	2.8 ± 0.8
	EXT (178.7–1340.5)	62	12.8	64	-1.7 ± 0.2	0.17 ± 0.06	0.6 ± 0.4	1.1 ± 0.4
	LAT (248.6–1340.5)	60	10.7	54	-1.6 ± 0.2	0.15 ± 0.06	0.5 ± 0.4	0.9 ± 0.3
100826A	GBM (8.7–93.7)	7	5.8	34	-1.6 ± 0.4	14 ± 7	4 ± 5	⋯
	LTF (0.0–100.0)	7	5.7	32	-1.6 ± 0.4	11 ± 6	4 ± 5	⋯
	LAT (33.5–54.5)	4	3.8	23	-2.3 ± 0.6	40 ± 20	0.5 ± 0.4	⋯
101014A	LTF (0.0–10000.0)	103	6.8	48	-1.4 ± 0.3	0.019 ± 0.010	2 ± 1	⋯
	EXT (450.8–4196.0)	42	5.3	46	-1.3 ± 0.3	0.04 ± 0.02	1 ± 1	⋯
	LAT (2270.7–4196.0)	40	5.2	47	-1.3 ± 0.3	0.04 ± 0.02	0.7 ± 0.8	⋯
101107A	GBM (2.3–378.1)	13	8.2	49	-1.9 ± 0.3	0.4 ± 0.2	0.2 ± 0.2	⋯
	LTF (0.0–500.0)	17	10.6	55	-2.1 ± 0.3	0.4 ± 0.1	0.2 ± 0.1	⋯
	LAT (134.0–239.4)	9	8.2	56	-1.9 ± 0.3	1.4 ± 0.6	0.2 ± 0.2	⋯
101227B	GBM (0.8–154.1)	14	5.0	24	-1.6 ± 0.3	0.4 ± 0.2	0.2 ± 0.3	⋯
	LTF (0.0–100.0)	9	4.2	27	-1.5 ± 0.3	0.6 ± 0.3	0.3 ± 0.3	⋯
	LAT (17.3–23.8)	3	2.1	25	-1.5 ± 0.5	4 ± 3	0.1 ± 0.2	⋯
110120A	LTF (0.0–4000.0)	62	19.2	70	-2.0 ± 0.2	0.18 ± 0.05	0.7 ± 0.4	⋯
	EXT (26.2–1112.8)	28	14.3	63	-2.0 ± 0.3	0.21 ± 0.06	0.3 ± 0.2	⋯
	LAT (0.6–1112.8)	31	16.8	74	-2.0 ± 0.3	0.24 ± 0.07	0.3 ± 0.2	⋯
110123A	LTF (0.0–10000.0)	190	20.7	46	-2.1 ± 0.3	0.06 ± 0.02	0.5 ± 0.3	⋯
	EXT (18.6–526.2)	28	11.3	38	-2.3 ± 0.4	0.4 ± 0.1	0.12 ± 0.07	⋯
	LAT (51.6–526.2)	23	7.9	27	-2.2 ± 0.4	0.3 ± 0.1	0.10 ± 0.08	⋯
110213A	LTF (0.0–10000.0)	207	8.8	28	-1.6 ± 0.3	0.05 ± 0.03	2 ± 2	3 ± 1
	EXT (33.5–1944.2)	37	3.3	21	-1.5 ± 0.4	0.11 ± 0.07	1 ± 1	1.1 ± 0.7
110328B	LTF (0.0–10000.0)	41	15.7	50	-2.2 ± 0.3	0.15 ± 0.05	1.1 ± 0.6	⋯
	EXT (86.5–737.2)	17	11.1	55	-2.0 ± 0.3	0.3 ± 0.1	0.2 ± 0.2	⋯
	LAT (102.5–737.2)	17	11.1	55	-2.0 ± 0.3	0.3 ± 0.1	0.2 ± 0.2	⋯
110428A	LTF (0.0–500.0)	71	22.4	63	-2.0 ± 0.2	0.7 ± 0.2	0.4 ± 0.2	⋯
	EXT (8.3–393.5)	51	17.0	52	-1.9 ± 0.3	0.7 ± 0.2	0.4 ± 0.2	⋯
	LAT (7.3–393.5)	52	18.1	55	-1.9 ± 0.2	0.8 ± 0.2	0.4 ± 0.2	⋯
110518A	LTF (0.0–4000.0)	51	10.4	42	-1.9 ± 0.3	0.09 ± 0.04	0.6 ± 0.5	⋯
	EXT (35.0–2364.2)	36	8.4	31	-1.9 ± 0.4	0.13 ± 0.06	0.4 ± 0.4	⋯
	LAT (1968.2–2364.2)	16	3.5	21	-1.8 ± 0.5	0.14 ± 0.10	0.1 ± 0.1	⋯
110625A	LTF (0.0–4000.0)	177	57.3	88	-3 ± 3	2 ± 6	3.9 ± 0.8	⋯
	EXT (30.7–577.2)	94	39.2	73	-2.7 ± 0.3	3.1 ± 0.6	0.7 ± 0.2	⋯
	LAT (205.9–577.2)	86	36.6	67	-2.7 ± 0.3	3.1 ± 0.6	0.4 ± 0.1	⋯
110721A	GBM (0.0–21.8)	34	33.6	355	-2.6 ± 0.3	30 ± 5	0.28 ± 0.09	⋯
	LTF (0.0–10.0)	30	29.8	349	-2.7 ± 0.3	60 ± 10	0.23 ± 0.07	⋯
	EXT (21.8–120.6)	8	7.4	31	-2.1 ± 0.4	1.3 ± 0.5	0.10 ± 0.09	⋯
	LAT (0.0–120.6)	41	40.2	387	-2.4 ± 0.2	5.8 ± 0.9	0.4 ± 0.1	⋯
110728A	LTF (0.0–10.0)	8	7.7	73	-1.8 ± 0.3	14 ± 5	0.2 ± 0.2	⋯
	EXT (0.6–3.0)	5	4.9	39	-1.9 ± 0.4	40 ± 20	0.1 ± 0.1	⋯
	LAT (0.4–3.0)	6	5.9	57	-1.9 ± 0.4	40 ± 20	0.2 ± 0.2	⋯

Table 4
(Continued)

GRB Name	Interval ($t_0 - t_1$) (s)	Trans. Ev. in the ROI	Trans. Ev. Predicted	Test Statistic (TS)	Spectral Index	Flux ($\times 10^{-5}$ cm^{-2} s^{-1})	Fluence ($\times 10^{-5}$ erg cm^{-2})	$E_{\rm iso}$ (100 MeV–10 GeV) ($\times 10^{52}$ erg)
110731A	GBM (0.0–7.5)	50	49.4	469	-2.6 ± 0.2	100 ± 10	0.30 ± 0.07	12 ± 3
	LTF (0.0–10.0)	59	58.2	558	-2.4 ± 0.2	80 ± 10	0.4 ± 0.1	13 ± 2
	EXT (7.5–436.0)	111	28.4	89	-2.0 ± 0.2	0.9 ± 0.2	0.4 ± 0.2	5 ± 1
	LAT (1.1–436.0)	160	70.6	191	-2.3 ± 0.2	2.4 ± 0.3	0.6 ± 0.2	15 ± 2
110903A	GBM (-0.3–341.0)	11	5.5	45	-1.5 ± 0.3	0.4 ± 0.2	0.6 ± 0.6	⋯
	LTF (0.0–500.0)	14	7.2	49	-1.6 ± 0.3	0.3 ± 0.2	0.6 ± 0.5	⋯
	LAT (46.7–370.1)	12	5.6	48	-1.4 ± 0.3	0.4 ± 0.2	0.7 ± 0.7	⋯
110921B	GBM (0.9–18.6)	6	5.0	43	-2.0 ± 0.4	6 ± 3	0.1 ± 0.1	⋯
	LTF (0.0–500.0)	21	11.9	55	-1.9 ± 0.3	0.4 ± 0.1	0.3 ± 0.2	⋯
	EXT (18.6–321.6)	14	7.4	36	-1.9 ± 0.3	0.4 ± 0.2	0.2 ± 0.2	⋯
	LAT (7.4–321.6)	19	11.0	55	-1.8 ± 0.3	0.6 ± 0.2	0.3 ± 0.2	⋯
111210B	LTF (0.0–10000.0)	22	12.4	35	-3.0 ± 0.5	0.4 ± 0.1	1.3 ± 0.5	⋯
	EXT (60.0–394.0)	14	7.0	22	-2.3 ± 0.5	0.4 ± 0.2	0.09 ± 0.06	⋯
	LAT (6.5–394.0)	18	10.2	30	-2.7 ± 0.5	0.6 ± 0.2	0.09 ± 0.04	⋯
120107A	GBM (0.1–23.1)	8	7.5	53	-2.4 ± 0.5	8 ± 3	0.10 ± 0.07	⋯
	LTF (0.0–10.0)	6	5.7	47	-2.1 ± 0.4	13 ± 6	0.1 ± 0.1	⋯
	LAT (1.3–48.8)	11	7.9	41	-1.9 ± 0.4	4 ± 2	0.2 ± 0.2	⋯
120226A	LTF (0.0–500.0)	84	20.0	43	-2.8 ± 0.4	0.7 ± 0.2	0.13 ± 0.04	⋯
	EXT (57.3–283.6)	47	11.8	30	-2.9 ± 0.6	0.9 ± 0.3	0.07 ± 0.03	⋯
	LAT (29.4–283.6)	52	14.0	37	-2.9 ± 0.5	1.0 ± 0.4	0.08 ± 0.03	⋯
120316A	GBM (1.5–28.2)	4	3.0	25	-1.9 ± 0.5	2 ± 1	0.1 ± 0.1	⋯
	LTF (0.0–500.0)	17	13.1	69	-2.2 ± 0.3	0.5 ± 0.1	0.2 ± 0.1	⋯
	EXT (28.2–545.0)	15	11.2	53	-2.3 ± 0.4	0.4 ± 0.1	0.11 ± 0.07	⋯
	LAT (15.0–545.0)	17	13.2	70	-2.2 ± 0.3	0.4 ± 0.1	0.2 ± 0.1	⋯
120420B	LTF (0.0–4000.0)	51	12.2	32	-2.2 ± 0.3	0.3 ± 0.1	1.0 ± 0.7	⋯
	EXT (254.9–3908.0)	45	10.0	27	-2.1 ± 0.4	0.3 ± 0.1	1.0 ± 0.7	⋯
	LAT (3501.7–3908.0)	28	9.0	28	-2.1 ± 0.4	0.5 ± 0.2	0.2 ± 0.1	⋯
120526A	LTF (0.0–4000.0)	81	32.3	121	-1.9 ± 0.2	0.20 ± 0.04	1.2 ± 0.7	⋯
	EXT (46.7–3306.3)	80	32.5	122	-1.9 ± 0.2	0.21 ± 0.04	1.1 ± 0.6	⋯
	LAT (692.2–3306.3)	78	31.0	121	-1.8 ± 0.2	0.20 ± 0.04	0.9 ± 0.5	⋯
120624B	LTF (0.0–4000.0)	154	124.3	750	-2.5 ± 0.1	2.1 ± 0.2	3.7 ± 0.7	77 ± 8
	EXT (14.3–1103.9)	148	122.9	775	-2.5 ± 0.1	2.3 ± 0.2	1.1 ± 0.2	23 ± 2
	LAT (73.7–1103.9)	148	122.9	774	-2.5 ± 0.1	2.3 ± 0.2	1.1 ± 0.2	22 ± 2
120709A	GBM (-0.1–27.2)	13	12.8	126	-2.2 ± 0.3	8 ± 2	0.2 ± 0.1	⋯
	LTF (0.0–10000.0)	53	33.1	99	-2.3 ± 0.2	1.0 ± 0.2	6 ± 2	⋯
	EXT (27.2–695.9)	36	18.6	38	-2.4 ± 0.3	0.6 ± 0.2	0.22 ± 0.10	⋯
	LAT (0.1–695.9)	48	31.7	92	-2.3 ± 0.2	1.0 ± 0.2	0.4 ± 0.2	⋯
120711A	LTF (0.0–10000.0)	143	44.1	135	-2.1 ± 0.2	0.24 ± 0.05	1.9 ± 0.7	9 ± 2
	EXT (106.5–5431.6)	87	42.5	161	-2.1 ± 0.2	0.53 ± 0.10	2.6 ± 1.0	11 ± 2
	LAT (393.3–5431.6)	86	41.3	158	-2.1 ± 0.2	0.52 ± 0.10	2.5 ± 1.0	10 ± 2
120729A	LTF (0.0–4000.0)	16	6.0	32	-1.7 ± 0.3	0.4 ± 0.2	5 ± 5	3 ± 1
	EXT (24.4–432.0)	5	3.1	31	-1.5 ± 0.4	3 ± 2	6 ± 8	2 ± 1
120830A	GBM (0.0–0.9)	3	3.0	47	-2.1 ± 0.6	60 ± 40	0.05 ± 0.07	⋯
	LTF (0.0–10.0)	5	5.0	64	-1.8 ± 0.4	9 ± 4	0.2 ± 0.2	⋯
	EXT (0.9–10.7)	3	2.9	29	-1.8 ± 0.5	5 ± 3	0.1 ± 0.1	⋯
	LAT (0.7–10.7)	6	6.0	71	-1.9 ± 0.4	11 ± 4	0.1 ± 0.1	⋯
120911B	GBM (0.0–69.0)	50	49.8	549	-2.5 ± 0.2	61 ± 9	1.9 ± 0.4	⋯
	LTF (0.0–100.0)	57	56.7	608	-2.5 ± 0.2	47 ± 7	2.3 ± 0.5	⋯

Table 4
(Continued)

GRB Name	Interval ($t_0 - t_1$) (s)	Trans. Ev. in the ROI	Trans. Ev. Predicted	Test Statistic (TS)	Spectral Index	Flux ($\times 10^{-5}$ cm^{-2} s^{-1})	Fluence ($\times 10^{-5}$ erg cm^{-2})	$E_{\rm iso}$ (100 MeV–10 GeV) ($\times 10^{52}$ erg)
	EXT (69.0–217.8)	16	15.7	128	-2.3 ± 0.3	10 ± 3	0.8 ± 0.4	⋯
	LAT (9.2–217.8)	65	64.5	628	-2.5 ± 0.2	28 ± 4	2.8 ± 0.5	⋯
120915A	GBM (−0.3–0.3)	2	2.0	21	-3 ± 1	50 ± 40	0.010 ± 0.009	⋯
	LTF (0.0–10.0)	4	3.9	31	-2.3 ± 0.6	6 ± 3	0.04 ± 0.04	⋯
120919B	LTF (0.0–4000.0)	30	8.5	29	-2.1 ± 0.4	0.19 ± 0.09	0.7 ± 0.6	⋯
121029A	LTF (0.0–4000.0)	103	10.0	38	-1.6 ± 0.2	0.08 ± 0.03	1.2 ± 0.9	⋯
	EXT (14.9–1926.5)	88	9.4	38	-1.6 ± 0.3	0.08 ± 0.04	0.6 ± 0.5	⋯
	LAT (119.0–1926.5)	82	6.4	23	-1.6 ± 0.3	0.06 ± 0.03	0.4 ± 0.4	⋯
121123B	LTF (0.0–4000.0)	32	10.6	27	-2.3 ± 0.4	0.19 ± 0.08	0.5 ± 0.3	⋯
	EXT (44.8–1651.3)	26	9.9	25	-2.3 ± 0.4	0.23 ± 0.10	0.2 ± 0.1	⋯
	LAT (268.0–1651.3)	24	10.0	26	-2.4 ± 0.4	0.2 ± 0.1	0.2 ± 0.1	⋯
130310A	LTF (0.0–4000.0)	38	15.3	53	-1.9 ± 0.2	0.5 ± 0.1	3 ± 2	⋯
	EXT (20.1–560.1)	26	15.3	54	-2.1 ± 0.3	0.7 ± 0.2	0.4 ± 0.2	⋯
	LAT (67.2–560.1)	25	14.1	48	-2.1 ± 0.3	0.7 ± 0.2	0.3 ± 0.2	⋯
130325A	LTF (0.0–10000.0)	277	27.2	64	-2.1 ± 0.2	0.08 ± 0.02	0.8 ± 0.4	⋯
	EXT (7.7–1029.7)	60	8.5	36	-1.7 ± 0.3	0.13 ± 0.06	0.4 ± 0.3	⋯
	LAT (324.1–1029.7)	43	5.9	33	-1.5 ± 0.3	0.12 ± 0.06	0.4 ± 0.4	⋯
130327B	GBM (2.0–33.3)	12	10.1	68	-1.8 ± 0.3	7 ± 2	0.3 ± 0.3	⋯
	LTF (0.0–100.0)	44	39.5	328	-1.7 ± 0.1	8 ± 1	1.8 ± 0.8	⋯
	EXT (33.3–523.2)	111	45.2	205	-1.8 ± 0.1	1.4 ± 0.2	1.5 ± 0.7	⋯
	LAT (8.0–523.2)	123	55.0	251	-1.8 ± 0.1	1.6 ± 0.2	1.7 ± 0.7	⋯
130427A	GBM (4.1–142.3)	283	270.8	2765	-1.90 ± 0.05	52 ± 3	10 ± 1	1.7 ± 0.1
	LTF (0.0–500.0)	558	518.4	4514	-1.97 ± 0.04	22 ± 1	13 ± 2	2.5 ± 0.2
	EXT (142.3–34366.2)	589	368.2	1397	-2.12 ± 0.06	0.68 ± 0.04	19 ± 2	4.5 ± 0.3
	LAT (0.1–34366.2)	877	635.9	2795	-1.99 ± 0.04	1.13 ± 0.05	45 ± 4	8.6 ± 0.4
130502B	GBM (7.2–31.5)	21	20.9	219	-2.2 ± 0.2	26 ± 6	0.5 ± 0.2	⋯
	LTF (0.0–500.0)	84	72.0	407	-2.0 ± 0.1	4.3 ± 0.6	2.2 ± 0.8	⋯
	EXT (31.5–1316.6)	80	55.3	238	-2.0 ± 0.1	1.1 ± 0.2	1.6 ± 0.7	⋯
	LAT (12.4–1316.6)	101	74.9	345	-2.0 ± 0.1	1.5 ± 0.2	2.1 ± 0.8	⋯
130504C	GBM (8.7–81.9)	8	7.4	29	-2.5 ± 0.5	3 ± 1	0.10 ± 0.05	⋯
	LTF (0.0–500.0)	67	23.3	104	-1.9 ± 0.2	0.8 ± 0.2	0.6 ± 0.3	⋯
	EXT (81.9–590.3)	69	18.2	84	-1.9 ± 0.2	0.6 ± 0.2	0.5 ± 0.3	⋯
	LAT (42.6–590.3)	75	23.0	103	-1.9 ± 0.2	0.7 ± 0.2	0.5 ± 0.3	⋯
130518A	GBM (9.9–58.5)	12	10.8	54	-3.5 ± 0.7	6 ± 2	0.07 ± 0.03	7 ± 5
	LTF (0.0–500.0)	62	38.8	165	-2.7 ± 0.3	2.8 ± 0.5	0.5 ± 0.1	18 ± 5
	EXT (58.5–343.6)	45	28.9	136	-2.7 ± 0.3	2.7 ± 0.6	0.29 ± 0.08	10 ± 3
	LAT (26.8–343.6)	56	38.4	174	-2.9 ± 0.3	3.2 ± 0.6	0.35 ± 0.08	15 ± 5
130606B	LTF (0.0–4000.0)	36	18.1	96	-1.8 ± 0.2	0.6 ± 0.2	5 ± 4	⋯
	EXT (57.6–527.3)	27	17.0	96	-1.7 ± 0.2	0.9 ± 0.3	1.0 ± 0.8	⋯
	LAT (130.5–527.3)	27	16.9	96	-1.7 ± 0.2	0.9 ± 0.3	0.8 ± 0.6	⋯
130702A	LTF (0.0–4000.0)	12	7.9	26	-2.0 ± 0.3	0.13 ± 0.05	0.6 ± 0.5	0.019 ± 0.009
130821A	GBM (3.6–90.6)	12	8.5	52	-2.6 ± 0.5	2.0 ± 0.7	0.08 ± 0.04	⋯
	LTF (0.0–10000.0)	252	81.9	202	-2.4 ± 0.2	0.27 ± 0.04	1.4 ± 0.3	⋯
	EXT (90.6–6103.7)	173	64.7	173	-2.3 ± 0.2	0.34 ± 0.08	1.2 ± 0.3	⋯
	LAT (33.9–6103.7)	183	71.9	198	-2.4 ± 0.2	0.37 ± 0.05	1.2 ± 0.3	⋯
130828A	GBM (13.3–150.3)	34	32.7	290	-2.4 ± 0.2	6 ± 1	0.5 ± 0.2	⋯
	LTF (0.0–100.0)	33	31.7	287	-2.3 ± 0.2	7 ± 1	0.4 ± 0.1	⋯
	EXT (150.3–616.8)	23	6.9	23	-2.0 ± 0.4	0.2 ± 0.1	0.1 ± 0.1	⋯
	LAT (17.1–616.8)	57	40.3	145	-2.2 ± 0.2	1.2 ± 0.2	0.5 ± 0.2	⋯

Table 4
(Continued)

GRB Name	Interval ($t_0 - t_1$) (s)	Trans. Ev. in the ROI	Trans. Ev. Predicted	Test Statistic (TS)	Spectral Index	Flux ($\times 10^{-5}$ cm^{-2} s^{-1})	Fluence ($\times 10^{-5}$ erg cm^{-2})	$E_{\rm iso}$ (100 MeV–10 GeV) ($\times 10^{52}$ erg)
130907A	LTF (0.0–10000.0)	48	10.6	34	-2.1 ± 0.4	0.08 ± 0.04	0.7 ± 0.5	2.4 ± 0.9
	EXT (210.0–4010.9)	12	3.6	20	-1.8 ± 0.5	0.14 ± 0.10	1 ± 1	2 ± 1
131014A	GBM (1.0–4.2)	10	10.0	132	-2.0 ± 0.3	400 ± 100	1 ± 1	⋯
	LTF (0.0–10.0)	12	11.9	132	-1.9 ± 0.3	140 ± 40	2 ± 1	⋯
	EXT (4.2–200.4)	19	15.5	82	-2.0 ± 0.2	4 ± 1	0.9 ± 0.6	⋯
	LAT (1.9–200.4)	29	25.1	155	-1.9 ± 0.2	6 ± 1	1.7 ± 1.0	⋯
131029A	GBM (1.0–105.5)	23	22.9	223	-2.6 ± 0.3	13 ± 3	0.6 ± 0.2	⋯
	LTF (0.0–500.0)	46	36.2	177	-2.4 ± 0.2	2.4 ± 0.5	0.6 ± 0.2	⋯
	EXT (105.5–557.2)	24	13.2	35	-2.3 ± 0.3	0.8 ± 0.3	0.2 ± 0.1	⋯
	LAT (38.7–557.2)	47	37.2	185	-2.4 ± 0.2	2.1 ± 0.4	0.6 ± 0.2	⋯
131108A	GBM (0.3–18.5)	136	135.4	1695	-2.6 ± 0.1	120 ± 10	0.9 ± 0.1	24 ± 3
	LTF (0.0–10.0)	136	135.8	1857	-2.6 ± 0.1	210 ± 20	0.9 ± 0.1	24 ± 3
	EXT (18.5–678.1)	60	43.0	112	-2.8 ± 0.3	1.0 ± 0.2	0.24 ± 0.05	9 ± 2
	LAT (0.0–678.1)	223	202.0	1321	-2.7 ± 0.1	4.6 ± 0.3	1.2 ± 0.1	37 ± 4
131209A	LTF (0.0–500.0)	38	12.8	28	-3.5 ± 0.7	0.6 ± 0.2	0.08 ± 0.03	⋯
	EXT (16.4–374.8)	30	9.3	22	-3.3 ± 0.8	0.6 ± 0.2	0.06 ± 0.03	⋯
	LAT (14.3–374.8)	32	11.4	27	-3.3 ± 0.7	0.7 ± 0.2	0.07 ± 0.03	⋯
131231A	GBM (13.3–44.5)	5	4.8	31	-2.7 ± 0.7	4 ± 2	0.05 ± 0.03	0.07 ± 0.03
	LTF (0.0–4000.0)	66	40.9	261	-1.7 ± 0.1	0.6 ± 0.1	6 ± 3	2.4 ± 0.6
	EXT (44.5–4824.2)	80	36.5	244	-1.6 ± 0.1	0.28 ± 0.05	4 ± 2	1.5 ± 0.4
	LAT (23.1–4824.2)	84	40.0	256	-1.7 ± 0.1	0.31 ± 0.06	4 ± 2	1.6 ± 0.3
140102A	LTF (0.0–100.0)	18	13.8	77	-2.1 ± 0.3	2.9 ± 0.9	0.2 ± 0.1	⋯
	EXT (4.1–60.2)	12	11.6	104	-2.1 ± 0.3	4 ± 1	0.2 ± 0.1	⋯
	LAT (3.1–60.2)	14	13.6	119	-2.1 ± 0.3	5 ± 1	0.2 ± 0.1	⋯
140104B	LTF (0.0–4000.0)	86	23.0	72	-2.0 ± 0.2	0.21 ± 0.06	1.0 ± 0.5	⋯
	EXT (198.1–1174.0)	41	18.8	73	-2.0 ± 0.2	0.4 ± 0.1	0.4 ± 0.3	⋯
	LAT (227.3–1174.0)	36	17.7	72	-2.0 ± 0.2	0.4 ± 0.1	0.4 ± 0.2	⋯
140110A	GBM (−0.3–9.2)	29	28.8	330	-2.6 ± 0.3	60 ± 10	0.22 ± 0.07	⋯
	LTF (0.0–10.0)	30	29.8	339	-2.6 ± 0.3	50 ± 10	0.22 ± 0.06	⋯
	EXT (9.2–159.4)	14	9.5	31	-2.3 ± 0.4	1.0 ± 0.4	0.09 ± 0.06	⋯
	LAT (0.6–159.4)	42	37.9	231	-2.6 ± 0.3	3.9 ± 0.7	0.25 ± 0.07	⋯
140124A	LTF (0.0–500.0)	33	5.4	26	-1.6 ± 0.3	0.18 ± 0.10	0.4 ± 0.4	⋯
140206B	GBM (7.5–154.2)	25	24.0	183	-2.8 ± 0.3	4.2 ± 0.9	0.22 ± 0.07	⋯
	LTF (0.0–10000.0)	245	87.2	302	-2.1 ± 0.1	0.30 ± 0.04	2.6 ± 0.7	⋯
	EXT (154.2–8585.0)	218	62.9	239	-1.9 ± 0.1	0.22 ± 0.03	2.3 ± 0.7	⋯
	LAT (0.6–8585.0)	244	85.8	298	-2.1 ± 0.1	0.30 ± 0.04	2.3 ± 0.6	⋯
140219A	LTF (0.0–4000.0)	43	12.2	31	-2.2 ± 0.3	0.19 ± 0.07	0.6 ± 0.4	⋯
140323A	LTF (0.0–4000.0)	15	6.8	40	-1.5 ± 0.3	0.17 ± 0.09	3 ± 3	⋯
	EXT (116.5–715.6)	12	4.1	21	-1.6 ± 0.4	0.14 ± 0.09	0.4 ± 0.4	⋯
140402A	GBM (−0.1–0.2)	4	4.0	61	-2.4 ± 0.6	180 ± 90	0.03 ± 0.03	⋯
	LTF (0.0–100.0)	21	14.3	92	-1.8 ± 0.2	2.0 ± 0.6	0.4 ± 0.3	⋯
	EXT (0.2–71.7)	16	9.4	62	-1.7 ± 0.3	1.8 ± 0.7	0.3 ± 0.3	⋯
	LAT (0.1–71.7)	18	10.4	76	-1.8 ± 0.3	2.0 ± 0.8	0.3 ± 0.3	⋯
140416A	LTF (0.0–4000.0)	64	13.2	35	-2.0 ± 0.3	0.17 ± 0.07	0.7 ± 0.5	⋯
	EXT (29.0–2207.4)	46	14.1	22	-2.4 ± 0.4	0.24 ± 0.08	0.3 ± 0.1	⋯
140523A	GBM (0.6–19.8)	15	14.8	160	-1.9 ± 0.2	28 ± 7	0.8 ± 0.5	⋯
	LTF (0.0–500.0)	44	42.6	368	-2.0 ± 0.1	4.7 ± 0.8	2 ± 1	⋯
	EXT (19.8–470.2)	26	24.9	197	-2.0 ± 0.2	3.0 ± 0.6	1.4 ± 0.6	⋯
	LAT (1.6–470.2)	41	39.6	343	-2.0 ± 0.1	4.5 ± 0.8	2 ± 1	⋯

Table 4
(Continued)

GRB Name	Interval ($t_0 - t_1$) (s)	Trans. Ev. in the ROI	Trans. Ev. Predicted	Test Statistic (TS)	Spectral Index	Flux ($\times 10^{-5}$ cm^{-2} s^{-1})	Fluence ($\times 10^{-5}$ erg cm^{-2})	$E_{\rm iso}$ (100 MeV–10 GeV) ($\times 10^{52}$ erg)
140528A	LTF (0.0–4000.0)	119	19.2	36	-2.1 ± 0.3	0.14 ± 0.05	0.5 ± 0.3	⋯
	EXT (14.6–1377.9)	67	14.0	34	-2.0 ± 0.3	0.18 ± 0.07	0.3 ± 0.2	⋯
	LAT (81.1–1377.9)	66	14.1	34	-2.0 ± 0.3	0.19 ± 0.07	0.3 ± 0.2	⋯
140619B	GBM (−0.3–2.6)	21	21.0	314	-2.0 ± 0.2	140 ± 30	0.5 ± 0.3	⋯
	LTF (0.0–10.0)	25	24.9	314	-1.9 ± 0.2	47 ± 9	0.6 ± 0.3	⋯
	EXT (2.6–5.3)	3	2.9	28	-1.7 ± 0.4	20 ± 10	0.1 ± 0.2	⋯
	LAT (0.2–5.3)	23	22.9	319	-1.9 ± 0.2	80 ± 20	0.6 ± 0.3	⋯
140723A	GBM (0.0–56.3)	31	26.1	113	-2.2 ± 0.2	13 ± 3	0.5 ± 0.2	⋯
	LTF (0.0–100.0)	33	32.4	270	-2.2 ± 0.2	9 ± 2	0.6 ± 0.2	⋯
	EXT (56.3–103.8)	3	3.0	25	-1.8 ± 0.5	1.6 ± 0.9	0.1 ± 0.2	⋯
	LAT (0.6–103.8)	34	33.4	282	-2.2 ± 0.2	9 ± 2	0.7 ± 0.2	⋯
140729A	GBM (0.5–56.1)	11	9.5	64	-1.9 ± 0.3	2.5 ± 0.9	0.2 ± 0.2	⋯
	LTF (0.0–100.0)	15	11.9	68	-1.8 ± 0.2	1.7 ± 0.5	0.3 ± 0.3	⋯
	LAT (4.8–58.9)	10	8.5	57	-1.8 ± 0.3	2.3 ± 0.8	0.2 ± 0.2	⋯
140810A	LTF (0.0–4000.0)	49	13.6	82	-1.7 ± 0.3	0.11 ± 0.04	1 ± 1	⋯
	EXT (88.3–18827.5)	152	13.5	73	-1.5 ± 0.2	0.03 ± 0.01	3 ± 2	⋯
	LAT (460.8–18827.5)	150	13.0	72	-1.5 ± 0.2	0.03 ± 0.01	3 ± 2	⋯
140928A	LTF (0.0–4000.0)	35	6.6	61	-1.2 ± 0.3	0.06 ± 0.03	3 ± 3	⋯
	EXT (7.2–2554.7)	19	7.0	22	-2.1 ± 0.4	0.14 ± 0.07	0.3 ± 0.3	⋯
	LAT (1676.6–2554.7)	16	5.2	21	-1.9 ± 0.5	0.11 ± 0.07	0.1 ± 0.1	⋯
141012A	GBM (−25.9–11.8)	8	7.7	61	-2.4 ± 0.4	7 ± 2	0.13 ± 0.08	⋯
	LTF (0.0–10000.0)	21	17.6	120	-2.1 ± 0.3	4 ± 1	30 ± 20	⋯
	EXT (11.8–107.0)	12	10.5	79	-1.9 ± 0.3	3 ± 1	0.4 ± 0.3	⋯
	LAT(3.1–107.0)	16	14.5	118	-2.0 ± 0.2	4 ± 1	0.5 ± 0.3	⋯
141028A	GBM (6.7–38.1)	20	18.9	169	-3.2 ± 0.5	13 ± 3	0.12 ± 0.03	7 ± 3
	LTF (0.0–500.0)	40	34.8	156	-2.5 ± 0.2	1.9 ± 0.3	0.4 ± 0.1	10 ± 2
	EXT (38.1–500.5)	20	15.7	90	-2.0 ± 0.2	0.9 ± 0.2	0.4 ± 0.3	4 ± 1
	LAT (10.9–500.5)	39	33.8	152	-2.4 ± 0.2	1.8 ± 0.3	0.5 ± 0.1	9 ± 2
141102A	LTF (0.0–100.0)	15	9.9	33	-2.4 ± 0.4	3 ± 1	0.15 ± 0.09	⋯
	EXT (2.6–34.5)	8	6.4	49	-2.0 ± 0.4	6 ± 2	0.2 ± 0.2	⋯
	LAT (3.5–34.5)	7	5.3	40	-1.9 ± 0.4	5 ± 2	0.2 ± 0.2	⋯
141113A	GBM (−0.1–0.4)	4	4.0	60	-2.1 ± 0.5	200 ± 100	0.1 ± 0.1	⋯
	LTF (0.0–100.0)	8	7.6	37	-2.1 ± 0.4	1.6 ± 0.6	0.1 ± 0.1	⋯
	LAT (0.1–3.5)	4	4.0	40	-2.6 ± 0.7	30 ± 20	0.05 ± 0.04	⋯
141207A	GBM (1.3–22.3)	39	38.8	495	-1.9 ± 0.1	70 ± 10	2.0 ± 0.8	⋯
	LTF (0.0–100.0)	47	44.9	414	-2.0 ± 0.1	16 ± 2	1.8 ± 0.7	⋯
	EXT (22.3–734.3)	29	8.7	32	-1.8 ± 0.3	0.2 ± 0.1	0.3 ± 0.3	⋯
	LAT (1.8–734.3)	67	46.9	197	-1.8 ± 0.1	1.2 ± 0.2	1.7 ± 0.6	⋯
141221B	LTF (0.0–100.0)	12	7.0	41	-1.9 ± 0.4	1.2 ± 0.5	0.2 ± 0.2	⋯
	EXT (31.2–58.5)	5	3.6	40	-1.5 ± 0.4	2 ± 1	0.3 ± 0.4	⋯
	LAT (22.2–58.5)	8	4.5	39	-1.6 ± 0.4	2 ± 1	0.3 ± 0.3	⋯
141222A	EXT (2.8–440.6)	67	15.0	39	-2.1 ± 0.3	0.8 ± 0.3	0.3 ± 0.2	⋯
	LAT (34.2–440.6)	67	15.0	39	-2.1 ± 0.3	0.8 ± 0.3	0.3 ± 0.2	⋯
150118B	LTF (0.0–500.0)	10	7.6	30	-2.5 ± 0.5	9 ± 4	2 ± 1	⋯
150202B	LTF (0.0–4000.0)	57	11.8	29	-2.2 ± 0.4	0.16 ± 0.07	0.5 ± 0.3	⋯
150210A	GBM (0.0–31.3)	16	15.2	157	-2.2 ± 0.3	13 ± 3	0.3 ± 0.2	⋯
	LTF (0.0–10.0)	14	13.1	112	-2.3 ± 0.3	40 ± 10	0.2 ± 0.1	⋯
	LAT (0.8–169.4)	23	20.5	77	-2.2 ± 0.3	3.3 ± 0.8	0.4 ± 0.2	⋯
150314A	LTF (0.0–500.0)	34	17.6	38	-2.7 ± 0.4	0.7 ± 0.2	0.15 ± 0.06	2.2 ± 0.7

Table 4
(Continued)

GRB Name	Interval ($t_0 - t_1$) (s)	Trans. Ev. in the ROI	Trans. Ev. Predicted	Test Statistic (TS)	Spectral Index	Flux ($\times 10^{-5}$ cm^{-2} s^{-1})	Fluence ($\times 10^{-5}$ erg cm^{-2})	$E_{\rm iso}$ (100 MeV–10 GeV) ($\times 10^{52}$ erg)
	LAT (0.1–3064.3)	137	18.3	23	-2.5 ± 0.4	0.10 ± 0.04	0.15 ± 0.06	1.8 ± 0.7
150403A	LTF (0.0–4000.0)	101	19.0	49	-1.9 ± 0.2	0.10 ± 0.03	0.5 ± 0.3	3.2 ± 1.0
	EXT (25.6–970.5)	32	8.6	36	-1.7 ± 0.3	0.18 ± 0.08	0.4 ± 0.4	1.4 ± 0.6
	LAT (399.5–970.5)	27	8.5	38	-1.7 ± 0.3	0.22 ± 0.10	0.3 ± 0.3	1.1 ± 0.4
150510A	GBM (0.4–52.3)	8	6.9	46	-2.4 ± 0.5	5 ± 2	0.12 ± 0.08	⋯
	LTF (0.0–500.0)	22	11.4	56	-1.9 ± 0.3	0.7 ± 0.2	0.6 ± 0.4	⋯
	EXT (52.3–147.6)	7	4.6	36	-1.7 ± 0.4	1.5 ± 0.8	0.3 ± 0.4	⋯
	LAT (2.4–147.6)	15	9.6	55	-2.0 ± 0.3	2.2 ± 0.8	0.4 ± 0.3	⋯
150513A	GBM (−157.2–1.8)	11	10.3	24	-2.5 ± 0.4	1.7 ± 0.6	0.12 ± 0.07	⋯
150514A	LTF (0.0–4000.0)	29	3.0	31	-1.3 ± 0.5	0.06 ± 0.05	2 ± 3	0.5 ± 0.4
	EXT (10.8–597.6)	24	2.4	31	-1.1 ± 0.4	0.06 ± 0.05	0.5 ± 0.6	0.08 ± 0.06
	LAT (442.4–597.6)	4	2.0	39	-1.0 ± 0.4	0.2 ± 0.1	0.7 ± 0.7	0.06 ± 0.05
150523A	GBM (1.8–84.2)	40	27.9	178	-2.1 ± 0.2	6 ± 1	0.4 ± 0.2	⋯
	LTF (0.0–500.0)	106	51.0	248	-2.0 ± 0.1	1.6 ± 0.3	0.9 ± 0.3	⋯
	EXT (84.2–6129.1)	344	31.3	116	-1.8 ± 0.2	0.20 ± 0.05	3 ± 1	⋯
	LAT (3.9–6129.1)	384	59.3	211	-1.9 ± 0.1	0.39 ± 0.06	3 ± 1	⋯
150627A	LTF (0.0–4000.0)	405	47.5	238	-1.7 ± 0.1	0.25 ± 0.05	3 ± 1	⋯
	EXT (69.9–6143.0)	449	49.8	237	-1.7 ± 0.1	0.24 ± 0.04	4 ± 1	⋯
	LAT (152.0–6143.0)	442	49.7	239	-1.7 ± 0.1	0.24 ± 0.04	4 ± 1	⋯
150702A	LTF (0.0–4000.0)	57	13.4	32	-2.2 ± 0.3	0.12 ± 0.04	0.3 ± 0.2	⋯
	EXT (47.2–1737.1)	32	10.4	30	-2.3 ± 0.4	0.16 ± 0.06	0.15 ± 0.09	⋯
	LAT (512.6–1737.1)	29	8.1	24	-2.2 ± 0.4	0.13 ± 0.06	0.11 ± 0.08	⋯
150902A	GBM (3.8–17.4)	21	20.4	160	-3.1 ± 0.4	37 ± 8	0.15 ± 0.05	⋯
	LTF (0.0–500.0)	110	51.1	203	-2.3 ± 0.2	2.0 ± 0.4	0.6 ± 0.2	⋯
	EXT (17.4–408.7)	73	30.5	115	-2.1 ± 0.2	1.5 ± 0.3	0.6 ± 0.2	⋯
	LAT (3.5–408.7)	94	49.3	212	-2.3 ± 0.2	2.4 ± 0.4	0.6 ± 0.2	⋯
160310A	LTF (0.0–10000.0)	71	6.4	30	-1.6 ± 0.4	0.10 ± 0.08	3 ± 4	⋯
160314B	LTF (0.0–10000.0)	32	11.6	28	-2.1 ± 0.3	0.15 ± 0.06	1.2 ± 0.8	⋯
160325A	LTF (0.0–4000.0)	73	36.2	97	-2.4 ± 0.2	0.46 ± 0.10	1.0 ± 0.3	⋯
	EXT (45.0–1555.7)	69	34.2	93	-2.4 ± 0.2	0.5 ± 0.1	0.4 ± 0.1	⋯
	LAT (5.0–1555.7)	71	35.4	95	-2.4 ± 0.2	0.48 ± 0.10	0.4 ± 0.1	⋯
160422A	LTF (0.0–4000.0)	60	4.8	36	-1.3 ± 0.3	0.03 ± 0.02	1 ± 1	⋯
	EXT (13.1–1061.4)	18	3.5	36	-1.2 ± 0.3	0.09 ± 0.06	1 ± 1	⋯
160503A	LTF (0.0–10000.0)	54	16.8	33	-2.6 ± 0.4	0.17 ± 0.05	0.7 ± 0.3	⋯
	EXT (26.1–23075.4)	141	28.3	37	-2.8 ± 0.4	0.12 ± 0.03	1.0 ± 0.3	⋯
	LAT (5324.7–23075.4)	94	19.3	23	-3.1 ± 0.5	0.14 ± 0.04	0.7 ± 0.2	⋯
160509A	GBM (8.2–377.9)	165	130.1	694	-2.4 ± 0.1	5.9 ± 0.6	1.1 ± 0.2	5.2 ± 0.5
	LTF (0.0–100.0)	135	118.3	716	-2.9 ± 0.2	22 ± 2	0.7 ± 0.1	5.4 ± 0.6
	EXT (377.9–5687.4)	183	19.0	39	-2.1 ± 0.3	0.11 ± 0.04	0.5 ± 0.3	1.5 ± 0.5
	LAT (9.6–5687.4)	348	148.4	371	-2.4 ± 0.1	0.76 ± 0.08	2.3 ± 0.4	10 ± 1
160521B	LTF (0.0–4000.0)	111	10.0	59	-1.5 ± 0.2	0.05 ± 0.02	1.1 ± 0.8	⋯
	EXT (3.1–11911.6)	207	9.3	50	-1.4 ± 0.3	0.020 ± 0.009	2 ± 1	⋯
	LAT (90.2–11911.6)	205	8.7	50	-1.4 ± 0.3	0.019 ± 0.009	2 ± 1	⋯
160623A	LTF (0.0–10000.0)	401	97.0	258	-2.0 ± 0.1	0.8 ± 0.1	9 ± 3	2.1 ± 0.4
	EXT (106.5–12160.0)	429	98.3	266	-2.0 ± 0.1	0.8 ± 0.1	11 ± 3	2.4 ± 0.3

Table 4
(Continued)

GRB Name	Interval ($t_0 - t_1$) (s)	Trans. Ev. in the ROI	Trans. Ev. Predicted	Test Statistic (TS)	Spectral Index	Flux ($\times 10^{-5}$ cm^{-2} s^{-1})	Fluence ($\times 10^{-5}$ erg cm^{-2})	$E_{\rm iso}$ (100 MeV–10 GeV) ($\times 10^{52}$ erg)
	LAT (401.5–12160.0)	427	98.3	267	-2.0 ± 0.1	0.8 ± 0.1	11 ± 3	2.4 ± 0.3
160625B	GBM (188.5–641.8)	272	258.3	2387	-2.33 ± 0.08	9.4 ± 0.6	2.5 ± 0.3	15 ± 1
	LTF (0.0–500.0)	270	255.8	2239	-2.43 ± 0.08	9.4 ± 0.6	2.4 ± 0.3	16 ± 1
	EXT (641.8–840.5)	20	9.3	52	-1.8 ± 0.3	0.7 ± 0.3	0.3 ± 0.3	0.6 ± 0.2
	LAT (25.6–840.5)	310	283.0	2222	-2.35 ± 0.07	6.0 ± 0.4	2.7 ± 0.3	17 ± 1
160702A	LTF (0.0–4000.0)	30	3.8	31	-1.4 ± 0.4	0.07 ± 0.05	2 ± 2	⋯
	EXT (0.2–2215.6)	22	3.8	33	-1.4 ± 0.4	0.10 ± 0.07	2 ± 2	⋯
160709A	GBM (0.0–5.4)	24	24.0	310	-2.4 ± 0.3	100 ± 20	0.3 ± 0.1	⋯
	LTF (0.0–10.0)	25	24.9	291	-2.5 ± 0.3	60 ± 10	0.3 ± 0.1	⋯
	EXT (5.4–25.8)	5	3.9	29	-2.5 ± 0.7	5 ± 2	0.04 ± 0.04	⋯
	LAT (0.5–25.8)	27	26.2	285	-2.4 ± 0.3	24 ± 5	0.3 ± 0.1	⋯
160816A	GBM (0.4–11.5)	19	16.7	146	-2.7 ± 0.4	26 ± 7	0.11 ± 0.04	⋯
	LTF (0.0–100.0)	52	41.2	261	-2.3 ± 0.2	7 ± 1	0.4 ± 0.1	⋯
	EXT (11.5–1094.8)	159	45.0	127	-2.2 ± 0.2	0.6 ± 0.1	0.5 ± 0.2	⋯
	LAT (1.1–1094.8)	178	60.7	182	-2.2 ± 0.2	0.8 ± 0.1	0.6 ± 0.2	⋯
160821A	GBM (118.5–161.5)	36	35.5	338	-5.1 ± 0.7	17 ± 3	0.16 ± 0.03	⋯
	LTF (0.0–500.0)	58	55.6	474	-2.7 ± 0.2	4.1 ± 0.6	0.8 ± 0.2	⋯
	EXT (161.5–1459.2)	20	19.5	163	-1.8 ± 0.2	1.8 ± 0.4	5 ± 3	⋯
	LAT (92.1–1459.2)	57	55.6	516	-2.6 ± 0.2	4.2 ± 0.6	2.4 ± 0.5	⋯
160829A	LTF (0.0–100.0)	20	4.3	31	-1.3 ± 0.4	0.6 ± 0.3	0.5 ± 0.7	⋯
	EXT (0.4–31.7)	5	2.8	31	-1.3 ± 0.3	1.2 ± 0.8	0.4 ± 0.4	⋯
	LAT (0.9–31.7)	5	2.8	31	-1.3 ± 0.3	1.2 ± 0.8	0.4 ± 0.4	⋯
160905A	GBM (3.8–37.4)	6	5.8	54	-1.7 ± 0.3	3 ± 1	0.3 ± 0.3	⋯
	LTF (0.0–500.0)	62	28.1	147	-1.8 ± 0.2	0.9 ± 0.2	0.8 ± 0.4	⋯
	EXT (37.4–463.3)	52	22.2	106	-1.8 ± 0.2	0.8 ± 0.2	0.6 ± 0.3	⋯
	LAT (7.8–463.3)	57	27.3	147	-1.8 ± 0.2	0.9 ± 0.2	0.8 ± 0.4	⋯
160910A	LTF (0.0–500.0)	14	9.0	44	-2.5 ± 0.5	1.6 ± 0.6	0.4 ± 0.2	⋯
161015A	GBM (0.3–15.4)	12	10.8	95	-2.2 ± 0.4	16 ± 5	0.2 ± 0.1	⋯
	LTF (0.0–10.0)	12	11.0	104	-2.2 ± 0.3	24 ± 8	0.2 ± 0.1	⋯
	LAT (1.1–7.5)	9	8.1	68	-2.7 ± 0.6	30 ± 10	0.07 ± 0.04	⋯
161109A	LTF (0.0–4000.0)	51	18.3	44	-2.2 ± 0.3	0.31 ± 0.10	0.9 ± 0.4	⋯
	EXT (27.4–890.9)	15	11.7	47	-2.2 ± 0.3	0.8 ± 0.3	0.5 ± 0.3	⋯
	LAT (423.4–890.9)	14	10.6	43	-2.2 ± 0.3	0.8 ± 0.3	0.3 ± 0.2	⋯
170115B	GBM (0.5–44.8)	22	17.3	92	-3.2 ± 0.5	7 ± 2	0.09 ± 0.03	⋯
	LTF (0.0–10.0)	15	13.5	111	-3.0 ± 0.5	24 ± 7	0.08 ± 0.03	⋯
	EXT (44.8–1027.9)	105	24.8	40	-2.5 ± 0.3	0.4 ± 0.1	0.17 ± 0.07	⋯
	LAT (1.3–1027.9)	127	40.5	69	-2.7 ± 0.4	0.6 ± 0.2	0.24 ± 0.05	⋯
170127C	LTF (0.0–4000.0)	65	15.6	32	-3.1 ± 0.5	0.12 ± 0.04	0.14 ± 0.05	⋯
	EXT (0.1–2889.0)	63	15.7	33	-3.1 ± 0.5	0.12 ± 0.04	0.10 ± 0.04	⋯
	LAT (664.8–2889.0)	52	14.5	36	-2.9 ± 0.5	0.12 ± 0.04	0.09 ± 0.03	⋯
170214A	GBM (12.5–135.4)	123	114.2	846	-2.7 ± 0.1	19 ± 2	0.9 ± 0.1	32 ± 5
	LTF (0.0–500.0)	265	228.7	1493	-2.45 ± 0.09	8.2 ± 0.6	2.0 ± 0.2	49 ± 4
	EXT (135.4–752.0)	179	138.8	819	-2.3 ± 0.1	3.8 ± 0.4	1.4 ± 0.3	27 ± 2
	LAT (39.5–752.0)	297	250.3	1571	-2.45 ± 0.09	6.1 ± 0.4	2.1 ± 0.2	53 ± 4
170306B	LTF (0.0–100.0)	6	5.9	35	-2.7 ± 0.6	2.2 ± 0.9	0.09 ± 0.05	⋯
	EXT (23.6–47.4)	3	3.0	28	-2.8 ± 0.9	5 ± 3	0.04 ± 0.03	⋯
	LAT (21.2–47.4)	3	3.0	27	-2.8 ± 0.9	4 ± 2	0.04 ± 0.03	⋯
170329A	GBM (0.3–33.8)	11	9.8	91	-2.1 ± 0.4	6 ± 2	0.2 ± 0.1	⋯
	LTF (0.0–100.0)	19	14.7	80	-2.4 ± 0.3	3.2 ± 0.9	0.18 ± 0.09	⋯
	LAT (3.9–52.4)	14	11.3	69	-2.2 ± 0.3	5 ± 2	0.2 ± 0.1	⋯

Table 4
(Continued)

GRB Name	Interval ($t_0 - t_1$) (s)	Trans. Ev. in the ROI	Trans. Ev. Predicted	Test Statistic (TS)	Spectral Index	Flux ($\times 10^{-5}$ cm^{-2} s^{-1})	Fluence ($\times 10^{-5}$ erg cm^{-2})	$E_{\rm iso}$ (100 MeV–10 GeV) ($\times 10^{52}$ erg)
170405A	GBM (7.4–86.0)	10	8.4	33	-5 ± 2	4 ± 2	0.07 ± 0.03	300 ± 800
	LTF (0.0–4000.0)	73	29.1	59	-2.7 ± 0.3	0.4 ± 0.1	0.7 ± 0.2	50 ± 20
	EXT (86.0–868.0)	45	19.8	50	-2.5 ± 0.3	0.5 ± 0.1	0.17 ± 0.07	9 ± 4
	LAT (17.8–868.0)	55	26.1	56	-2.8 ± 0.3	0.6 ± 0.2	0.19 ± 0.05	16 ± 7
170409A	LTF (0.0–500.0)	18	13.5	55	-2.1 ± 0.3	1.2 ± 0.4	0.6 ± 0.4	⋯
	EXT (93.4–440.3)	18	13.5	55	-2.1 ± 0.3	1.3 ± 0.4	0.4 ± 0.3	⋯
	LAT (178.4–440.3)	18	13.4	54	-2.1 ± 0.3	1.3 ± 0.4	0.3 ± 0.2	⋯
170424A	GBM (2.8–56.1)	3	3.0	31	-1.9 ± 0.5	2 ± 1	0.1 ± 0.2	⋯
	LTF (0.0–500.0)	18	12.8	44	-2.3 ± 0.3	1.1 ± 0.3	0.3 ± 0.2	⋯
	EXT (56.1–107.7)	3	3.0	25	-2.4 ± 0.7	2 ± 1	0.06 ± 0.06	⋯
	LAT (21.8–107.7)	5	5.0	36	-2.0 ± 0.4	1.9 ± 0.9	0.2 ± 0.2	⋯
170510A	GBM (2.8–130.6)	9	6.9	42	-2.2 ± 0.4	3 ± 1	0.3 ± 0.2	⋯
	LTF (0.0–100.0)	8	6.6	47	-2.2 ± 0.4	4 ± 2	0.3 ± 0.3	⋯
	LAT (26.8–154.2)	10	9.0	36	-2.3 ± 0.4	4 ± 1	0.3 ± 0.2	⋯
170522A	GBM (0.6–8.0)	6	5.9	71	-1.8 ± 0.3	17 ± 7	0.2 ± 0.3	⋯
	LTF (0.0–100.0)	17	13.0	98	-1.7 ± 0.2	2.9 ± 0.9	0.7 ± 0.5	⋯
	EXT (8.0–41.6)	5	4.9	44	-1.5 ± 0.3	3 ± 1	0.5 ± 0.5	⋯
	LAT (2.8–41.6)	10	9.7	104	-1.6 ± 0.2	5 ± 2	0.8 ± 0.6	⋯
170728B	GBM (0.0–46.3)	5	4.8	21	-2.2 ± 0.5	2.0 ± 1.0	0.06 ± 0.06	⋯
	LTF (0.0–500.0)	18	11.0	30	-2.5 ± 0.4	0.4 ± 0.2	0.09 ± 0.05	⋯
170808B	LTF (0.0–4000.0)	52	25.1	66	-2.3 ± 0.3	0.5 ± 0.1	1.2 ± 0.5	⋯
	EXT (21.8–6205.9)	97	24.0	52	-2.1 ± 0.3	0.15 ± 0.04	0.7 ± 0.4	⋯
	LAT (13.7–6205.9)	99	26.8	55	-2.2 ± 0.3	0.17 ± 0.05	0.7 ± 0.3	⋯
170825B	LTF (0.0–10.0)	3	3.0	25	-3 ± 1	10 ± 6	0.03 ± 0.02	⋯
170906A	LTF (0.0–10000.0)	197	58.5	204	-2.1 ± 0.1	0.41 ± 0.07	4 ± 1	⋯
	EXT (90.9–1894.3)	151	55.5	205	-2.1 ± 0.1	0.57 ± 0.09	1.0 ± 0.3	⋯
	LAT (162.1–1894.3)	149	55.1	206	-2.1 ± 0.1	0.57 ± 0.09	1.0 ± 0.3	⋯
170921B	LTF (0.0–10000.0)	55	9.0	28	-1.9 ± 0.4	0.07 ± 0.03	0.9 ± 0.8	⋯
	EXT (40.4–1058.6)	15	4.6	26	-1.7 ± 0.4	0.12 ± 0.07	0.3 ± 0.4	⋯
171010A	LTF (0.0–10000.0)	231	77.6	234	-2.0 ± 0.1	0.22 ± 0.03	2.2 ± 0.6	0.43 ± 0.07
	EXT (123.9–2984.8)	141	69.0	235	-2.0 ± 0.1	0.41 ± 0.06	1.2 ± 0.3	0.23 ± 0.04
	LAT (335.6–2984.8)	141	69.0	235	-2.0 ± 0.1	0.41 ± 0.06	1.1 ± 0.3	0.21 ± 0.03
171011C	GBM (-0.4–0.0)	3	3.0	52	-2.2 ± 0.7	120 ± 70	0.04 ± 0.05	⋯
171102A	LTF (0.0–500.0)	14	10.5	38	-2.4 ± 0.4	0.4 ± 0.1	0.10 ± 0.06	⋯
	EXT (56.1–349.9)	7	5.3	22	-2.4 ± 0.6	0.3 ± 0.2	0.05 ± 0.04	⋯
	LAT (34.9–349.9)	8	6.3	25	-2.6 ± 0.6	0.4 ± 0.2	0.05 ± 0.03	⋯
171120A	GBM (0.0–44.1)	6	5.9	66	-2.1 ± 0.4	2 ± 1	0.10 ± 0.10	⋯
	LTF (0.0–4000.0)	50	36.4	147	-2.3 ± 0.2	0.8 ± 0.1	1.8 ± 0.6	⋯
	EXT (44.1–5276.0)	74	33.1	104	-2.3 ± 0.2	0.34 ± 0.07	1.2 ± 0.4	⋯
	LAT (0.3–5276.0)	79	37.4	134	-2.2 ± 0.2	0.37 ± 0.07	1.5 ± 0.5	⋯
171124A	GBM (-0.7–25.5)	22	21.0	192	-2.0 ± 0.2	12 ± 3	0.3 ± 0.2	⋯
	LTF (0.0–100.0)	33	23.6	125	-2.1 ± 0.2	3.5 ± 0.8	0.3 ± 0.1	⋯
	LAT (3.4–321.3)	45	26.2	90	-2.2 ± 0.2	1.3 ± 0.3	0.3 ± 0.1	⋯
171210A	LTF (0.0–10000.0)	169	28.2	65	-2.2 ± 0.2	0.11 ± 0.03	0.8 ± 0.3	⋯
	EXT (146.7–1374.5)	54	19.9	45	-2.4 ± 0.3	0.27 ± 0.07	0.16 ± 0.07	⋯
	LAT (5.9–1374.5)	64	24.1	59	-2.4 ± 0.3	0.30 ± 0.08	0.22 ± 0.09	⋯
171212B	LTF (0.0–4000.0)	26	7.7	26	-2.3 ± 0.5	0.18 ± 0.08	0.5 ± 0.3	⋯

Table 4
(Continued)

GRB Name	Interval ($t_0 - t_1$) (s)	Trans. Ev. in the ROI	Trans. Ev. Predicted	Test Statistic (TS)	Spectral Index	Flux ($\times 10^{-5}$ cm^{-2} s^{-1})	Fluence ($\times 10^{-5}$ erg cm^{-2})	$E_{\rm iso}$ (100 MeV–10 GeV) ($\times 10^{52}$ erg)
180210A	LTF (0.0–4000.0)	81	40.3	184	-1.8 ± 0.1	0.40 ± 0.08	3 ± 1	⋯
	EXT (43.0–1621.1)	75	33.9	168	-1.7 ± 0.1	0.35 ± 0.07	1.3 ± 0.5	⋯
	LAT (23.1–1621.1)	77	35.8	176	-1.8 ± 0.1	0.36 ± 0.07	1.3 ± 0.5	⋯
180305A	LTF (0.0–4000.0)	119	11.9	32	-1.8 ± 0.3	0.11 ± 0.05	0.8 ± 0.6	⋯
	EXT (14.6–2038.0)	100	9.1	27	-1.7 ± 0.3	0.10 ± 0.05	0.5 ± 0.4	⋯
	LAT (1613.8–2038.0)	21	6.0	21	-2 ± 1	0.3 ± 0.5	0.2 ± 0.2	⋯
180526A	LTF (0.0–10000.0)	110	14.0	48	-1.8 ± 0.3	0.13 ± 0.05	3 ± 2	⋯
	EXT (87.0–1948.6)	47	13.2	51	-1.8 ± 0.3	0.4 ± 0.1	1.2 ± 0.8	⋯
	LAT (808.9–1948.6)	44	11.9	48	-1.8 ± 0.3	0.3 ± 0.1	0.6 ± 0.5	⋯
180703A	GBM (1.5–22.3)	4	3.8	24	-3 ± 1	5 ± 3	0.03 ± 0.02	⋯
	LTF (0.0–4000.0)	40	21.9	54	-2.5 ± 0.3	0.24 ± 0.07	0.4 ± 0.1	⋯
	EXT (22.3–1614.0)	31	16.7	43	-2.4 ± 0.3	0.27 ± 0.09	0.2 ± 0.1	⋯
	LAT (3.8–1614.0)	35	19.3	47	-2.5 ± 0.3	0.31 ± 0.09	0.24 ± 0.09	⋯
180703B	LTF (0.0–100.0)	6	5.0	36	-1.8 ± 0.4	0.8 ± 0.3	0.1 ± 0.2	⋯
	EXT (1.7–34.2)	4	4.0	43	-1.6 ± 0.4	1.8 ± 0.9	0.2 ± 0.2	⋯
	LAT (8.0–34.2)	3	3.0	27	-1.7 ± 0.4	2 ± 1	0.1 ± 0.2	⋯
180718B	GBM (1.6–99.9)	12	11.2	21	-2.8 ± 0.5	3.0 ± 1.0	0.11 ± 0.05	⋯
	LTF (0.0–10.0)	8	8.0	72	-2.9 ± 0.6	20 ± 7	0.07 ± 0.03	⋯
	LAT (1.1–16.2)	8	7.9	60	-2.9 ± 0.6	13 ± 5	0.07 ± 0.04	⋯
180720B	GBM (4.4–53.2)	22	20.2	162	-3.2 ± 0.4	13 ± 3	0.19 ± 0.05	0.39 ± 0.09
	LTF (0.0–500.0)	152	136.8	984	-2.24 ± 0.10	6.0 ± 0.6	2.0 ± 0.4	2.1 ± 0.2
	EXT (53.2–625.0)	136	120.9	871	-2.15 ± 0.10	4.6 ± 0.5	2.1 ± 0.4	2.0 ± 0.2
	LAT (11.8–625.0)	157	139.3	975	-2.23 ± 0.10	5.0 ± 0.5	2.1 ± 0.4	2.2 ± 0.2

Table 5
Temporally Extended High-energy Emission

GRB Name	Peak Flux ($\times 10^{-5}$ cm^{-2} s^{-1})	Peak Flux Time (s)	Decay Index (SPL)	Decay Index 1 (BPL)	Decay Index 2 (BPL)	Break Time (BPL) (s)	Decay Index	Extended Emission Duration (s)
080825C	21 ± 8	10 ± 20	1.45 ± 0.03	⋯	⋯	⋯	1.45 ± 0.03	170.4
080916C	1800 ± 700	5.87 ± 0.08	1.1 ± 0.1	1.6 ± 0.2	0.4 ± 0.3	3.1 ± 0.3	0.4 ± 0.3	1528.8
081009	1.9 ± 1.0	100 ± 200	0.9 ± 0.2	⋯	⋯	⋯	0.9 ± 0.2	1182.4
090323	13 ± 4	90 ± 30	1.1 ± 0.1	1 ± 2	1.1 ± 0.2	2.4 ± 0.4	1.1 ± 0.1	5312.3
090328	16 ± 5	20 ± 50	0.99 ± 0.09	0.7 ± 0.4	1.1 ± 0.1	2.4 ± 0.5	0.99 ± 0.09	6136.3
090510	6000 ± 3000	0.85 ± 0.01	1.81 ± 0.08	2.3 ± 0.2	1.3 ± 0.2	0.6 ± 0.2	1.3 ± 0.2	169.9
090626	4 ± 1	100 ± 40	0.9 ± 0.2	⋯	⋯	⋯	0.9 ± 0.2	548.3
090902B	1300 ± 500	8.0 ± 0.1	1.63 ± 0.08	1.9 ± 0.2	1.2 ± 0.2	2.2 ± 0.3	1.2 ± 0.2	883.7
090926A	7000 ± 3000	9.91 ± 0.02	1.39 ± 0.08	1.8 ± 0.2	1.1 ± 0.2	2.0 ± 0.3	1.1 ± 0.2	4417.3
091003	4 ± 2	20 ± 40	0.9 ± 0.2	0.7 ± 0.4	2 ± 1	2.5 ± 0.4	0.9 ± 0.2	391.0
091031	30 ± 10	1 ± 3	1.3 ± 0.2	⋯	⋯	⋯	1.3 ± 0.2	408.1
091120	0.8 ± 0.3	200 ± 300	0.54 ± 0.09	⋯	⋯	⋯	0.54 ± 0.09	772.1
100116A	7 ± 2	110 ± 20	2.7 ± 0.2	⋯	⋯	⋯	2.7 ± 0.2	652.9
100414A	40 ± 10	30 ± 30	1.3 ± 0.1	1.8 ± 0.2	0.3 ± 0.6	2.9 ± 0.3	0.3 ± 0.6	5487.5
100423B	0.3 ± 0.4	0 ± 200	0.2 ± 0.1	⋯	⋯	⋯	0.2 ± 0.1	13.9
100511A	1.1 ± 0.4	100 ± 200	0.58 ± 0.07	⋯	⋯	⋯	0.58 ± 0.07	6326.6
100728A	0.3 ± 0.1	300 ± 600	0.8 ± 0.5	⋯	⋯	⋯	0.8 ± 0.5	1091.8
101014A	0.05 ± 0.03	2500 ± 1000	−0.2 ± 0.3	⋯	⋯	⋯	−0.2 ± 0.3	1925.3
110120A	1.7 ± 0.7	50 ± 70	0.6 ± 0.4	⋯	⋯	⋯	0.6 ± 0.4	1112.3
110428A	9 ± 5	12 ± 10	1.0 ± 0.1	⋯	⋯	⋯	1.0 ± 0.1	386.2
110518A	0.11 ± 0.06	2000 ± 1000	0.7 ± 0.5	⋯	⋯	⋯	0.7 ± 0.5	396.0
110625A	8 ± 4	260 ± 30	0.6 ± 0.3	⋯	⋯	⋯	0.6 ± 0.3	371.4
110721A	600 ± 200	0.1 ± 0.2	1.0 ± 0.1	⋯	⋯	⋯	1.0 ± 0.1	120.6
110731A	1400 ± 500	5.63 ± 0.08	1.5 ± 0.1	1.8 ± 0.1	0 ± 1	2.4 ± 0.5	0 ± 1	434.8
111210B	1.0 ± 0.4	100 ± 200	0.5 ± 0.2	⋯	⋯	⋯	0.5 ± 0.2	387.5
120226A	1.8 ± 0.9	30 ± 60	1.21 ± 0.07	⋯	⋯	⋯	1.21 ± 0.07	254.3
120316A	2.0 ± 0.8	40 ± 60	0.9 ± 0.2	⋯	⋯	⋯	0.9 ± 0.2	530.0
120526A	0.4 ± 0.2	900 ± 500	0.7 ± 0.1	⋯	⋯	⋯	0.7 ± 0.1	2614.1
120624B	8 ± 3	380 ± 20	1.2 ± 0.3	⋯	⋯	⋯	1.2 ± 0.3	1030.2
120709A	60 ± 30	0 ± 2	0.7 ± 0.1	⋯	⋯	⋯	0.7 ± 0.1	695.8
120711A	2.1 ± 0.7	400 ± 200	1.6 ± 0.2	⋯	⋯	⋯	1.6 ± 0.2	5038.3
120911B	500 ± 200	20 ± 1	1.3 ± 0.2	⋯	⋯	⋯	1.3 ± 0.2	208.5
130325A	0.2 ± 0.1	200 ± 200	0.1 ± 0.3	⋯	⋯	⋯	0.1 ± 0.3	705.7
130327B	17 ± 6	35 ± 9	1.6 ± 0.2	1.3 ± 0.9	1.7 ± 0.3	1.9 ± 0.8	1.6 ± 0.2	515.2
130427A	300 ± 100	16.5 ± 0.6	1.24 ± 0.06	0.8 ± 0.2	1.4 ± 0.1	2.7 ± 0.2	1.4 ± 0.1	34366.0
130502B	40 ± 10	28 ± 8	1.44 ± 0.06	⋯	⋯	⋯	1.44 ± 0.06	1304.2
130504C	1.6 ± 0.6	100 ± 200	0.77 ± 0.06	0.7 ± 0.1	1.0 ± 0.5	2.4 ± 0.4	0.77 ± 0.06	547.7
130518A	5 ± 2	40 ± 60	1.1 ± 0.2	⋯	⋯	⋯	1.1 ± 0.2	316.9
130606B	1.3 ± 0.5	200 ± 200	0.7 ± 0.2	⋯	⋯	⋯	0.7 ± 0.2	396.7
130821A	2.2 ± 0.8	70 ± 80	1.0 ± 0.1	⋯	⋯	⋯	1.0 ± 0.1	6069.8
130828A	70 ± 30	35 ± 2	1.0 ± 0.4	⋯	⋯	⋯	1.0 ± 0.4	599.8
131014A	5000 ± 2000	2.0 ± 0.2	0.8 ± 0.2	⋯	⋯	⋯	0.8 ± 0.2	198.6
131029A	22 ± 8	50 ± 20	1.1 ± 0.2	⋯	⋯	⋯	1.1 ± 0.2	518.5
131108A	3000 ± 1000	0.13 ± 0.03	1.5 ± 0.2	1.9 ± 0.5	1.2 ± 0.6	1.8 ± 0.6	1.5 ± 0.2	678.1
131209A	2.6 ± 1.0	30 ± 60	0.8 ± 0.2	⋯	⋯	⋯	0.8 ± 0.2	360.5
131231A	5 ± 2	30 ± 40	1.0 ± 0.2	⋯	⋯	⋯	1.0 ± 0.2	4801.1
140102A	50 ± 20	4 ± 2	1.2 ± 0.4	⋯	⋯	⋯	1.2 ± 0.4	57.1
140104B	0.5 ± 0.3	900 ± 200	0.3 ± 0.6	⋯	⋯	⋯	0.3 ± 0.6	946.8
140110A	130 ± 50	1.0 ± 0.9	0.97 ± 0.02	⋯	⋯	⋯	0.97 ± 0.02	158.8
140206B	15 ± 5	30 ± 20	0.3 ± 0.3	⋯	⋯	⋯	0.3 ± 0.3	8584.4
140402A	50 ± 20	0 ± 3	0.87 ± 0.06	⋯	⋯	⋯	0.87 ± 0.06	71.5
140523A	30 ± 10	8 ± 8	1.0 ± 0.1	⋯	⋯	⋯	1.0 ± 0.1	468.6
140810A	0.4 ± 0.2	500 ± 200	0.8 ± 0.2	⋯	⋯	⋯	0.8 ± 0.2	18366.7
141028A	25 ± 10	20 ± 6	0.97 ± 0.03	⋯	⋯	⋯	0.97 ± 0.03	489.6
141102A	11 ± 6	10 ± 10	1.0 ± 0.2	⋯	⋯	⋯	1.0 ± 0.2	31.0
141207A	150 ± 60	8 ± 1	1.88 ± 0.03	⋯	⋯	⋯	1.88 ± 0.03	732.6
141222A	6 ± 3	50 ± 30	1.3 ± 0.4	⋯	⋯	⋯	1.3 ± 0.4	406.3
150314A	4 ± 1	30 ± 80	0.9 ± 0.1	⋯	⋯	⋯	0.9 ± 0.1	3064.2
150523A	20 ± 7	15 ± 7	1.0 ± 0.3	⋯	⋯	⋯	1.0 ± 0.3	6125.2
150627A	3 ± 1	200 ± 200	0.9 ± 0.2	3.0 ± 0.2	0.41 ± 0.07	2.62 ± 0.03	0.41 ± 0.07	5991.0

Table 5
(Continued)

GRB Name	Peak Flux ($\times 10^{-5}$ cm^{-2} s^{-1})	Peak Flux Time (s)	Decay Index (SPL)	Decay Index 1 (BPL)	Decay Index 2 (BPL)	Break Time (BPL) (s)	Decay Index	Extended Emission Duration (s)
150702A	0.2 ± 0.1	800 ± 600	0.4 ± 0.3	⋯	⋯	⋯	0.4 ± 0.3	1224.5
150902A	60 ± 20	5 ± 3	1.0 ± 0.2	⋯	⋯	⋯	1.0 ± 0.2	405.2
160325A	1.7 ± 0.6	100 ± 100	0.74 ± 0.10	⋯	⋯	⋯	0.74 ± 0.10	1550.7
160509A	1500 ± 500	17.5 ± 0.1	1.1 ± 0.1	0.9 ± 0.3	1.3 ± 0.3	2.8 ± 0.5	1.1 ± 0.1	5677.8
160521B	1.5 ± 0.8	90 ± 70	1.3 ± 0.2	⋯	⋯	⋯	1.3 ± 0.2	11821.5
160623A	8 ± 4	500 ± 100	1.25 ± 0.09	⋯	⋯	⋯	1.25 ± 0.09	11758.4
160625B	400 ± 200	200.6 ± 0.3	2.2 ± 0.3	⋯	⋯	⋯	2.2 ± 0.3	814.9
160816A	40 ± 10	2 ± 3	1.2 ± 0.1	1.5 ± 0.3	0.9 ± 0.6	2.1 ± 0.8	1.2 ± 0.1	1093.7
160821A	300 ± 100	137.3 ± 0.7	1.15 ± 0.10	⋯	⋯	⋯	1.15 ± 0.10	1367.1
160905A	4 ± 2	40 ± 30	1.2 ± 0.3	⋯	⋯	⋯	1.2 ± 0.3	455.5
161109A	1.9 ± 0.8	500 ± 200	1.3 ± 0.5	⋯	⋯	⋯	1.3 ± 0.5	467.5
170115B	80 ± 30	7 ± 1	1.2 ± 0.2	2 ± 2	0.9 ± 0.7	2.3 ± 0.4	1.2 ± 0.2	1026.6
170214A	400 ± 100	63.0 ± 0.4	1.7 ± 0.3	2 ± 2	1.6 ± 0.5	2.3 ± 0.5	1.7 ± 0.3	712.5
170405A	8 ± 3	30 ± 30	1.27 ± 0.01	⋯	⋯	⋯	1.27 ± 0.01	850.1
170409A	1.8 ± 0.7	300 ± 200	1.3 ± 0.1	⋯	⋯	⋯	1.3 ± 0.1	261.9
170808B	4 ± 1	100 ± 100	1.0 ± 0.2	⋯	⋯	⋯	1.0 ± 0.2	6192.2
170906A	3 ± 1	200 ± 100	0.8 ± 0.1	⋯	⋯	⋯	0.8 ± 0.1	1732.2
171010A	3 ± 1	380 ± 70	1.3 ± 0.2	2.2 ± 0.7	1.0 ± 0.3	2.9 ± 0.2	1.0 ± 0.3	2649.2
171102A	1.4 ± 0.7	60 ± 90	1.02 ± 0.07	⋯	⋯	⋯	1.02 ± 0.07	315.0
171120A	2 ± 1	10 ± 40	0.6 ± 0.3	0.2 ± 0.6	1.1 ± 0.6	2.8 ± 0.5	1.1 ± 0.6	5275.7
171124A	40 ± 10	8 ± 4	0.89 ± 0.09	⋯	⋯	⋯	0.89 ± 0.09	317.9
171210A	0.3 ± 0.1	200 ± 500	0.7 ± 0.3	⋯	⋯	⋯	0.7 ± 0.3	1368.6
180210A	1.8 ± 0.6	140 ± 80	1.0 ± 0.2	⋯	⋯	⋯	1.0 ± 0.2	1598.1
180526A	3 ± 2	800 ± 200	1.3 ± 0.7	⋯	⋯	⋯	1.3 ± 0.7	1139.7
180703A	6 ± 3	10 ± 20	0.8 ± 0.2	⋯	⋯	⋯	0.8 ± 0.2	1610.1
180720B	40 ± 20	62 ± 5	1.9 ± 0.1	1.5 ± 0.2	3.2 ± 0.6	2.37 ± 0.08	3.2 ± 0.6	613.3

Table 6
Highest-energy Events of *Fermi*-LAT GRBs

GRB Name	GBM Time Window				Time Resolved			
	Events ($P > 0.9$)	Energy (GeV)	Arrival Time (s)	Probability	Events ($P > 0.9$)	Energy (GeV)	Arrival Time (s)	Probability
080818B	…	…	…	…	3	1.70	9018.86	1.00
080825C	9	0.30	21.38	0.93	13	0.68	28.28	1.00
080916C	237	27.00	40.50	1.00	320	27.00	40.50	1.00
081006	8	0.71	1.80	1.00	12	0.80	12.08	0.99
081009	…	…	…	…	9	1.60	1250.13	0.99
081024B	6	0.45	0.26	1.00	12	1.70	2.12	1.00
081102B	6	0.74	1.33	0.97	5	0.55	0.30	1.00
081122A	1	0.15	5.05	0.93	4	2.50	66.53	1.00
081203A	…	…	…	…	5	1.00	379.66	1.00
081224	…	…	…	…	4	1.80	177.49	1.00
090102	…	…	…	…	2	0.58	3915.89	0.99
090217	19	0.82	14.83	1.00	23	0.82	14.83	1.00
090227A	1	0.43	2.90	1.00	4	2.30	51.68	1.00
090227B	2	0.13	0.21	1.00	…	…	…	…
090228A	1	0.14	0.09	1.00	5	0.70	2.09	0.92
090323	16	1.20	22.57	0.99	59	7.40	195.42	1.00
090328	12	2.30	53.30	1.00	67	5.50	697.80	1.00
090427A	…	…	…	…	2	14.00	422.87	1.00
090510	64	30.00	0.83	1.00	260	30.00	0.83	1.00
090626	3	0.12	9.00	0.99	20	2.10	111.63	1.00
090720B	6	0.43	1.68	0.99	5	0.43	1.68	1.00
090902B	245	14.00	14.16	1.00	480	40.00	81.74	1.00
090926A	252	3.30	9.48	1.00	410	19.00	24.83	1.00
091003	5	2.70	6.47	1.00	22	5.90	348.63	1.00
091031	9	0.60	6.44	1.00	25	1.40	408.18	1.00
091120	3	0.20	31.79	0.99	10	7.00	712.58	1.00
091127	1	1.60	8.61	1.00	3	2.20	16.94	1.00
100116A	8	0.84	101.30	0.99	20	33.00	378.98	1.00
100213C	…	…	…	…	3	34.00	3389.03	1.00
100225A	6	0.34	6.62	0.97	8	3.00	64.85	1.00
100325A	6	0.82	0.34	1.00	6	0.82	0.34	1.00
100414A	4	0.47	24.50	1.00	48	30.00	33.36	1.00
100423B	…	…	…	…	3	3.90	166.69	1.00
100511A	3	0.60	11.61	0.92	19	46.00	161.90	1.00
100620A	5	0.25	3.75	1.00	5	0.25	3.75	1.00
100724B	8	0.16	42.83	0.96	8	0.16	42.83	0.98
100728A	…	…	…	…	7	3.10	325.06	1.00
100826A	5	1.70	61.39	1.00	4	1.70	61.39	1.00
101014A	…	…	…	…	6	14.00	2750.71	1.00
101107A	6	4.80	139.85	1.00	7	4.80	139.85	1.00
101227B	3	1.50	20.53	1.00	3	1.50	20.53	1.00
110120A	2	0.47	0.87	0.99	10	2.00	72.46	1.00
110123A	…	…	…	…	7	2.10	445.55	1.00
110213A	…	…	…	…	2	3.00	1261.39	1.00
110328B	1	0.16	9.84	0.90	6	4.00	328.67	1.00
110428A	1	0.62	7.28	0.94	9	3.00	14.80	0.94
110518A	…	…	…	…	4	2.90	2039.24	1.00
110529A	1	0.10	0.07	1.00	…	…	…	…
110625A	…	…	…	…	7	1.70	577.24	0.95
110721A	33	6.70	4.50	1.00	36	6.70	4.50	1.00
110728A	1	0.51	0.36	1.00	6	1.40	2.98	1.00
110731A	48	0.97	5.52	1.00	75	3.50	435.96	1.00
110903A	3	16.00	301.35	1.00	4	16.00	301.35	1.00
110921B	4	0.65	13.08	0.99	10	2.00	202.48	1.00
111210B	3	0.15	47.63	0.99	7	0.56	96.10	1.00
120107A	7	1.90	7.70	1.00	8	1.90	7.70	1.00
120226A	3	0.27	30.71	0.96	10	0.38	283.65	0.96
120316A	3	2.10	26.44	1.00	10	2.10	26.44	1.00
120420B	…	…	…	…	4	1.90	3800.54	1.00
120526A	…	…	…	…	20	14.00	1354.30	1.00
120624B	4	0.36	−201.87	0.91	110	1.90	557.66	1.00
120709A	12	2.20	1.77	1.00	22	2.60	140.33	0.99

Table 6
(Continued)

GRB Name	GBM Time Window				Time Resolved			
	Events ($P > 0.9$)	Energy (GeV)	Arrival Time (s)	Probability	Events ($P > 0.9$)	Energy (GeV)	Arrival Time (s)	Probability
120711A	…	…	…	…	29	2.50	5431.65	1.00
120729A	…	…	…	…	3	2.40	396.87	1.00
120830A	3	0.48	0.75	1.00	6	0.78	2.96	1.00
120911B	50	1.20	15.51	0.96	66	1.40	90.29	1.00
120915A	2	0.18	0.14	1.00	2	0.25	0.82	0.99
120919B	…	…	…	…	3	13.00	605.27	1.00
121029A	1	0.12	13.80	0.94	5	4.30	1926.46	1.00
121123B	…	…	…	…	7	2.50	268.02	1.00
121225B	1	0.12	11.04	0.94	…	…	…	…
130310A	2	0.84	4.12	1.00	11	1.40	329.90	1.00
130325A	1	0.23	2.19	0.99	4	5.30	828.57	1.00
130327B	7	4.60	20.23	1.00	42	9.20	49.42	1.00
130427A	252	77.00	18.64	1.00	600	94.00	243.13	1.00
130502B	21	2.00	27.47	1.00	68	31.00	222.10	0.97
130504C	7	2.20	54.16	1.00	19	5.70	250.82	1.00
130518A	8	0.39	50.71	0.94	32	2.10	270.81	1.00
130606B	…	…	…	…	11	4.60	527.27	1.00
130702A	…	…	…	…	3	1.70	272.29	0.99
130821A	7	2.80	64.29	1.00	47	6.30	219.13	0.96
130828A	32	1.20	52.09	1.00	32	1.20	52.09	1.00
130907A	…	…	…	…	2	5.60	3618.37	1.00
131014A	10	1.20	1.98	1.00	23	1.80	14.37	0.98
131029A	23	1.20	71.66	1.00	35	3.20	189.93	1.00
131108A	135	1.20	5.21	1.00	200	1.50	66.33	1.00
131209A	2	0.22	15.56	0.92	8	0.29	65.13	0.91
131231A	5	0.96	37.94	1.00	35	48.00	110.29	1.00
140102A	3	0.37	3.42	0.99	12	2.30	4.29	1.00
140104B	…	…	…	…	11	3.10	809.91	1.00
140110A	29	2.00	0.62	1.00	38	2.00	0.62	1.00
140124A	1	2.30	93.56	0.96	3	2.30	93.56	0.93
140206B	24	0.75	24.00	1.00	62	11.00	6735.90	1.00
140219A	…	…	…	…	4	1.70	1356.56	1.00
140323A	…	…	…	…	4	2.80	226.80	1.00
140402A	4	0.66	0.05	1.00	16	3.70	8.73	1.00
140416A	…	…	…	…	3	10.00	2207.37	1.00
140523A	14	2.60	18.87	1.00	35	7.30	43.46	1.00
140528A	…	…	…	…	3	4.60	1377.90	1.00
140619B	21	23.00	0.61	1.00	23	23.00	0.61	1.00
140723A	18	1.00	0.56	0.99	31	1.00	0.56	1.00
140729A	9	1.30	44.14	1.00	11	1.50	73.40	1.00
140810A	…	…	…	…	13	15.00	1490.23	1.00
140825A	…	…	…	…	3	1.60	1702.32	0.91
140928A	…	…	…	…	4	52.00	2554.67	1.00
141012A	7	1.00	9.64	1.00	14	1.10	19.51	1.00
141028A	19	0.68	32.21	1.00	34	3.90	157.52	0.94
141102A	1	0.15	2.54	0.92	7	0.64	30.91	0.97
141113A	4	0.53	0.07	1.00	5	0.53	0.07	1.00
141207A	39	3.40	4.80	1.00	48	5.50	734.33	1.00
141221B	1	0.11	22.17	0.98	3	5.50	58.47	1.00
141222A	…	…	…	…	11	3.60	227.42	1.00
150118B	…	…	…	…	3	1.80	51.03	1.00
150202B	2	1.00	115.70	1.00	2	1.00	115.70	0.99
150210A	15	1.00	2.02	1.00	18	2.50	169.37	1.00
150314A	…	…	…	…	13	1.90	3064.28	0.97
150403A	…	…	…	…	5	5.40	631.76	1.00
150510A	5	0.58	2.43	1.00	9	2.00	100.91	1.00
150513A	8	2.20	−56.40	1.00	…	…	…	…
150514A	1	0.18	3.58	0.99	2	6.20	442.44	1.00
150523A	23	1.90	42.33	1.00	44	7.00	118.00	1.00
150627A	…	…	…	…	26	8.10	258.66	1.00
150702A	…	…	…	…	6	0.80	1115.33	0.99
150902A	18	0.41	6.18	0.99	40	11.00	97.49	1.00

Table 6
(Continued)

GRB Name	GBM Time Window				Time Resolved			
	Events ($P > 0.9$)	Energy (GeV)	Arrival Time (s)	Probability	Events ($P > 0.9$)	Energy (GeV)	Arrival Time (s)	Probability
160310A	…	…	…	…	2	1.40	99.25	0.95
160314B	…	…	…	…	4	0.88	628.72	0.94
160325A	2	0.31	4.98	0.96	21	3.00	92.02	1.00
160422A	…	…	…	…	2	12.00	769.62	1.00
160503A	…	…	…	…	11	0.52	12969.55	0.91
160509A	103	52.00	76.51	1.00	140	52.00	76.51	1.00
160521B	…	…	…	…	8	13.00	422.62	1.00
160623A	…	…	…	…	43	18.00	12038.53	1.00
160625B	250	15.00	346.18	1.00	260	15.00	346.18	1.00
160702A	…	…	…	…	3	4.80	1941.52	1.00
160709A	24	0.99	1.47	1.00	28	0.99	1.47	1.00
160816A	15	1.10	1.40	1.00	46	9.20	1094.77	1.00
160821A	35	0.68	156.93	0.94	52	4.70	212.43	1.00
160829A	…	…	…	…	3	9.40	0.95	1.00
160905A	5	2.20	22.03	1.00	22	7.90	347.76	1.00
160910A	3	0.15	23.57	0.91	4	0.49	197.48	0.99
161015A	9	1.00	7.47	1.00	10	1.00	7.47	1.00
161109A	…	…	…	…	8	3.40	594.81	1.00
170115B	13	0.64	1.34	0.93	28	2.30	861.41	0.99
170127C	…	…	…	…	10	0.51	2889.00	1.00
170214A	103	7.80	103.62	1.00	220	7.80	103.62	1.00
170228A	5	0.34	9.47	0.97	6	0.34	9.47	0.97
170306B	1	0.23	21.16	0.99	6	0.50	43.25	1.00
170329A	9	0.78	4.11	1.00	10	0.78	4.11	1.00
170405A	7	0.16	41.82	0.93	23	0.89	445.97	0.98
170409A	…	…	…	…	10	9.90	440.27	1.00
170424A	3	1.10	54.20	1.00	7	1.10	54.20	1.00
170510A	6	1.00	45.47	1.00	6	1.00	45.47	1.00
170522A	6	3.70	6.86	1.00	10	3.70	6.86	1.00
170728B	4	0.63	9.27	0.99	7	0.63	9.27	0.92
170808B	2	0.14	13.73	1.00	18	1.80	484.36	1.00
170813A	3	0.58	9.52	1.00	4	0.96	265.30	0.96
170825B	2	0.30	1.49	1.00	2	0.30	1.49	0.99
170906A	…	…	…	…	29	3.60	203.25	1.00
170921B	…	…	…	…	2	2.70	901.67	1.00
171010A	…	…	…	…	47	19.00	2890.98	0.99
171011C	3	0.51	−0.09	1.00	2	0.16	42.72	0.99
171102A	2	0.14	34.91	0.98	8	0.37	349.89	0.99
171120A	6	1.60	5.63	1.00	29	3.40	4840.92	1.00
171124A	20	3.60	4.08	1.00	21	3.60	4.08	1.00
171210A	2	0.65	74.83	1.00	12	12.00	1374.49	1.00
171212B	…	…	…	…	3	0.61	496.97	0.97
180210A	3	0.47	31.78	1.00	32	7.40	1621.12	1.00
180305A	1	0.20	6.18	0.99	2	8.90	1613.84	1.00
180526A	…	…	…	…	8	2.20	1308.09	1.00
180703A	2	0.21	5.06	0.99	13	0.93	40.46	1.00
180703B	…	…	…	…	5	1.10	34.22	1.00
180718B	11	0.49	2.63	0.96	9	0.49	2.63	0.99
180720B	19	0.63	38.77	1.00	130	4.90	142.43	1.00

Table 7
Fermi-LAT GRBs with Photon Energies $E > 10$ GeV

GRB Name (Class)	Energy (GeV)	Arrival Time (s)	z	$E_{\rm sf}$ (GeV)
080916C (L)	27.4	40.5	4.35	**146.6**
	12.4	16.5		66.3
090427A (L)	14.1	422.9	…	…
090510 (S)	30.0	0.83	0.90	56.8
090902B (L)	40.0	81.7	1.82	**112.5**
	21.7	331.9		61.2
	18.1	26.2		51.0
	15.4	45.6		43.4
	14.2	14.2		40.0
	12.7	42.4		35.8
	11.9	11.7		33.6
090926A (L)	19.4	24.8	2.11	60.3
	10.4	3785.0		32.3
100116A (L)	32.6	379.0	…	…
	13.3	296.0	…	…
100213C (L)	34.0	3389.0	…	…
100414A (L)	30.0	33.4	1.37	70.6
	25.1	358.5		59.5
100511A (L)	46.0	161.9	…	…
	18.4	179.8	…	…
101014A (L)	13.6	2750.7	…	…
	11.2	2962.0	…	…
110903A (L)	15.6	301.0	…	…
120526A (L)	14.3	1354.3	…	…
120919B (L)	12.7	605.3	…	…
130427A (L)	94.1	243.1	0.34	**126.1**
	77.1	18.6		**103.3**
	57.4	256.0		76.9
	38.7	78.4		51.9
	38.2	3409.0		51.2
	33.6	34366.0		45.0
	28.4	47.6		38.0
	26.9	84.7		36.0
	25.4	141.0		34.0
	19.3	6062.0		25.9
	17.1	217.0		22.9
	14.9	119.3		20.0
	12.9	80.5		17.3
	12.2	64.5		16.3
	12.0	23.5		16.1
	11.7	214.0		15.7
	10.8	23.2		14.5
130502B (L)	31.1	222.1	…	…
	17.3	48.0	…	…
131231A (L)	48.3	110.3	0.64	79.2
	17.1	844.2		28.0
140206B (L)	11.0	6735.9	…	…
140416A (L)	10.1	2207.4	…	…
140619B (L)	22.7	0.6	…	…
140810A (L)	15.4	1490.0	…	…
140928A (L)	51.7	2554.7	…	…
150902A (L)	11.3	97.5	…	…
160422A (L)	12.3	769.6	…	…
160509A (L)	51.9	76.5	1.17	**112.6**
	41.5	242.0		90.1
160521B (L)	12.7	422.6	…	…
160623A (L)	18.2	12038.5	0.37	24.9
160625B (L)	15.3	346.2	1.41	36.9
171010A (L)	19.0	2891.0	0.33	25.3
171210A (L)	12.4	1374.5	…	…

Appendix B
Description of the Content of the Fits File

All the information used to produce plots and tables in this paper is saved into a FITS file described in Table 8.

Table 8
Definition of the Columns in the *Fermi* GRB LAT FITS File

Name	Units	Description
GCNNAME		Name as appears in the GCN distribution list
GRBNAME		Name of the GRB in YYMMDDFFF
GRBDATE		Date of the trigger
GRBMET	s	Mission Elapsed Time since 2001 Jan 1 UT 00:00:00
RA	deg	R.A. (J2000)
DEC	deg	decl. (J2000)
ERR	deg	Localization error from LTF analysis
REDSHIFT		Redshift of the GRB
LUMINOSITY_DISTANCE	cm	Luminosity distance calculated using the redshift of the GRB (when available)
THETA	deg	Off-axis angle at the time of the trigger
ZENITH	deg	Zenith angle at the time of the trigger
ARR		If the GRB triggered an ARR, this flag is set to 1; otherwise, it is set to 0
DISTANCE2CLOSEST	deg	Distance to the closest 3FGL source
IRFS		Instrument response function used in the analysis
GBMT05	s	GBM T_{05}, when available; otherwise, this number is set to 0
GBMT90	s	GBM T_{90}, when available; otherwise, this number corresponds to the estimated duration of the prompt emission
GBMT95	s	Calclated as GBMT05+GBMT90
LLEBBBD_SIG	sigma	Significance of the signal in the LLE data
LLEBBBD_SIG_DETECTED		Whether the GRB is detected in LLE data
LLET05	s	LLE onset time ($T_{\rm LLE,05}$)
LLET90	s	LLE duration ($T_{\rm LLE,90}$)
LLET95	s	LLE end time ($T_{\rm LLE,95}$)
TL0	s	LAT emission estimated onset time $T_{\rm LAT,0}$
TL100	s	LAT emission estimated duration $T_{\rm LAT,100}$
TL1	s	LAT emission estimated end $T_{\rm LAT,1}$
TL0_L	s	Estimated lower limit on the LAT emission onset time $T_{\rm LAT,0}$
TL100_ERR	s	Estimated error on the LAT emission duration $T_{\rm LAT,100}$
TL1_U	s	Estimated upper limit on LAT emission end $T_{\rm LAT,1}$
LIKE_BEST_T0	s	Start of the time window for the likelihood analysis that returned the highest TS value
LIKE_BEST_T1	s	End of the time window for the likelihood analysis that returned the highest TS value
LIKE_BEST_TS_GRB		TS value obtained by the likelihood analysis that returned the highest TS value
LIKE_BEST_FLUX	ph/cm^2/s	Flux obtained by the likelihood analysis that returned the highest TS value
LIKE_BEST_FLUX_ERR	ph/cm^2/s	Estimated error on the flux obtained by the likelihood analysis that returned the highest TS value
LIKE_BEST_FLUX_ENE	erg cm^{-2} s^{-1}	Energy flux obtained by the likelihood analysis that returned the highest TS value
LIKE_BEST_FLUX_ENE_ERR	erg cm^{-2} s^{-1}	Estimated error on the energy flux obtained by the likelihood analysis that returned the highest TS value
LIKE_BEST_FLUENCE_ENE	erg cm^{-2}	Energy fluence obtained by the likelihood analysis that returned the highest TS value
LIKE_BEST_FLUENCE_ENE_ERR	erg cm^{-2} s^{-1}	Estimated error on the energy fluence obtained by the likelihood analysis that returned the highest TS value
LIKE_BEST_GRBindex		Photon index of the PL that models the GRB in the likelihood analysis that returned the highest TS value
LIKE_BEST_GRBindex_ERR		Estimated error on the photon index of the PL that models the GRB in the likelihood analysis that returned the highest TS value
LIKE_BEST_EISO52_RF	10^{52} erg	Rest-frame isotropic energy from 100 MeV to 10 GeV in the likelihood analysis that returned the highest TS value
LIKE_BEST_EISO52_RF_ERR	10^{52} erg	Estimated error on the rest-frame isotropic energy from 100 MeV to 10 GeV in the likelihood analysis that returned the highest TS value
LIKE_LAT_T0	s	Start of the time window for the likelihood analysis in the LAT time window
LIKE_LAT_T1	s	End of the time window for the likelihood analysis in the LAT time window
LIKE_LAT_TS_GRB		TS value obtained by the likelihood analysis in the LAT time window
LIKE_LAT_FLUX	ph/cm^2/s	Flux obtained by the likelihood analysis in the LAT time window
LIKE_LAT_FLUX_ERR	ph/cm^2/s	Estimated error on the flux obtained by the likelihood analysis in the LAT time window
LIKE_LAT_FLUX_ENE	erg cm^{-2} s^{-1}	Energy flux obtained by the likelihood analysis in the LAT time window
LIKE_LAT_FLUX_ENE_ERR	erg cm^{-2} s^{-1}	Estimated error on the energy flux obtained by the likelihood analysis in the LAT time window
LIKE_LAT_FLUENCE_ENE	erg cm^{-2}	Energy fluence obtained by the likelihood analysis in the LAT time window

Table 8
(Continued)

Name	Units	Description
LIKE_LAT_FLUENCE_ENE_ERR	erg cm^{-2} s^{-1}	Estimated error on the energy fluence obtained by the likelihood analysis in the LAT time window
LIKE_LAT_GRBindex		Photon index of the PL that models the GRB in the likelihood analysis in the LAT time window
LIKE_LAT_GRBindex_ERR		Estimated error on the photon index of the PL that models the GRB in the likelihood analysis in the LAT time window
LIKE_LAT_EISO52_RF	10^{52} erg	Rest-frame isotropic energy from 100 MeV to 10 GeV in the likelihood analysis in the LAT time window
LIKE_LAT_EISO52_RF_ERR	10^{52} erg	Estimated error on the rest-frame isotropic energy from 100 MeV to 10 GeV in the likelihood analysis in the LAT time window
LIKE_GBM_T0	s	Start of the time window for the likelihood analysis in the GBM time window
LIKE_GBM_T1	s	End of the time window for the likelihood analysis in the GBM time window
LIKE_GBM_TS_GRB		Value of the TSs obtained by the likelihood analysis in the GBM time window
LIKE_GBM_FLUX	ph/cm^2/s	Flux obtained by the likelihood analysis in the GBM time window
LIKE_GBM_FLUX_ERR	ph/cm^2/s	Estimated error on the flux obtained by the likelihood analysis in the GBM time window
LIKE_GBM_FLUX_ENE	erg cm^{-2} s^{-1}	Energy flux obtained by the likelihood analysis in the GBM time window
LIKE_GBM_FLUX_ENE_ERR	erg cm^{-2} s^{-1}	Estimated error on the energy flux obtained by the likelihood analysis in the GBM time window
LIKE_GBM_FLUENCE_ENE	erg cm^{-2}	Energy fluence obtained by the likelihood analysis in the GBM time window
LIKE_GBM_FLUENCE_ENE_ERR	erg cm^{-2} s^{-1}	Estimated error on the energy fluence obtained by the likelihood analysis in the GBM time window
LIKE_GBM_GRBindex		Photon index of the PL that models the GRB in the likelihood analysis in the GBM time window
LIKE_GBM_GRBindex_ERR		Estimated error on the photon index of the PL that models the GRB in the likelihood analysis in the GBM time window
LIKE_GBM_EISO52_RF	10^{52} erg	Rest-frame isotropic energy from 100 MeV to 10 GeV in the likelihood analysis in the GBM time window
LIKE_GBM_EISO52_RF_ERR	10^{52} erg	Estimated error on the rest-frame isotropic energy from 100 MeV to 10 GeV in the likelihood analysis in the GBM time window
LIKE_EXT_T0	s	Start of the time window for the likelihood analysis in the EXT time window
LIKE_EXT_T1	s	End of the time window for the likelihood analysis in the EXT time window
LIKE_EXT_TS_GRB		Value of the TSs obtained by the likelihood analysis in the EXT time window
LIKE_EXT_FLUX	ph/cm^2/s	Flux obtained by the likelihood analysis in the EXT time window
LIKE_EXT_FLUX_ERR	ph/cm^2/s	Estimated error on the flux obtained by the likelihood analysis in the EXT time window
LIKE_EXT_FLUX_ENE	erg cm^{-2} s^{-1}	Energy flux obtained by the likelihood analysis in the EXT time window
LIKE_EXT_FLUX_ENE_ERR	erg cm^{-2} s^{-1}	Estimated error on the energy flux obtained by the likelihood analysis in the EXT time window
LIKE_EXT_FLUENCE_ENE	erg cm^{-2}	Energy fluence obtained by the likelihood analysis in the EXT time window
LIKE_EXT_FLUENCE_ENE_ERR	erg cm^{-2} s^{-1}	Estimated error on the energy fluence obtained by the likelihood analysis in the EXT time window
LIKE_EXT_GRBindex		Photon index of the PL that models the GRB in the likelihood analysis in the EXT time window
LIKE_EXT_GRBindex_ERR		Estimated error on the photon index of the PL that models the GRB in the likelihood analysis in the EXT time window
LIKE_EXT_EISO52_RF	10^{52} erg	Rest-frame isotropic energy from 100 MeV to 10 GeV in the likelihood analysis in the EXT time window
LIKE_EXT_EISO52_RF_ERR	10^{52} erg	Estimated error on the rest-frame isotropic energy from 100 MeV to 10 GeV in the likelihood analysis in the EXT time window
gtsrcprob_ExtendedEmission_MAXE	MeV	Maximum energy of the event with >90% probability to be associated with the GRB, calculated during the time-resolved analysis
gtsrcprob_ExtendedEmission_MAXE_P		Probability of the event with maximum energy calculated during the time-resolved analysis
gtsrcprob_ExtendedEmission_MAXE_T	s	Arrival time of the event with maximum energy calculated during the time-resolved analysis
gtsrcprob_ExtendedEmission_NTH		Number of events with probability >90% to be associated with the GRB, calculated during the time-resolved analysis
LAT_BPL_CHI2		Value of the χ^2 obtained by fitting the LAT light curve with a BPL model
LAT_BPL_F0		Normalization of the BPL model
LAT_BPL_F0_ERR		Error on the normalization of the BPL model
LAT_BPL_IN1		First index of the BPL model
LAT_BPL_IN1_ERR		Error on the first index of the BPL model
LAT_BPL_IN2		Second index of the BPL model
LAT_BPL_IN2_ERR		Error on the second index of the BPL model
LAT_BPL_TB		Time of the break
LAT_BPL_TB_ERR		Error on the time of the break
LAT_SPL_CHI2		Value of the χ^2 obtained by fitting the LAT light curve with a simple PL model
LAT_SPL_IN1		Index of the simple PL model
LAT_SPL_IN1_ERR		Error on the index of the simple PL model
LAT_F0		Normalization of the simple PL model
LAT_F0_ERR		Error on the normalization of the simple PL model

Table 8
(Continued)

Name	Units	Description
LAT_IN		Index that best describes the behavior at late time (either LAT_BPL_IN2 or LAT_SPL_IN1), depending on the value of the respective χ^2
LAT_IN_ERR		Error on the index that best describes the behavior at late time
SU_TSINPUT		TS resulting from the LTF detection algorithm
GBM_assoc_key		Name of the GRB in the *Fermi* GBM GRB catalog
T90_ERROR	s	Error on the GBM $T_{\rm GBM,90}$ from the *Fermi* GBM GRB catalog
FLUENCE	erg cm^{-2} s^{-1}	Fluence in the 10 keV–1 MeV energy band, from the *Fermi* GBM GRB catalog
FLUENCE_ERROR	erg cm^{-2} s^{-1}	Error on the fluence in the 10 keV–1 MeV energy band, from the *Fermi* GBM GRB catalog
LC_START	s	Variable length array containing the starting points of the time interval in the time-resolved analysis
LC_MEDIAN	s	Variable length array containing the median points of the time interval in the time-resolved analysis
LC_END	s	Variable length array containing the end points of the time interval in the time-resolved analysis
LC_ENE_FLUX	erg cm^{-2} s^{-1}	Variable length array containing the energy flux values in the time-resolved analysis
LC_ENE_FLUX_ERR	erg cm^{-2} s^{-1}	Variable length array containing the energy flux value errors in the time-resolved analysis
LC_FLUENCE	erg cm^{-2}	Variable length array containing the energy fluence values in the time-resolved analysis
LC_FLUX	ph/cm^2/s	Variable length array containing the photon flux values in the time-resolved analysis
LC_FLUX_ERR	ph/cm^2/s	Variable length array containing the photon flux value errors in the time-resolved analysis
LC_INDEX		Variable length array containing the values of the photon index in the time-resolved analysis
LC_INDEX_ERR		Variable length array containing the errors on the values of the photon index in the time-resolved analysis
LC_TS		Variable length array containing the values of the TS in the time-resolved analysis

(This table is available in its entirety in FITS format.)

ORCID iDs

M. Axelsson https://orcid.org/0000-0003-4378-8785
E. Bissaldi https://orcid.org/0000-0001-9935-8106
J. W. Hewitt https://orcid.org/0000-0001-5254-2248
S. Maldera https://orcid.org/0000-0002-0698-4421
N. Omodei https://orcid.org/0000-0002-5448-7577
G. Vianello https://orcid.org/0000-0002-2553-0839

References

Abbott, B. P., Abbott, R., Abbott, T. D., et al. 2017a, ApJL, 848, L12
Abbott, B. P., Abbott, R., Abbott, T. D., et al. 2017b, ApJL, 848, L13
Abbott, B. P., Abbott, R., Abbott, T. D., et al. 2017c, PhRvL, 119, 161101
Abdo, A. A., Ackermann, M., Ajello, M., et al. 2009a, ApJL, 706, L138
Abdo, A. A., Ackermann, M., Ajello, M., et al. 2009b, Natur, 462, 331
Abdo, A. A., Ackermann, M., Arimoto, M., et al. 2009c, Sci, 323, 1688
Abdo, A. A., Ackermann, M., Asano, K., et al. 2009d, APh, 32, 193
Abdo, A. A., Ackermann, M., Asano, K., et al. 2009e, ApJ, 707, 580
Abdo, A. A., Ackermann, M., Ajello, M., et al. 2010a, ApJ, 712, 558
Abdo, A. A., Ackermann, M., Ajello, M., et al. 2010b, ApJ, 723, 1082
Abdollahi, S., Ackermann, M., Ajello, M., et al. 2017, ApJ, 846, 34
Acero, F., Ackermann, M., Ajello, M., et al. 2015, ApJS, 218, 23
Acero, F., Ackermann, M., Ajello, M., et al. 2016, ApJS, 223, 26
Ackermann, M., Ajello, M., Albert, A., et al. 2012a, ApJS, 203, 4
Ackermann, M., Ajello, M., Albert, A., et al. 2016, ApJL, 823, L2
Ackermann, M., Ajello, M., Allafort, A., et al. 2012b, Sci, 338, 1190
Ackermann, M., Ajello, M., Asano, K., et al. 2011, ApJ, 729, 114
Ackermann, M., Ajello, M., Asano, K., et al. 2013a, ApJ, 763, 71
Ackermann, M., Ajello, M., Asano, K., et al. 2013b, ApJS, 209, 11
Ackermann, M., Ajello, M., Asano, K., et al. 2014, Sci, 343, 42
Ackermann, M., Ajello, M., Baldini, L., et al. 2010a, ApJL, 717, L127
Ackermann, M., Asano, K., Atwood, W. B., et al. 2010b, ApJ, 716, 1178
Actis, M., Agnetta, G., Aharonian, F., et al. 2011, ExA, 32, 193
Ahlgren, B., Larsson, J., Nymark, T., Ryde, F., & Pe'er, A. 2015, MNRAS, 454, L31
Ajello, M., Allafort, A., Axelsson, M., et al. 2018, ApJ, 861, 85
Arimoto, M., Asano, K., Ohno, M., et al. 2016, ApJ, 833, 139
Asano, K., Guiriec, S., & Mészáros, P. 2009, ApJL, 705, L191
Atwood, W., Albert, A., Baldini, L., et al. 2013a, arXiv:1303.3514
Atwood, W. B., Abdo, A. A., Ackermann, M., et al. 2009, ApJ, 697, 1071
Atwood, W. B., Baldini, L., Bregeon, J., et al. 2013b, ApJ, 774, 76
Axelsson, M., Baldini, L., Barbiellini, G., et al. 2012, ApJL, 757, L31
Band, D., Matteson, J., Ford, L., et al. 1993, ApJ, 413, 281
Band, D. L., Axelsson, M., Baldini, L., et al. 2009, ApJ, 701, 1673
Barthelmy, S. D., Barbier, L. M., Cummings, J. R., et al. 2005, SSRv, 120, 143
Barthelmy, S. D., Kennea, J., & Racusin, J. 2012, GCN, 13381, 1
Beloborodov, A. M. 2002, ApJ, 565, 808
Beloborodov, A. M. 2005, ApJL, 618, L13
Beloborodov, A. M., Hascoët, R., & Vurm, I. 2014, ApJ, 788, 36
Benjamini, Y., & Hochberg, Y. 1995, Journal of the Royal Statistical Society. Series B (Methodological), 57, 289
Bennett, C. L., Larson, D., Weiland, J. L., & Hinshaw, G. 2014, ApJ, 794, 135
Bhat, P. N., Meegan, C. A., von Kienlin, A., et al. 2016, ApJS, 223, 28
Bissaldi, E., Omodei, N., Vianello, G., Kocevski, D. & on behalf of the Fermi-LAT Collaboration 2017, in Proc. Science, 312, ed. J. Greiner & J. McEnery, 5
Bošnjak, Ž., Daigne, F., & Dubus, G. 2009, A&A, 498, 677
Burgess, J. M., Bégué, D., Ryde, F., et al. 2016, ApJ, 822, 63
Burrows, D. N., Hill, J. E., Nousek, J. A., et al. 2005, SSRv, 120, 165
Cenko, S. B., Bloom, J. S., Morgan, A. N., & Perley, D. A. 2009, GCN, 9053, 1
Chernoff, H. 1954, Ann. Math. Statist., 25, 573
Chevalier, R. A., & Li, Z.-Y. 2000, ApJ, 536, 195
Chornock, R., Perley, D. A., Cenko, S. B., & Bloom, J. S. 2009, GCN, 9028, 1
Ciprini, S., Thompson, D. J. & on behalf of the Fermi LAT Collaboration 2013, arXiv:1303.4054
Connaughton, V., Briggs, M. S., Goldstein, A., et al. 2015, ApJS, 216, 32
Corsi, A., Guetta, D., & Piro, L. 2010, ApJ, 720, 1008
Cucchiara, A., Fox, D., Levan, A., & Tanvir, N. 2009a, GCN, 10202, 1
Cucchiara, A., & Fox, D. B. 2010, GCN, 10606, 1
Cucchiara, A., Fox, D. B., Cenko, S. B., Tanvir, N., & Berger, E. 2009b, GCN, 10031, 1
Cucchiara, A., Fox, D. B., Tanvir, N., & Berger, E. 2009c, GCN, 9873, 1
Cummings, J. R., & Palmer, D. M. 2013, GCN, 14257, 1
Daigne, F., Bošnjak, Ž., & Dubus, G. 2011, A&A, 526, A110
de Ugarte Postigo, A., Campana, S., Thöne, C. C., et al. 2013a, A&A, 557, L18
de Ugarte Postigo, A., Fynbo, J. P. U., Thoene, C., et al. 2015a, GCN, 17583, 1
de Ugarte Postigo, A., Jakobsson, P., Malesani, D., et al. 2009, GCN, 8766, 1
de Ugarte Postigo, A., Kann, D. A., Thoene, C. C., et al. 2017, GCN, 20990, 1

de Ugarte Postigo, A., Thoene, C. C., Gorosabel, J., et al. 2013b, GCN, 15470, 1
de Ugarte Postigo, A., Xu, D., Malesani, D., et al. 2013c, GCN, 15187, 1
de Ugarte Postigo, A., Xu, D., Malesani, D., & Tanvir, N. R. 2015b, GCN, 17822, 1
Desai, A., Ajello, M., Omodei, N., et al. 2017, ApJ, 850, 73
Duncan, R. C., & Thompson, C. 1992, ApJL, 392, L9
Esposito, J. A., Bertsch, D. L., Chen, A. W., et al. 1999, ApJS, 123, 203
Evans, P. A., Goad, M. R., Osborne, J. P., & Beardmore, A. P. 2016, GCN, 19927, 1
Galli, M., Marisaldi, M., Fuschino, F., et al. 2013, A&A, 553, A33
Gao, H., Lei, W.-H., Zou, Y.-C., Wu, X.-F., & Zhang, B. 2013, NewAR, 57, 141
Gehrels, N., Chincarini, G., Giommi, P., et al. 2004, ApJ, 611, 1005
Gehrels, N., & Razzaque, S. 2013, FrPhy, 8, 661
Ghisellini, G., Ghirlanda, G., Nava, L., & Celotti, A. 2010, MNRAS, 403, 926
Gilmore, R. C., Bouvier, A., Connaughton, V., et al. 2013, ExA, 35, 413
Goad, M. R., Osborne, J. P., Beardmore, A. P., & Evans, P. A. 2015, GCN, 18403, 1
Goldstein, A., Veres, P., Burns, E., et al. 2017, ApJL, 848, L14
Granot, J., Cohen-Tanugi, J., & do Couto e Silva, E. 2008, ApJ, 677, 92
Greiner, J., Clemens, C., Krühler, T., et al. 2009, A&A, 498, 89
Gruber, D., Goldstein, A., Weller von Ahlefeld, V., et al. 2014, ApJS, 211, 12
Gruber, D., Paciesas, W., Pelassa, V., & Chaplin, V. 2012, GCN, 13757, 1
Hascoët, R., Daigne, F., Mochkovitch, R., & Vennin, V. 2012, MNRAS, 421, 525
Inoue, S., Granot, J., O'Brien, P. T., et al. 2013, APh, 43, 252
Ito, H., Nagataki, S., Matsumoto, J., et al. 2014, ApJ, 789, 159
Kankare, E., O'Neill, D., Izzo, L., et al. 2017, GCN, 22002, 1
Katz, J. I., & Piran, T. 1997, ApJ, 490, 772
Kocevski, D., Kennea, J. A., Lien, A. Y., Page, K. L., & Racusin, J. L. 2015, GCN, 17810, 1
Kouveliotou, C., Meegan, C. A., Fishman, G. J., et al. 1993, ApJL, 413, L101
Kruehler, T., Greiner, G., & A, K. D. 2010, GCN, 14500, 1
Kruehler, T., Schady, P., Greiner, J., & Tanvir, N. R. 2017, GCN, 20686, 1
Kumar, P., & Barniol Duran, R. 2009, MNRAS, 400, L75
Landsman, W., de Pasquale, M., Kuin, P., et al. 2008, GCN, 8601, 1
Lebrun, F., Leray, J. P., Lavocat, P., et al. 2003, A&A, 411, L141
Leloudas, G., Fynbo, J. P. U., Schulze, S., et al. 2013, GCN, 14983, 1
Lien, A., Sakamoto, T., Barthelmy, S. D., et al. 2016, ApJ, 829, 7
Lithwick, Y., & Sari, R. 2001, ApJ, 555, 540
Malesani, D., de Ugarte Postigo, A., de Pasquale, M., et al. 2016, GCN, 19708, 1
Malesani, D., Goldoni, P., Fynbo, J. P. U., et al. 2009, GCN, 9942, 1
Maselli, A., Melandri, A., Nava, L., et al. 2014, Sci, 343, 48
Mattox, J. R., Bertsch, D. L., Chiang, J., et al. 1996, ApJ, 461, 396
Meegan, C., Lichti, G., Bhat, P. N., et al. 2009, ApJ, 702, 791
Mészáros, P., Ramirez-Ruiz, E., & Rees, M. J. 2001, ApJ, 554, 660
Metzger, B. D., Giannios, D., Thompson, T. A., Bucciantini, N., & Quataert, E. 2011, MNRAS, 413, 2031
Milne, P. A., & Cenko, S. B. 2011, GCN, 11708, 1
Mirzoyan, R. 2019, ATel, 12390
Moretti, E., & Axelsson, M. 2016, MNRAS, 458, 1728
Nava, L., Vianello, G., Omodei, N., et al. 2014, MNRAS, 443, 3578
Nemiroff, R. J., Connolly, R., Holmes, J., & Kostinski, A. B. 2012, PhRvL, 108, 231103
Norris, J. P. 2002, ApJ, 579, 386
Norris, J. P., Nemiroff, R. J., Bonnell, J. T., et al. 1996, ApJ, 459, 393
Planck Collaboration, Ade, P. A. R., Aghanim, N., et al. 2016, A&A, 594, A13
Preece, R., Burgess, J. M., von Kienlin, A., et al. 2014, Sci, 343, 51
Pugliese, V., Xu, D., Tanvir, N. R., et al. 2015, GCN, 17672, 1
Racusin, J. L., Burns, E., Goldstein, A., et al. 2017, ApJ, 835, 82
Racusin, J. L., Burrows, D. N., D'Elia, V., et al. 2012, GCN, 13845, 1
Rau, A., McBreen, S., & Kruehler, T. 2009, GCN, 9353, 1
Razzaque, S. 2010, ApJL, 724, L109
Razzaque, S., Dermer, C. D., & Finke, J. D. 2010, OAJ, 3, 150
Razzaque, S., Mészáros, P., & Zhang, B. 2004, ApJ, 613, 1072
Roming, P. W. A., Kennedy, T. E., Mason, K. O., et al. 2005, SSRv, 120, 95
Ryde, F., Axelsson, M., Zhang, B. B., et al. 2010, ApJL, 709, L172
Sanchez-Ramirez, R., Gorosabel, J., Castro-Tirado, A. J., Cepa, J., & Gomez-Velarde, G. 2013, GCN, 14685, 1
Sari, R. 1997, ApJL, 489, L37
Sari, R., Piran, T., & Narayan, R. 1998, ApJL, 497, L17
Scargle, J. D., Norris, J. P., Jackson, B., & Chiang, J. 2013, ApJ, 764, 167
Shao, L., Xiao, Z., & Ma, B.-Q. 2010, APh, 33, 312
Spitkovsky, A. 2006, ApJL, 648, L51
Tak, D., Omodei, N., Uhm, L., et al. 2019, ApJ, submitted
Tanvir, N. R., & Ball, J. 2012, GCN, 13532, 1
Tanvir, N. R., Levan, A. J., Cenko, S. B., et al. 2016, GCN, 19419, 1
Tanvir, N. R., Wiersema, K., Levan, A. J., et al. 2012, GCN, 13441, 1
Tanvir, N. R., Wiersema, K., Levan, A. J., Cenko, S. B., & Geballe, T. 2011, GCN, 12225, 1
The CTA Consortium 2019, Science with the Cherenkov Telescope Array (Singapore: World Scientific Publishing Co. Pte. Ltd.)
Thompson, C., & Madau, P. 2000, ApJ, 538, 105
Toma, K., Wu, X.-F., & Mészáros, P. 2009, ApJ, 707, 1404
Usov, V. V. 1992, Natur, 357, 472
Vasileiou, V., Jacholkowska, A., Piron, F., et al. 2013, PhRvD, 87, 122001
Veres, P., Meegan, C., & Mailyan, B. 2018, GCN, 23053, 1
Vianello, G., Gill, R., Granot, J., et al. 2018, ApJ, 864, 163
Vianello, G., Omodei, N., Chiang, J., & Digel, S. 2017, ApJL, 841, L16
Vianello, G., Omodei, N. & Fermi/LAT Collaboration 2015, arXiv:1502.03122
von Kienlin, A., Veres, P., Roberts, O. J., et al. 2019, ApJ, 876, 89
Wang, X.-Y., Li, Z., Dai, Z.-G., & Mészáros, P. 2009, ApJL, 698, L98
Weinberg, S. 1972, Gravitation and Cosmology: Principles and Applications of the General Theory of Relativity (Weinheim: Wiley-VCH), 688
Willingale, R., O'Brien, P. T., Osborne, J. P., et al. 2007, ApJ, 662, 1093
Winkler, C., Courvoisier, T. J.-L., Di Cocco, G., et al. 2003, A&A, 411, L1
Xu, D., de Ugarte Postigo, A., Schulze, S., et al. 2013, GCN, 14478, 1
Xu, D., Levan, A. J., Fynbo, J. P. U., et al. 2014a, GCN, 16983, 1
Xu, D., Malesani, D., Fynbo, J. P. U., et al. 2016, GCN, 19600, 1
Xu, D., Malesani, D., Tanvir, N. R., et al. 2014b, GCN, 15645, 1
Zhang, B., Fan, Y. Z., Dyks, J., et al. 2006, ApJ, 642, 354